uOttawa

L'Université canadienne
Canada's university

FACULTÉ DES ÉTUDES SUPÉRIEURES ET POSTOCTORALES

uOttawa

L'Université canadienne
Canada's university

FACULTY OF GRADUATE AND POSDOCTORAL STUDIES

Abdessamad Benhsaien
AUTEUR DE LA THÈSE / AUTHOR OF THESIS

M.A.Sc. (Electrical Engineering)
GRADE / DEGREE

School of Information Technology and Engineering
FACULTÉ, ÉCOLE, DÉPARTEMENT / FACULTY, SCHOOL, DEPARTMENT

Self-Assembled Quantum Dot Semiconductor Nanostructures Modeling: Photonic Device Applications

TITRE DE LA THÈSE / TITLE OF THESIS

T.Hall
DIRECTEUR (DIRECTRICE) DE LA THÈSE / THESIS SUPERVISOR

CO-DIRECTEUR (CO-DIRECTRICE) DE LA THÈSE / THESIS CO-SUPERVISOR

EXAMINATEURS (EXAMINATRICES) DE LA THÈSE / THESIS EXAMINERS

P. Berini

J. Albert

Gary W. Slater
Le Doyen de la Faculté des études supérieures et postdoctorales / Dean of the Faculty of Graduate and Postdoctoral Studies

Self-Assembled Quantum Dot Semiconductor Nanostructures Modeling: Photonic Device Applications

By

Abdessamad Benhsaien

Thesis submitted to the
Faculty of Graduate and Postdoctoral Studies
In partial fulfillment of the requirements for the degree of
Master of Applied Science in *Electrical Engineering*

School of Information Technology and Engineering
Faculty of Engineering
University of Ottawa
Ottawa Ontario, Canada

Your file Votre référence
ISBN: 978-0-494-18398-4
Our file Notre référence
ISBN: 978-0-494-18398-4

Acknowledgements

I would like to express my sincere gratitude to my advisor Professor T.J. Hall for his trust, insightful guidance and patience. I am indebted to him for his continuous financial support at the most critical and formative time without which this work would have been impossible. I would like to single out the following people (in alphabetical order) and gratefully thank them for lending me their timely help during the development of this thesis and especially for their unique advice, constructive discussions, invaluable remarks and clarifications that made moments of doubt really ephemeral and contributed a great deal to my work.

Jacques Albert (Carleton University, Ottawa Ontario, Canada),

Claudine Allen (National Research Council, Ottawa Ontario, Canada),

Pierre Berini (University of Ottawa, Ottawa Ontario, Canada),

Stefan Birner (Walter Schottky Institute, Garching, Germany),

Kian-Seng Chang (City University of Hong Kong, Kowloon, Hong Kong),

Michael J. Connelly (University of Limerick, Limerick, Ireland),

Mirek Florjanczyk (University of Ottawa, Ottawa Ontario, Canada),

Karin Hinzer (Bookham Inc., Ottawa Ontario, Canada),

Yih-Yin Lin (University of Michigan, Ann Arbor MI, USA),

Marco Pala (Universita' di Pisa, Pisa, Italy),

Jamie Ramsey (University of Ottawa, Ontario Canada),

Sylvain Raymond (National Research Council, Ottawa Ontario Canada),

Bruno Riel (Cyrium Technologies Inc., Ottawa Ontario, Canada),

Sébastien Sauvage (Institut d'Electronique Fondamentale, Orsay, France),

Jason Taylor (University of Ottawa, Ottawa Ontario, Canada),

Valery Tolstikhin (OneChip Photonics, Ottawa Ontario, Canada).

Abstract

A microscopic analysis of a vertical stack of self-assembled *InAs/GaAs* lens-shaped quantum dot nanostructures is presented. The analysis revolves around a rigorous Hamiltonian formulation of an eight-band *k.p.* perturbation to account for the lattice-mismatch strain endured by the islands. The numerical implementation yields the effective bandgap energy and electronic structure of an *InAs/GaAs* quantum dot. Within the framework of a resonant two-level energy system, material gain and absorption spectra are calculated up to a third-order susceptibility to include nonlinearity. The material gain polarization dependence is expressed in the dipole transition strength. Polarization-dependent anisotropy factors corresponding to different interband transitions are derived and shown to satisfy a momentum conservation rule.

Modal analysis of a rectangular core waveguide realized by imbedding the active quantum dot layer(s) into a cladding medium with lower refractive index is presented. Polarization-independent modal gain is achieved by optimizing the width of the rectangular core waveguide. In illustration of a quantum dot device, a realistic semiconductor optical amplifier model accounting for both stimulated and spontaneous emission is considered. The calculated carrier density longitudinal profile yields other parameters characterizing the amplifier performance.

Contents

Acknowledgements ---- *ii*

Abstract ---- *iii*

Contents ---- *iv*

Tables ---- *vii*

Figures ---- *viii*

Chapter One: Introduction ---- *1*

I. Prologue ---- 1

II. Literature Review ---- 2

III. Outline ---- 3

IV. Achievements ---- 5

Chapter Two: Electronic Structure ---- *7*

I. Introduction ---- 8

II. Theory ---- 9

II. 1 Hamiltonian Formulation ---- 10

II. 2 Solution Overview ---- 11

II.2.1 Domain Partition ---- 11

II.2.2 Strain Distribution ---- 13

II.2.3 Boundary Conditions ---- 16

II.2.4 Hermitian Property ---- 17

II.2.5 Matrix Elements ---- 18

III. Software Implementation ---- 20

III.1 State Index ---- 20

III.2 Eigensolution Computing ---- 21

III.3 Accelerated Version ---- 22

IV. Software Validation ---- 22

IV.1 Input Material Parameters ---- 22

IV.2 Convergence Analysis ---- 23

IV.3 Quantitative Validation ---- 27

IV.4 Qualitative Validation ---- 28

IV.4.1 Test Case 1: Strain Effects on Electronic Structure ---- 29

IV.4.2 Test Case 2: Quantum Confinement Effect on Energy Spectrum ---- 30

IV.4.3 Test Case 3: Quantum Confinement Effect on Eigenstate ---- 30

IV.4.4 Test Case 4: Repeated Vertical Close Stacking Effect ---- 32

V. Conclusions ---- 33

Chapter Three: Susceptibility Analysis ---- *34*

I. Introduction ---- 34

II. Transition Strength ---- 35

II.1 Wetting Layer ---- 36
II. 2 Lens-Shaped Dot ---- 36
II. 3 Momentum Conservation ---- 37

III. Transition Line Broadening ---- 37
III.1 Inhomogeneous Broadening ---- 37
III.2 Homogeneous Broadening ---- 38
III.3 Joint Broadening ---- 39

IV. Fermi Level Energies ---- 39

V. Material Susceptibility ---- 42
V.1 Linear Material Gain ---- 43
V.2 Non-Linear Material Gain ---- 43
V.3 Gain Simulations ---- 44
V.4 Differential Gain ---- 45
V.5 Linewidth Enhancement Factor ---- 46

VI. Conclusion ---- 48

Chapter Four: Waveguide Modal Analysis ---- *50*

I. Introduction ---- 50

II. Refractive Index ---- 51

III. Waveguide Modal Analysis ---- 54
III.1 Rectangular Waveguides: 2D Problem ---- 54
III.1.1 Quasi-TE Wave Equation ---- 56
III.1.2 Quasi-TM Wave Equation ---- 56
III.2 Marcatili Method ---- 56
III.3 Slab Waveguides: 1D Problem ---- 58
III.3.1 Vertical Slab Waveguide (Growth Direction) ---- 58
III.3.2 TE Field Distribution ---- 59
III.3.3 TM Field Distribution ---- 61
III.3.4 Horizontal Slab Waveguide (Width Direction) ---- 61
III.4 Optical Confinement Factors ---- 62
III.5 Modal Gain ---- 63

IV. Polarization-Insensitive Modal Gain Analysis ---- 64
IV.1 Problem Statement ---- 64
IV.2 Solution Overview ---- 65
IV.3 Numerical Illustrations ---- 65

V. Conclusion ---- 71

Chapter Five: Photonic Device Application ---- *72*

I. Device Structure ---- 72

II. Amplifier Model ---- 73
II.1 Signal Propagation ---- 73
II.2 Noise Propagation ---- 75
II.3 Carrier Density Rate Equations ---- 76
II.4 Steady-State Model ---- 77
II.5 Solution Overview ---- 78

III. Performance Analysis ---- 80

IV. Conclusion ---- 83

Chapter Six: Conclusion ---- *84*
I. Epilogue ---- 84
II. Extensions ---- 84

Appendix A1 ---- *86*
Appendix A2 ---- *87*
Appendix A3 ---- *90*
Appendix B ---- *91*
Appendix C ---- *97*
Bibliography ---- *98*

Tables

Table 2.1: Comparison of *k.p.* Computed and (PL) Measured Transition Energies 28

Table 3.1: Γ point Quantum Well Anisotropy Factors 36

Table 3.2: Γ Point Lens Shaped Quantum Dot Anisotropy Factors 37

Table 4.1. Emission Wavelengths of a Multi-Fold Layer Quantum Dot Structure 69

Table A.1: Useful Band Structure Parameters 90

Table C:1: Useful Parameters Used in SOA Simulations 97

Figures

Figure 1.1: Done Shaped *InAs/GaAs* Island TEM Image 1
Figure 2.1: Lens Shaped Dot Geometrical Representation 9
Figure 2.2: Schematic of the Island, Wetting Layer and Substrate Structures 12
Figure 2.3: Unit Cell Transverse and Normal Cross-Sections Sub-Regions 13
Figure 2.4: Inhomogeneous Strain Spatial Distribution 15
Figure 2.4: Inhomogeneous Strain Spatial Distribution 15
Figure 2.5: Global Hermitian Property of the Hamiltonian Matrix 18
Figure 2.6: Electronic Structure of an *InAs/GaAs* Lens-Shaped Dot 25
Figure 2.7: Normalized Eigenstate Power Spectra 26
Figure 2.8: Quantum Confinement Effect on Transition Energy 30
Figure 2.9.a: Envelope Function Magnitudes $|F|^2$ through the xz plane 31
Figure 2.9.b: Envelope Function Magnitudes $|F|^2$ through the xz plane 31
Figure 2.10: Perpendicular Stacking Effect on Ground Transition Energy 33
Figure 3.1: Active Region Physical Layers Breakdown 39
Figure 3.2: Energy Offset between Band Edges and Fermi Levels 41
Figure 3.3 : Material Gain 45
Figure 3.4 : Material Gain Peak vs. Injection Level 46
Figure 3.5: Refractive Index Change Dispersion 47
Figure 3.6: Linewidth Enhancement Factor Dispersion 47
Figure 3.7: $|\alpha_e(\lambda)|$ at saturating carrier density levels 48
Figure 4.1: Schematic View of the Embedded Active Layers 51
Figure 4:2 Refractive Index Spatial Profile 52
Figure 4.3: Core-Clad Refractive Index Contrast 53
Figure 4.4: Rectangular Waveguide with a Uniform Transverse Cross-Section 55
Figure 4.5: Rectangular Waveguide and Its Equivalent Independent Slab Waveguides 57
Figure 4:6 Refractive Index Vertical Profile 60
Figure 4.7: Core Width Optimization Process 65
Figure 4.8: Optimal Waveguide Core Width Dispersion 66
Figure 4.9: Optimal Waveguide Core Width Dispersion 67
Figure 4.10 Mode Cutoff Widths 68
Figure 4.11: (Optimal) Effective Index Dispersion 69
Figure 4.12: (Optimal) Power Confinement Dispersion 70
Figure 4:13: Optimal Core width Birefringence 71

Figure 5.1: Device and Active Layer Structures 73
Figure 5:2 Steady-State Polarization-Insensitive SOA Amplifier Model 77
Figure 5:3 SOA Longitudinal Distributions (-25 dBm , 0.5A) 80
Figure 5:4 SOA Longitudinal Distributions (-25dBm, 2A) 81
Figure 5:5 SOA Characteristic Parameters 82
Figure B.1: Geometry of Quantum Well Structure 91

Chapter One

Introduction

I. Prologue

The effects of size quantization on the carrier motion trigger immediate optoelectronic device applications. Indeed, the three dimensional spatial confinement in quantum dots results in highly localized carriers and thus facilitates a more efficient light and matter interaction. In particular, the smaller the quantum dots are the more atom-like properties they display. It ensues that a quantum mechanical treatment is necessary to fully characterize the microscopic inherent properties of such zero dimensional media. The *ab initio* calculations are central in the design of quantum effect optoelectronic devices in that they produce the electronic structure of the active medium. The computed dot energy states are critical in evaluating the zero dimensional gain and absorption spectra due to interband transitions between conduction and valence discrete states.

The semiconductor material combination $In_xGa_{1-x}As/Al_{1-y}Ga_yAs$ is the model of choice herein since it is the most studied and best understood system. Moreover dots of lens shape, as shown in figure 1.1, and circular base are selected as an idealization to simplify the numerical model since the literature on the subject reports various theoretical and experimental geometrical shapes of the islands.

Figure 1.1: Dome Shaped *InAs/GaAs* Island TEM[1] Image [49]

[1] TEM: Transmission Electron Microscope

On the other hand, imbedding a single or multifold stack of quantum dot layers into a cladding material of lower refractive index provides optical waveguiding. A rigorous analysis of the propagating mode(s) is mandatory in order to optimize the waveguide geometry and electromagnetic field distribution. The carrier confinement and the optical field confinement are engineered individually and such waveguides are referred to as separate confinement heterostructures.

Moreover, coating the input and output facets of the active waveguide with some anti-reflective material helps suppress (minimize) feed back and results in an active resonant photonic cavity. Under appropriate injection above transparency, the cavity acts as an amplifier provided the modal gain overcompensates for the inherent absorption and loss of the active medium. Several radiative and nonradiative mechanisms help deplete the initially injected carriers resulting inevitably in gain saturation. This implies that an accurate carrier density spatial distribution is required to be able to characterize the amplifier performance.

II. Literature Review

Several authors point out that an accurate knowledge of the electronic structure is of paramount importance to understand the physics and device applications of quantum dot structures. *Skolnick et al* [54] cover the more recent advances in the study of single and self-assembled quantum dots as well as their device applications. In particular, a detailed account of the dot shape anisotropies effects on the optical spectra is described in [54]. The strain effects, the driver behind the self-assembly growth mechanism, is reviewed in detail by *Bhattacharya et al* in [14]. *Jiang* and *Singh* [36], *Bimberg et al* [15] are the pioneers to investigate the nature of the strain tensor in quantum dot structures. The former authors have shown that due to the high lattice-mismatch strain in self-assembled structures, the simple decoupled conduction-valence picture and the effective mass description fail to accurately predict the electronic structure of zero dimensional media [36].

While many authors rely on the adequacy of the *k.p* method near the Γ point, *Riel et al* provide an introductory model to compute the energy levels for ideal dots [49]. *Baraff* and *Gershoni* consider advanced mathematical formulations [11, 27] of the *k.p* method in quantum dot structures with internal interfaces having perpendicular planes. The method considered in chapter two is inspired from the articles [11, 27] and customized to the requirements of the dome-shaped geometry using the Hamiltonian operator described in [36]. *Sugawara et al* provide a comprehensive description of the optical properties of semiconductor quantum nanostructures such as the material gain [65]. On the other hand, *Visser et al* derive a new identity relating the material gain and field distribution (or confinement factor) in an active dielectric waveguide [66] and show that the gain associated with a guided mode cannot be expressed, as often thought, in terms of the fraction of power flow that is confined to the active region. Moreover, *Chiang* and *Wong* present a comprehensive modal analysis for several types of polarization-insensitive waveguide structures [69]. A deep understanding of the latter article [69] is the key to the development of the polarization-insensitive algorithm detailed in chapter four. *Connelly* presents a flexible steady-state semiconductor optical amplifier with a bulk active region [22]. The amplifier model described in [21, 22] is extended to quantum dot active regions in chapter five under polarization insensitive single mode operation.

III. Outline

Essentially, this thesis comprises three parts that can be summarized as follows:

1. Microscopic analysis of the material properties of *InAs/GaAs* semiconductor quantum dots governed by the *Schrödinger* equation. The outcome of this study produces the effective band gap of the highly-strained *InAs/GaAs* dot, the dot eigenenergies and eigenstates which are instrumental in calculating the gain and absorption spectra.

2. Macroscopic analysis of the modal field distribution governed by polarization-dependent wave equations derived from *Maxwell*'s equations. The outcome of this study produces the optimal waveguide core width, effective refractive index (or modal propagation constant) and optical confinement factors constrained to polarization-insensitive modal gain.

3. Photonic device performance simulation governed by the injected carrier density rate equations. The outcome of this study produces various parameters characterizing the performance of a quantum dot semiconductor optical amplifier.

A breakdown by chapter of the entire thesis substance is presented next.

Chapter one presents a brief motivation and summarizes the achievements of this thesis.

Chapter two establishes the bedrock of this work and is concerned with computing the electronic structure of self-assembled quantum dots. It presents an eight band *k.p* Hamiltonian formulation built upon a custom domain partition compatible with the island dome shape geometry. It presents an elaborate account of matching boundary conditions at the internal interfaces. It also shows that the numerical implementation is supplemented by two convergence criteria which help decide on the optimal unit cell dimensions and the number of waves in each direction. The available experimental measurements of the photoluminescence (PL) spectra of lens-shaped dots produced by NRC[2] [49] are used as benchmark to validate the computational model developed herein.

Chapter three is concerned mainly with the zero-dimensional material gain and absorption spectra calculations. It refers to appendix B where quantum mechanical derivations are explicitly shown for the momentum matrix elements as well as anisotropy factors. It also presents the noise characteristics of quantum dots through a brief examination of the linewidth enhancement factor.

Chapter four is concerned mainly with immunizing a rectangular core waveguide against the state

---

[2] National Research Council, Ottawa Ontario, Canada

of polarization. It shows that the approach achieving polarization-insensitive modal gain consists of optimizing the nonplanar waveguide aspect ratio in order to make up for the non-altered anisotropy of the gain medium. It also presents a plethoric formulation founded on many assumptions which ultimately reduces to an iterative optimization process.

Chapter five is concerned mainly with illustrating a photonic device application of quantum dots. It simulates the steady-state performance of a semiconductor optical amplifier based on a carrier density longitudinal distribution.

Chapter six summarizes the conclusions, recommendations and potential extensions of this work.

IV. Achievements

This thesis provides state of the art formulations and computational tools necessary for the quantitative and qualitative analyses of self-assembled lens-shaped quantum dot active media. It must be emphasized that at the beginning of this work no commercial tool modeling and simulating zero dimensional media was available to the knowledge of the author. Equally important are the developed software library and processes accompanying this work. An optoelectronic device designer will undoubtedly benefit from various insightful simulation results of this work which would help shorten the development lifecycle of a prototype. For example, in a computer aided design environment, the electronic structure computational engine may be used to engineer the effective bandgap energy of the strained quantum dots. This means the designer can make an enlightened decision as to how many quantum dot layers should be stacked vertically, how thick the quantum dot layers and barrier spacing should be, how much lateral expansion of the dots of the higher layers can be expected and so forth. These are intricate questions which are susceptible to affect the device performance and thus require an in-depth analysis of the material. Overall, the software helps deciding on the critical dimension along the growth direction (thickness of the dot layers) which induces vertical electronic coupling of the

eigenstates so that the whole nanostructure effectively behaves as a single large quantum dot.

Additionally, the merits of the polarization-insensitive modal gain formulations must be stressed. First, the indirect method developed here considers the passive core analog and therefore enables real-valued material parameter analysis in contrast to direct methods which consider the active core with complex-valued material parameters. Second, a non-spatially varying refractive index of the active core corresponding to an equivalent homogeneous isotropic core is derived. This simplifies the piecewise continuous spatial distribution of the refractive index otherwise. Third, the rectangular waveguide modal analysis is reduced into the analysis of two associated independent slab waveguides thereby reducing the dimensionality of the problem. Overall, the software helps deciding on the critical dimension along the transverse direction (i.e. optimal width of active core) which induces polarization-immune modal gain within a preset tolerance.

Last, this thesis extends a reported semiconductor optical amplifier model into active regions with quantum dots. It predicts the tapered longitudinal profile of the cavity under polarization-immune mode operation. This is a tremendous achievement which would remove the current hurdle in commercialization of such devices [3].

Chapter Two

Electronic Structure

To acquire a sound understanding of the physics underlying self-assembled quantum dots, it is important to develop familiarity with the structural, electronic and optical properties of such three-dimensionally confined nanostructures. In particular, special attention is devoted herein to the computation of electronic interband transition energies in the presence of an incident optical wave. Such energies are critical in evaluating the material absorption and gain spectra.

To compute the quantum dot energy discrete levels, a Hamiltonian formulation based on an eight band *k.p* perturbation method is adopted. The considered Hamiltonian operator includes the influence of remote bands on the conduction and valence band states and accounts for strain induced crystal deformation effects as well.

The implementation uses a *Fourier series* expansion of the eight band envelope functions over a parallelepiped unit cell volume. This heterostructure is divided into smaller spatially non-uniform but compositionally homogeneous bulk regions whose internal interfaces are not necessarily planar surfaces. Demands of matching boundary conditions across the internal interfaces are adhered to following a typical prescription in the literature. Periodic boundary conditions apply at the external interfaces. In order to fully exploit the horizontal and vertical symmetry walls, the calculations are carried out over a reduced subset of the unit cell transverse section only.

Quite a few convergence and validation tests accompanying this work substantiate the accuracy and reliability of the numerical results.

Numerical illustrations are provided in the case of lens-shaped *InAs* islands grown onto a thin wetting layer made out of the same binary compound and surrounded by *GaAs* potential barrier.

I. Introduction

The *k.p* method can be identified as a second order perturbation approach which yields the energy dispersion of the conduction and valence bands. The *k.p* calculations consist of expanding the electron and hole wave functions on the basis of the bandedge state functions giving rise to an associated eigenvalue problem. This approach provides a continuation in the wave vector k of the energy bands in the vicinity of some special point in the Brillouin zone. It is established that the *k.p* method is more accurate near the Γ point where $k \sim 0$. For direct band gap semiconductors, this means that the *k.p* method can adequately handle the non parabolic band mixing effects.

In the case of three-dimensional quantum confinement, the *k.p* method furnishes energy states at various discrete wave vector states (k_x, k_y, k_z) commonly referred to as quantized states. As a matter of fact, the wave vector k is interpreted as a spatial differential operator, $k = -i\nabla$ or momentum operator $p = \hbar k = -i\hbar\nabla$ with components $p_\alpha = \hbar k_\alpha = -i\hbar\partial_\alpha, \alpha = x, y, z$ where $\hbar$ is the reduced *Planck* constant, ∇ is the gradient operator and ∂_α is the partial derivative with respect to the spatial variable α.

On the other hand, the electronic band structure depends on the specific geometry - lens or pyramidal shape, size and orientation (i.e. growth direction) of the quantum dot. Of interest are lens-shaped dots with a circular base grown along the perpendicular direction (001). These dots can easily be represented by the upper-half of an oblate spheroid as depicted in figure 2.1.

The parametric equations of the dot shown in figure 2.1 are given by:

$$\begin{cases} x = R\cos\theta\sin\phi \\ y = R\sin\theta\sin\phi \\ z = t_{QD}\cos\phi \end{cases} \qquad (2.1.1)$$

where R denotes the radius of the base lying onto the transverse xy plane of the spheroid and $t_{QD}<R$ the thickness of the dot along the growth direction z. The ratio of the thickness to the

diameter $\frac{t_{QD}}{2R}$ is referred to as the aspect ratio of the dot. The polar angle θ varies between 0 and 2π whereas the azimuthal angle ϕ varies between $-\frac{\pi}{2}$ and $\frac{\pi}{2}$.

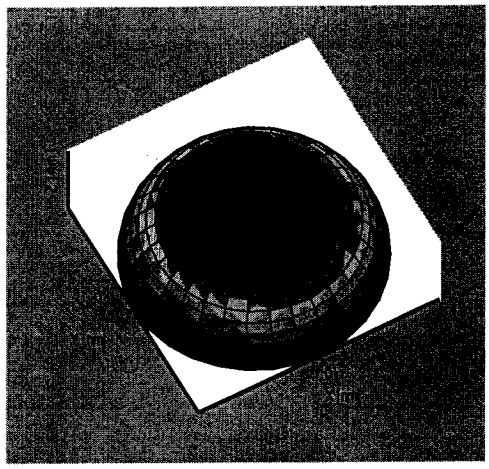

Figure 2.1: Lens Shaped Dot Geometrical Representation

The points *(x, y, z)* lying on the three dimensional dot surface must satisfy equation (2.1.2):

$$\frac{x^2}{R^2}+\frac{y^2}{R^2}+\frac{z^2}{t_{QD}^2}=1 \qquad (2.1.2)$$

II. Theory

The considered physical problem can be stated as the calculation of the energy band structure at the Γ point for a given direct band gap semiconductor heterostructure consisting of a vertical stack of a single or multiple layers of self-assembled lens-shaped quantum dots. To facilitate the physical problem, a Hamiltonian operator based formulation is sought. Mathematically, the task translates to computing the Hamiltonian matrix eigenvalues and eigenvectors. This is accomplished via a customized numerical implementation whose details are presented next.

II. 1 Hamiltonian Formulation

The energy levels and their associated electronic states of a semiconductor structure are governed by the *Schrödinger* equation with an effective matrix Hamiltonian H such that:

$$H\psi = \left(\frac{p^2}{2m_0} + V(r) \right) \psi = E\psi \qquad (2.2.1)$$

The general form of the Hamiltonian can be derived from symmetry while the values of the phenomenological parameters used in the Hamiltonian are determined primarily by the microscopic structure of the crystal. Note that H consists of two additive entities, namely the kinetic Hamiltonian, H_0, and its strain counterpart H_{str}. H_0 includes the influence of remote bands on the conduction and valence band states. H_{str} accounts for strain induced crystal deformation effects. To present a simple picture of the strain effects on the dots, *Pikus and Bir* formulation is adopted herein [20]. Due to the same underlying symmetry, the strain Hamiltonian H_{str} can be obtained from the kinetic part H_0 following few simple substitutions. All the Hamiltonian mathematical details are relegated to appendices A1 and A2. The atomic potential $V(r)$ is replaced by the band edge energy E_{edge} and the effect of the background potential is contained in the effective mass such that the *Schrödinger* equation (2.2.1) can be rewritten as:

$$H\psi = \left(\frac{p^2}{2m^*} + E_{edge} \right) \psi = E\psi \qquad (2.2.2)$$

An electric charge carrier state can be represented phenomenologically by a smoothly varying function, $F = \{F_n\}_{n=1}^{8}$, conventionally referred to as envelope functions such that:

$$\psi(r) = \sum_{n=1}^{8} F_n(r) u_{n0}(r) \qquad (2.2.3)$$

where the basis elements u_{n0} are explicitly given in appendix A1. In the context of the eight band $k.p$ method, there are eight such envelope functions, accounting for conduction band, three valence sub-bands (i.e. heavy hole (HH), light hole (LH) and spin orbit (SO)) as well as their

respective spin degenerate bands.

In a homogenous crystal, denoted as region σ, the multi-component wave function satisfies the *Schrödinger* equation (2.2.2) which can be recast as a set of eight coupled partial differential equations (PDEs) such that

$$\sum_{n=1}^{8} H_{mn}(r,k)\, F_n^{\sigma}(r) = E_m(k) F_m^{\sigma}(r); m = 1(1)8 . \qquad (2.2.4)$$

To render the system (2.2.4) determined over a homogeneous semiconductor region σ, equations (2.2.4) must be augmented by boundary conditions describing the envelope functions behavior across the boundaries of adjacent regions. Recall that the Hamiltonian operator entries contain constant material parameters within each homogeneous region σ but piecewise discontinuous from a homogeneous region to another. The augmented system can then be solved for both the energy levels, Hamiltonian eigenenergies, and the wave functions, Hamiltonian eigenstates.

II. 2 Solution Overview

Some structural features of the considered quantum dot nanostructure are discussed to explain the rationale behind the specific non uniform spatial partition of the unit cell into smaller compositionally-homogeneous sub-regions. The boundary conditions apply at the interfaces of these sub-regions. The Hamiltonian entries are evaluated over both these bulk sub-regions and their surface interfaces.

II.2.1 Domain Partition

Self-assembling of quantum dots is a novel fabrication method that overcomes past growth problems. This process exploits the three-dimensional island growth of highly lattice-mismatched semiconductors. The growth of *InAs* dots on a *GaAs* substrate is a typical example where the lattice mismatch is about 7%. The *Stranski-Krastanow* (SK) growth mode allows deposition of several monolayer thin films called the wetting layer, followed by a cluster nucleation leading to

island formation.

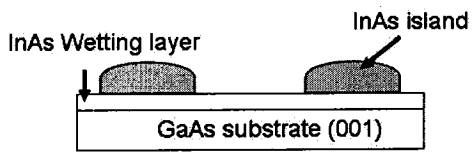

Figure 2.2: Schematic of the Island, Wetting Layer and Substrate Structures

The *InAs* islands buried in *GaAs* work as quantum dots because they are smaller than the carrier's *deBroglie* wavelength both in the transverse (i.e. width) and normal (i.e. thickness) directions. Optical devices with *InAs* island active regions require multiple-layer stacking to enable enough interaction between electrons and the electromagnetic field. The islands become technologically attractive if lateral and vertical arrangement can be manipulated to achieve three-dimensional arrays. The vertical stacking technique helps reducing the dot thickness fluctuations. Assuming in-plane transverse homogeneity, in other words constant center-to-center dot spatial separation as shown in figure 2.3, the column-aligned multiple-layer nanostructure is expected to have a uniform dot width. It ensues from the latter two assumptions that both the transverse and normal spatial dot isolations are uniform throughout the structure.

Based on an uniform spatial dot isolation, the considered unit cell is a cuboid whose transverse cross-section displays both horizontal and vertical symmetries. The transverse section of the computational domain can therefore be restricted to a quarter of the unit cell square cross section. This reduced computational domain is further partitioned into the following five compositionally-homogeneous regions depicted in figure 2.3:

1. The Bulk Barrier (BB) sub-region made out of *GaAs* is uniform along the growth direction (001) in the case of a unit cell comprising a single quantum dot layer.

2. The Dot Core (DC) sub-region made out of *InAs* forms a quarter of the volume enclosed by the lens-shaped dot. On the transverse *xy* plane, the base of DC corresponds to a quarter of a disk with diameter $2R$. The DC region height extends from the bottom to

the inner shell of the dot along the growth direction z, (001).

3. The Inter-Dot (ID) bulk region made out of *GaAs* represents the interstitial volume between two contiguous dots aligned in a columnar fashion. It can be represented by a cylinder of base a quarter of a disk with diameter $2R$ and height extending from the outer dot shell to the spacing thickness between two adjacent layers t_l.

4. The wetting Layer (WL) sub-region made out of *InAs* acts as a very thin sheet on which the *InAs* islands are deposited. The WL can be represented by a quantum well with thickness t_{WL} along the growth direction z, (001).

5. The substrate (SB) bulk sub-region made out of *GaAs*.

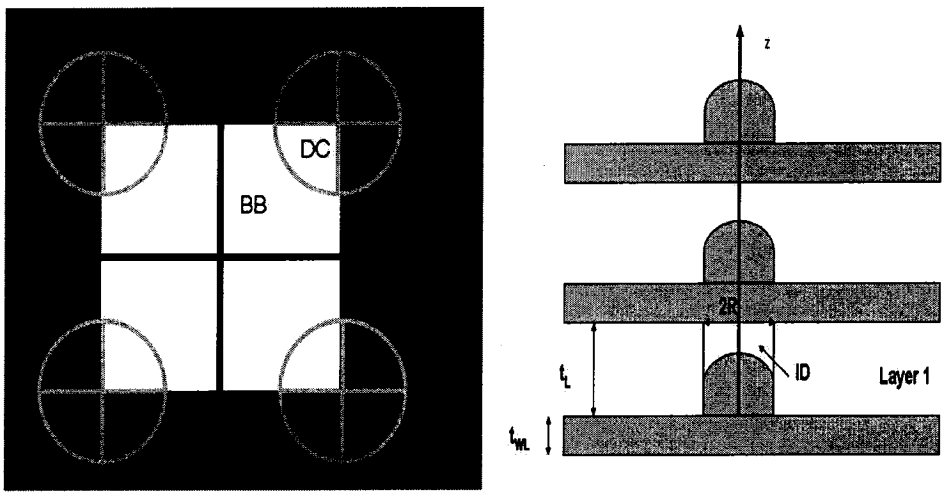

Figure 2.3: Unit Cell Transverse and Normal Cross-Sections Sub-Regions

II.2.2 Strain Distribution

Note that the domain partition described above assumes a piecewise constant strain distribution throughout the homogeneous sub-regions (i.e. constant in the *InAs* dot core and constant in the *GaAs* surrounding barrier volume). Off course this is an oversimplification of the strain spatial profile in typical lattice-mismatched heterostructures. In reality, the strain varies throughout the dot and the barrier material. The atoms in the centre of a dot are further away from the barrier

material and therefore the bonds at the centre of a dot are not as distorted, relative to bulk *InAs*, as those at the periphery. Similarly, the bonds in the barrier material further away from the dot perceive less strain [49]. Nonetheless, the assumption of piecewise constant strain profile in the inhomogeneous unit cell shall hold for very small aspect ratio quantum dots (i.e. ~ 0.1).

The considered partition scheme assumes constant dot size and uniform in-plane dot isolation. This ideal dot distribution does not accommodate a realistic dot placement which is rather random. The dot size fluctuations and non-uniform spatial isolations are critical factors which affect the lasing characteristics of the medium. Such effects may be alleviated to some extent provided improved structure uniformity can be achieved. Self-assembled nanostructures with multiple-layers stacked along the growth direction may be endowed with more structural uniformity, in particular, if the higher-layer islands are grown in correlation with those of the first-layer.

It turns out that the barrier spacing t_l between two adjacent layers is a critical factor in the formation of vertically aligned self-assembled islands. If $t_l < 20nm$, the stacked upper islands form in correlation to the lower-layer islands. In fact, the upper-layer islands form in alignment with the first-layer islands in the vertical direction and expand with an increase in the stacked-layer number. Nonetheless, if t_l decreases to almost the thickness of the dot, the size expansion is suppressed and *almost* equal size islands are closely stacked. In this case, the dots are electronically coupled in the vertical direction and the whole stacked structure works *effectively* as a single large quantum dot [65].

The strain field induced by the islands and impinging on the *GaAs* barrier provides the driving force for self-assembly along the vertical direction. This inevitably leads to revisit the non-spatially-varying strain profile in the barrier. The strain field radial dependence can be estimated by a cubic decay in the distance from the island center, $r = \sqrt{x^2 + y^2 + z^2}$, such that the in-plane strain component ε_{xx}^{GaAs} correction is given by [70]:

$$\varepsilon_{xx}^{GaAs}(r) = 2A_{mat}\varepsilon_0 \frac{\rho_0^3}{r^3}$$

where $A_{mat} = \dfrac{3B_{InAs}}{3B_{InAs} + 2E_{GaAs}/(1+\nu_{GaAs})}$, B_{InAs} is the bulk modulus, E_{GaAs} is Young's modulus, ν_{GaAs} is Poisson's ratio, $\varepsilon_0 (\approx -7\%)$ is the natural lattice mismatch between *InAs* and *GaAs*.

Note that the strain field is weakly dependent on the detailed shape of the islands. For this reason, the islands are assumed to have a symmetric (isotropic) spherical shape with the same volume as that of the lens-shaped dot such that the radius of the sphere is $\rho_0 = \sqrt[3]{\dfrac{R^2 t_{QD}}{2}}$ [15].

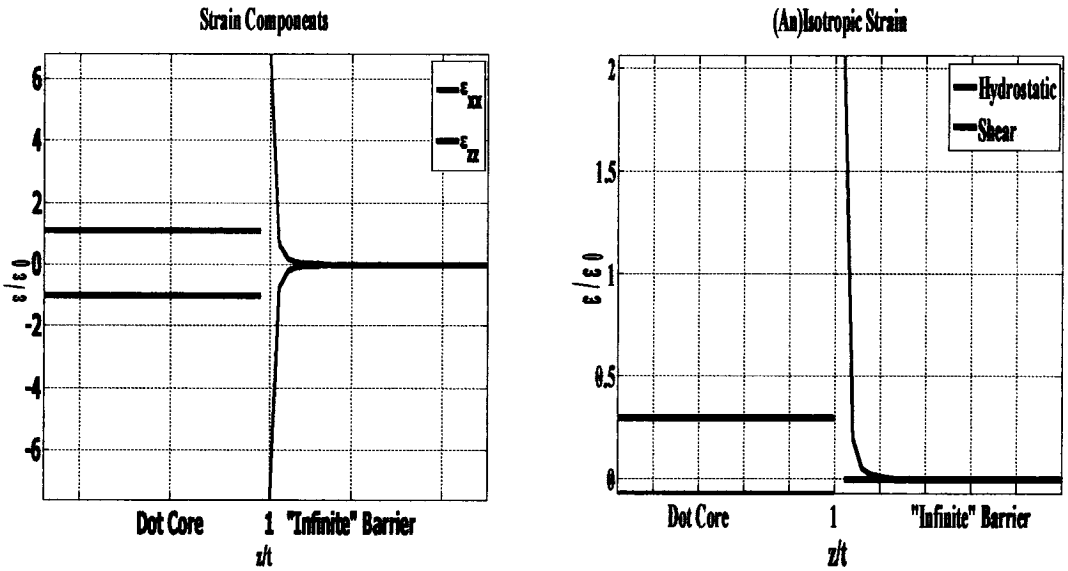

Figure 2.4: Inhomogeneous Strain Spatial Distribution

(a) In-plane and Vertical Components (b) Hydrostatic and Shear Strains

The strain field spatial distribution of a lens-shaped dot with an aspect ratio of ~0.1, projected onto the line joining the centre of the circular base (0, 0, 0) and the apex of the lens (0, 0, t_{QD}), is shown in figure 2.4. The assumption that the strain is constant in the dot is maintained. In the barrier, the shear strain, $2\varepsilon_{zz} - \varepsilon_{xx} - \varepsilon_{yy}$, decays further away from the dot surface whereas the

hydrostatic strain, $\varepsilon_{xx}+\varepsilon_{yy}+\varepsilon_{zz}$, is confined to the dot alone. The strain components observe an abrupt jump at the tip of the lens-shaped dot (i.e. $\frac{z}{t_{QS}}=1$) given the highest lattice-mismatch at this point. It can also be seen from figure 2.4(b) that the strain is biaxial tensile in the barrier with a negative shear strain (recall that $\varepsilon_0<0$).

II.2.3 Boundary Conditions

The regions $\sigma = BB, DC, ID, WL, SB$ have three types of interfaces $I^{\sigma,\sigma'}=\sigma \bigcap_{\sigma\neq\sigma'}\sigma'$ such that:

1. A planar interface between the dot core and the wetting layer. The interface $I^{DC,WL}$ is exactly the dot base which is a disk of diameter $2R$ lying onto the transverse xy plane. Note that both intersecting regions are made of the same material.

2. A three-dimensional interface between the dot core and the surrounding barrier material. The interface $I^{DC,BB}$ is exactly the dot shell given by equation (2.1.2).

3. A planar interface between the wetting layer and the substrate. The interface $I^{WL,SB}$ is exactly the transverse plane common to the substrate and the wetting layer beneath it.

The envelope functions $F_n^{\sigma}(r)$ are expanded over the complete and orthonormal set of three-dimensional *Fourier* series, such that

$$F_n^{\sigma}(r)=\sum_{\alpha\beta\kappa}^{\infty} F_n(\alpha,\beta,\kappa)\phi_{\alpha\beta\kappa}(x,y,z);\ \ n=1(1)8 \qquad (2.2.5)$$

where

$$\phi_{\alpha\beta\kappa}(x,y,z)=\frac{1}{\sqrt{XYZ}}\exp\left[2\pi i\left(\alpha\frac{x}{X}+\beta\frac{y}{Y}+\kappa\frac{z}{Z}\right)\right] \qquad (2.2.6)$$

The discrete *Fourier* series assume that the overall structure is periodic with periods X,Y and Z along the x, y and z directions respectively. The angular momenta states $F_n(\alpha,\beta,\kappa)$ bear no mention of the region index σ. This implies that the *same* expansion coefficients apply to each

region σ. Therefore, by construction the envelope functions F_n^σ satisfy the mathematical continuity condition at each interface since the functions $\phi_{\alpha\beta\kappa}(x,y,z)$ are themselves continuous across all interfaces. Nonetheless, the material parameters observe a discontinuity across the intersection of two compositionally different regions. To comply still with the physical matching boundary conditions demanding the continuity of the tangential electromagnetic field component (i.e. continuity of the normal (gradient) component of the current) across theses particular interfaces, a symmetrization prescription needs to be applied as described in the next subsection.

II.2.4 Hermitian Property

The spatial dependence of any material parameter or strain component $Q(r)$ is expressed in terms of step functions for the interfaces at $r=r_0$, where material 1 is on one side and material 2 is on the opposite side of the interface. For example, along the transverse x direction:

$$Q(x) = Q_1 + (Q_2 - Q_1)\theta(x - x_0) \text{ where } \theta(x - x_0) = \begin{cases} 0 & x < x_0 \\ 1 & x \geq x_0 \end{cases} \qquad (2.2.7)$$

The parameters involving spatial derivatives result in delta terms at the internal interfaces. The delta terms arise following the differentiation of the Heaviside function $\theta(x - x_0)$.

The position-dependent parameters must observe the following symmetrization prescriptions to ensure that the Hamiltonian is hermitian [11,27]:

$$Q\partial_\mu \rightarrow \frac{1}{2}\left[Q(r)\partial_\mu + \partial_\mu Q(r)\right] \qquad Q\partial_\mu\partial_\nu \rightarrow \frac{1}{2}\left[\partial_\mu Q(r)\partial_\nu + \partial_\nu Q(r)\partial_\mu\right] \qquad (2.2.8)$$

The Hamiltonian hermitian (i.e. self-adjoint) property ensures that all eigenenergies are real.

In the software implementation, H is hermitian by construction so that only the upper triangular entries are evaluated first, then the complex conjugate of the non-zero entries are assigned to their lower triangular homologous by symmetry across the main diagonal (see figure 2.5). It follows that all main diagonal entries must be real such that

$$H_{mn}(\alpha,\beta,\kappa,\alpha',\beta',\kappa') \equiv H^{*}_{nm}(\alpha',\beta',\kappa',\alpha,\beta,\kappa).$$

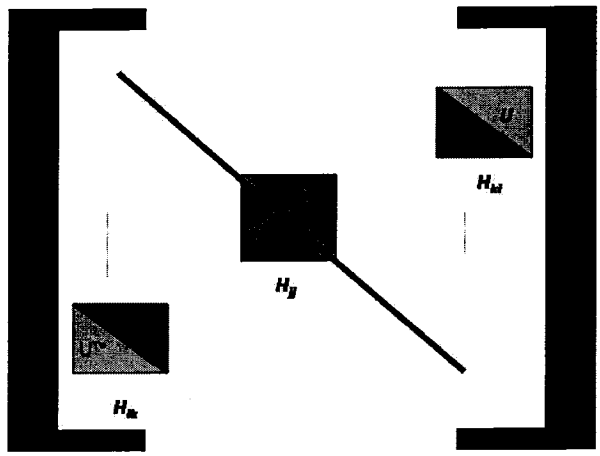

Figure 2.5: Global Hermitian Property of the Hamiltonian Matrix

II.2.5 Matrix Elements

The associated eigenvalue problem can be written in concise matrix form such that the resultant 8×8 matrix has elements $H_{nm}(r,\nabla)$. Incorporating equation (2.2.5) into (2.2.4), the eight coupled PDEs (2.2.4) are rewritten as follows:

$$\sum_{n=1}^{8} H_{mn}(r,\nabla)\left(\sum_{\alpha\beta\kappa}^{\infty} F_n(\alpha,\beta,\kappa)\phi_{\alpha\beta\kappa}(x,y,z)\right) = E_m(\alpha,\beta,\kappa)\sum_{\alpha\beta\kappa}^{\infty} F_m(\alpha,\beta,\kappa)\phi_{\alpha\beta\kappa}(x,y,z);\ m = 1(1)8 \tag{2.2.9}$$

Operating the derivatives $H_{mn}(r,\nabla)$ on the *Fourier* series expansion of the envelope functions would destroy its convergence. To avoid such scenario, the equations (2.2.9) are multiplied by $\phi^{*}_{\alpha\beta\kappa}(xyz)$ and integration is carried out over the unit cell volume Ω (i.e. orthogonality domain) given by $\Omega=\left\{-\frac{X}{2}\le x\le\frac{X}{2},-\frac{Y}{2}\le y\le\frac{Y}{2},0\le z\le Z\right\}$. The reduced computational domain is $\Omega_{red}=\left\{0\le x\le\frac{X}{2},0\le y\le\frac{Y}{2},0\le z\le Z\right\}$. The resultant matrix eigenvalue problem now reads:

$$\sum_{n=1}^{8}\sum_{\alpha\beta\kappa}^{\infty} H_{mn}(\alpha',\beta',\kappa',\alpha,\beta,\kappa)F_n(\alpha,\beta,\kappa) = E_m(\alpha,\beta,\kappa)F_m(r); m = 1(1)8 \qquad (2.2.10)$$

where the matrix entries $H_{mn}(\alpha',\beta',\kappa',\alpha,\beta,\kappa)$ are given by:

$$H_{mn}(\alpha',\beta',\kappa',\alpha,\beta,\kappa) = \iiint_{\Omega} dxdydz\, \phi^{*}_{\alpha'\beta'\kappa'}(xyz) H_{mn}(r,\nabla)\phi_{\alpha\beta\kappa}(xyz). \qquad (2.2.11)$$

The unit cell volume Ω comprises five types of bulk sub-regions $\sigma = BB, DC, ID, WL, SB$ and three types of internal-interfaces $I^{\sigma,\sigma'}$. The sum of the contributions from each sub-region and internal interface yields the overall matrix element such that:

$$H_{mn}(\alpha',\beta',\kappa',\alpha,\beta,\kappa) = \sum_{\sigma} B^{\sigma}_{mn}(\alpha',\beta',\kappa',\alpha,\beta,\kappa) + \sum_{I^{\sigma,\sigma'}} S^{\sigma,\sigma'}_{mn}(\alpha',\beta',\kappa',\alpha,\beta,\kappa) \qquad (2.2.12)$$

where the bulk term B^{σ}_{mn} is given by:

$$B^{\sigma}_{mn}(\alpha',\beta',\kappa',\alpha,\beta,\kappa) = \iiint_{\sigma} dxdydz\ \ \phi^{*}_{\alpha'\beta'\kappa'}(xyz) H_{mn}(r,\nabla)\phi_{\alpha\beta\kappa}(xyz) \qquad (2.2.13)$$

and the internal-interface term $S^{\sigma,\sigma'}_{mn}$ is given by the following surface integral:

$$S^{\sigma,\sigma'}_{mn}(\alpha',\beta',\kappa',\alpha,\beta,\kappa) = \oiint_{I^{\sigma,\sigma'}} dS\phi^{*}_{\alpha'\beta'\kappa'}(xyz) H_{mn}(r,\nabla)\phi_{\alpha\beta\kappa}(xyz)\hat{n} \qquad (2.2.14)$$

The operators $H_{mn}(r,\nabla)$ contain only material parameters, first and second order spatial derivatives which are constant within the homogeneous bulk sub-region σ. This observation allows the bulk integrals B^{σ}_{mn} to have an analytic expression in the form of an energy rescale of the following integral:

$$\frac{1}{XYZ}\iiint_{\sigma} dxdydz\ \ \exp\left[2\pi i\left((\alpha-\alpha')\frac{x}{X} + (\beta-\beta')\frac{y}{Y} + (\kappa-\kappa')\frac{z}{Z}\right)\right] \qquad (2.2.15)$$

On the other hand, the operators $H_{mn}(r,\nabla)$ contain delta terms to account for the material constants and slope discontinuities across the internal interface $I^{\sigma,\sigma'}$. Each interface has a dual

boundary role since $I^{\sigma,\sigma'}$ acts as the inner-boundary of region σ as well as the outer-boundary of region σ'. This implies that the regions σ and σ' have unit normal vectors, $\hat{n}$ and $\hat{n}'$ respectively, pointing in opposite directions such that $\hat{n}' = -\hat{n}$. The surface integral $S_{mn}^{\sigma,\sigma'}$ therefore picks up only the contribution from the interface discontinuity of the operator:

$$H_{mn}(r,\nabla) = H_{mn}^{\sigma}(r,\nabla) - H_{mn}^{\sigma'}(r,\nabla) \tag{2.2.16}$$

In view of the Hamiltonian interface discontinuity, the surface integral (2.2.14) does not pick up any contribution from the external interface where periodic conditions apply. Likewise, the same observation applies at interface $I^{DC,WL}$ where both sides of the interface consist of the same material. These observations allow the surface integrals $S_{mn}^{\sigma,\sigma'}$ to have an analytic expression in the form of an energy rescale of the following integral:

$$\frac{1}{XYZ}\oiint_{I^{\sigma\sigma'}} dS \exp\left[2\pi i\left(\left(\alpha-\alpha'\right)\frac{x}{X}+\left(\beta-\beta'\right)\frac{y}{Y}+\left(\kappa-\kappa'\right)\frac{z}{Z}\right)\right]\hat{n} \tag{2.2.17}$$

In general, the integrals (2.2.15) and (2.2.17) do not lend themselves to analytical evaluation over the sub-regions σ and the interfaces $I^{\sigma,\sigma'}$ respectively.

III. Software Implementation

The Hamiltonian evaluation relies on the evaluation of integrals (2.2.15) and (2.2.17) for various quantized states. The local Hamiltonian elements must then be placed in a global matrix according to their respective conduction and valence band quantized states.

III.1 State Index

An index numbering scheme must be used so that a computed eigenvalue $E_l(\alpha,\beta,\kappa)$ can be unambiguously designated with its band l and quantized state (α,β,κ). For a local Hamiltonian

$H_{mn,}$ the local row i_{mn} is obtained from the conduction state (α,β,κ) whereas the local column j_{mn} is obtained from the valence state (α',β',κ') for each band l. This is easily accomplished according to the following mappings:

$$i_{mn}(\alpha,\beta,\kappa)=(\kappa-1)N^2+(\beta-1)N+(\alpha-1) \tag{2.2.18}$$

$$j_{mn}(\alpha',\beta',\kappa')=(\kappa'-1)N^2+(\beta'-1)N+(\alpha'-1) \tag{2.2.19}$$

where $N=2J+1$ denotes the total number of waves in each spatial direction such that $N\in\{-J,-J+1,\ldots,0,\ldots,J-1,J\}$.

The quantized states consist of all possible combinations $\{(\alpha,\beta,\kappa):-J\le\alpha,\beta,\kappa\le J)\}$ Additionally, the numbering scheme must map the local entries (i_{mn},j_{mn}) into their corresponding global entries (i,j) according to the following mappings:

$$i(\alpha,\beta,\kappa)=N^3(m-1)+i_{mn}(\alpha,\beta,\kappa) \tag{2.2.20}$$

$$j(\alpha',\beta',\kappa')=N^3(n-1)+j_{mn}(\alpha',\beta',\kappa') \tag{2.2.21}$$

III.2 Eigensolution Computing

Once the Hamiltonian is set up, an eigensolver is applied in order to compute the Hamiltonian eigenenergies and their corresponding eigenstates. Keeping in mind that the eigenenergies near the band gap are of special interest, only few inner eigenvalues need then to be solved for. The partition approach discussed previously results in a far smaller Hamiltonian rank than do typical discretized meshes described in the literature. As a matter of fact, using 15 waves in each of the three directions results in a Hamiltonian rank of almost $3.10^3\times3.10^3$ whereas the typical reported sizes are at least $10^5\times10^5$. As such, partial or even full diagonalization of the Hamiltonian may be numerically realizable. The software implementation actually uses the *Jacobi-Davidson* method which computes a partial generalized *Schur* decomposition of the Hamiltonian matrix. The decomposition leads to a pre-specified number of eigensolutions.

III.3 Accelerated Version

A close inspection of the matrix element expressions (2.2.15,17) reveals that quasi-redundant integral evaluations are carried out were it not for the small perturbation in the conduction and valence quantized numbers. Near the Γ point, especially, the exponential integrand can be expanded into its three-dimensional *MacLaurin series* which can be truncated up to a desired accuracy order. A linear approximation comprises eight additive terms meanwhile a quadratic approximation comprises nineteen extra terms. The practical aspect of the fast version stems from the fact that each *MacLaurin* exponential approximant term splits the matrix element integral into two factors, a core integral and a constant multiplier. The core integral needs to be evaluated *only once* and can at most times be integrated analytically. The constant multiplier affecting the core integral consists of the varying quantized state terms $\left(\alpha-\alpha'\right),\left(\beta-\beta'\right),\left(\kappa-\kappa'\right)$.

The merit of the accelerated version is to provide quick estimates for the eigenenergies and eigenstates. It should be stressed that the set of the exponential approximants may not satisfy the orthogonality (normality) conditions. Therefore, the accelerated version eigensolutions may actually be crude approximations.

IV. Software Validation

The *k.p* software validation is quite intricate because it is subject to many adjustable degrees of freedom.

IV.1 Input Material Parameters

The controversial material parameters cause input subtleties which must be reckoned with prior to simulation. Primarily, the crucial parameter for the energy level calculations with respect to the *GaAs* barrier is the heterojunction band lineup. Unfortunately this is the least known parameter. Given that *GaAs* is the most technologically studied semiconductor, many of its band structure

parameters are known with relatively more accuracy than for any other compound. To set aside the replete but controversial reported parameters in the literature, *Vürgaftman et. al.* [68] have presented a comprehensive and up-to-date compilation of the band parameters for the technologically important III-V zinc blende and würtzite compound semiconductors. This is a tremendous achievement since it provides an absolute scale for heterostructure band offsets and thus it allows materials to be aligned relative to one another. In the context of this work, the useful parameters for the chosen dot and barrier materials, *InAs* and *GaAs* respectively, are shown in table A1 which is relegated to appendix A3.

The anisotropic effective masses in the z-crystallographic direction (i.e. growth direction (001)) for the conduction and valence bands are given in terms of the *Luttinger* parameters such that:

$$m_{hh}^{*} = \frac{m_0}{\gamma_1 - 2\gamma_2} \text{ and } m_{lh}^{*} = \frac{m_0}{\gamma_1 + 2\gamma_2}.$$

Another source of difficulty emanates from the fact that all available material parameters are given for bulk structures. When dealing with lower dimension materials, many parameters, such as electron and hole effective masses change to reflect the higher quantum confinement dimension. The zero dimensional parameters used in the simulations are given in table A1 of Appendix A3 and their corresponding bulk ones are included between brackets wherever applicable.

IV.2 Convergence Analysis

The unit cell size and the total number of waves are two adjustable degrees of freedom to ensure convergence of the computed results. In the absence of rigorous error analysis, which would predict error estimates in terms of some norm of the Hamiltonian matrix $\|H\|_{2,-}$ otherwise, a practical convergence criterion may be selected. Such criterion is founded on the basis of two observations. First, the quantum dot discrete eigenenergies must somewhat, in the order of a tenth of 1 meV, be independent of the unit cell size starting at an optimal choice. One can settle for the

smallest unit cell volume which warrants little change in the calculated *dot energy levels* thereafter. One must be cautious though since continuously increasing the size of the confining box to "infinity" is conducive to the onset of the wetting layer and the barrier continua states. Given that the zero dimensional confined eigenenergies are the highlight of the current work, little appreciation is given to the continuum energies. Emphasis is rather placed on conduction energies lying under the conduction band offset (CBO) or conduction separation energy. Similarly, only valence energies lying above the valence band offset (VBO) are targeted.

Second, the number of waves used along each direction must be practically finite. This number depends on how much the material parameters vary along the same direction. One way to settle for a "good" minimum number of waves is to pick a particular threshold above which the eigenenergies are barely altered. Note that due to computing resources limitations such as memory space and execution time, the number of waves cannot be increased to a potentially high number (e.g. greater than 15 waves). In such circumstances, it may be necessary to extrapolate the calculations to a more accurate final value.

To elucidate the convergence criterion, a nanostructure consisting of one layer of almost flat lens-shaped *InAs* dots of volume[3] $25\times25\times2.5$ nm^3 deposited onto a wetting layer 0.5 nm thick and surrounded by *GaAs* barrier 3 nm thick is considered for illustration. The aim is to compute few conduction and valence energy levels near the bandgap for these low aspect ratio, 0.1, dots. The computed electronic structure is shown next in figure 2.6.

The dot and surrounding barrier volumes are encompassed into a large "infinite" wall box of size $35\times35\times20$ nm^3 in order to limit the rank of the Hamiltonian and impose periodic boundary wave function conditions at the edges of the box. Indeed, following an increase in the selected box size the energy states confined in the dot remain nearly unaffected.

---

[3] This is actually the equivalent cubic volume

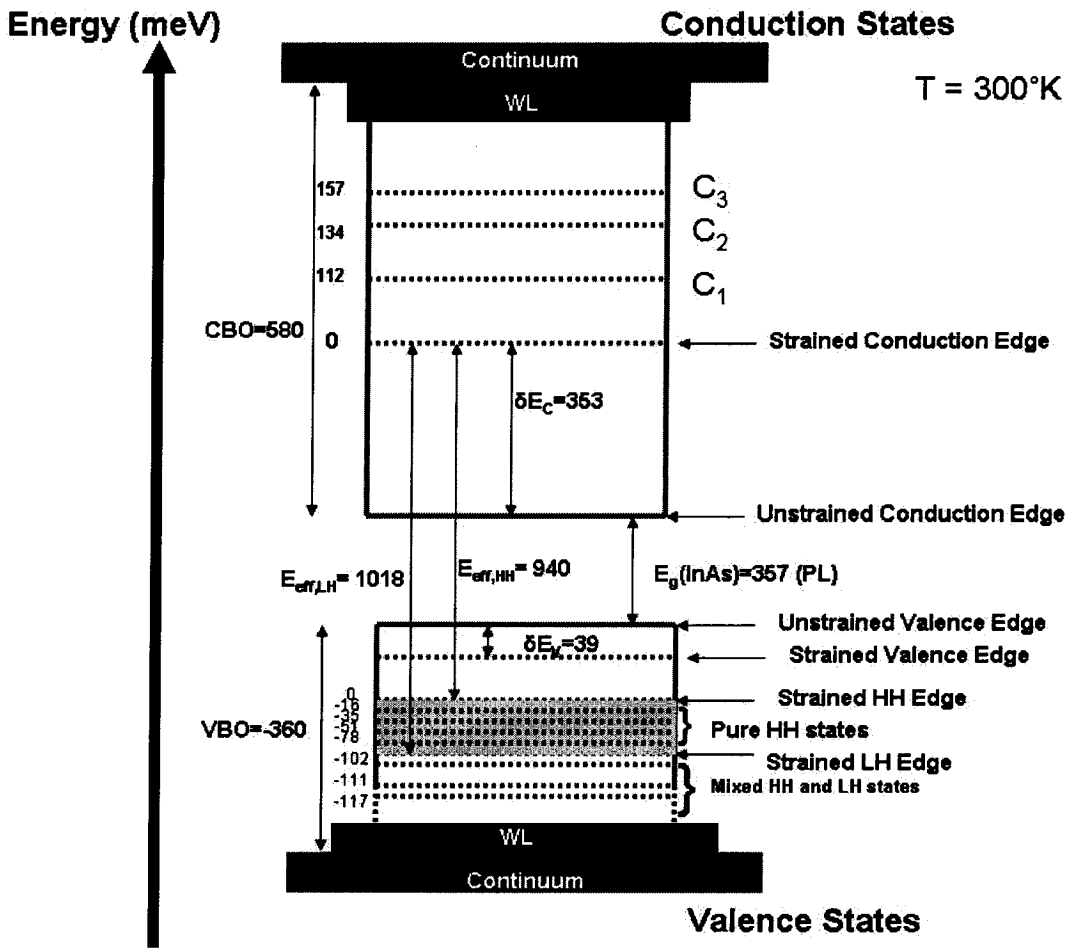

Figure 2.6: Electronic Structure of an *InAs/GaAs* Lens-Shaped Dot

The electronic structure in figure 2.6 shows more than one conduction confined state due to the strong confinement especially along the growth direction. This is in agreement with the inherent atom-like properties of small size dots. Few valence states are equally shown. The pure heavy hole confined states are situated between the heavy and light hole strained edges and extend over an energy range of 78 meV. The intraband mixing of heavy and light hole states takes place between the light hole strained edge and the valence band offset (VBO) and extends over an energy range of 52 meV. It is worthwhile noting that no *confined* spin orbit state is predicted since the spin orbit split-off energy is larger than the VBO in this case. Spin orbit states are found

subsequently in the wetting layer or the continuum. The reader is referred to section IV.4.1 for a more elaborate discussion on the strain effects on the band structure.

Extending the convergence analysis to the normalized eigenstates power $|F_n|^2$ spectra allows to visually deciding on an optimum number of waves to be used. Figure 2.7 reveals, in the case of 11 waves in each of the three spatial directions, that the power is widely spread over the whole range of quantized states with sharp peaks towards the electron and hole spectra ends. Meanwhile, in the case of 15 waves, the power is mainly concentrated over a broad vicinity around the middle quantized state leaving nothing but negligible noise components toward the head and tail ends of the spectra. The last two observations suggest that an optimum wave number must be higher than 11 but lower than 15 waves in each direction.

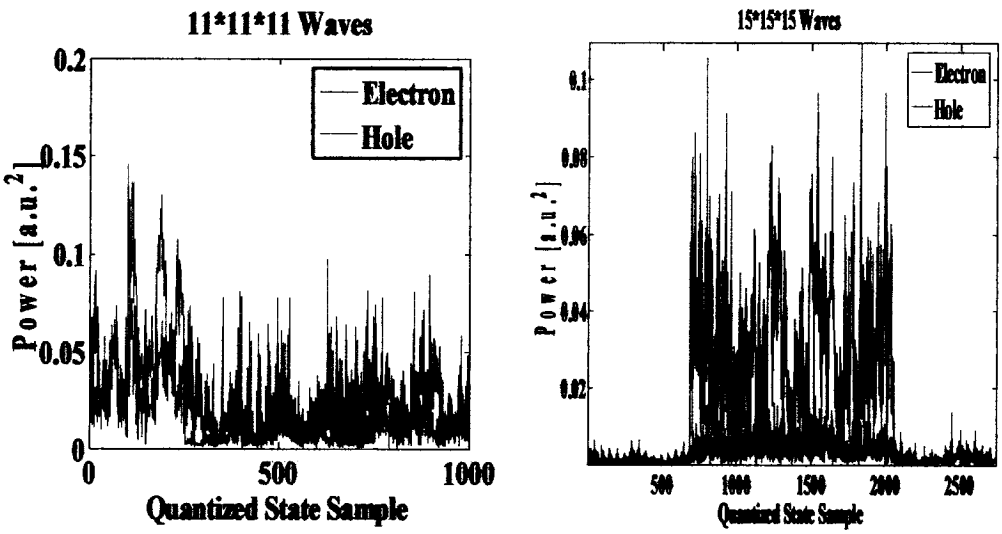

Figure 2.7: Normalized Eigenstate Power Spectra

To closely monitor the convergence behavior, the fast version of the software is executed for an increasing wave count up to a maximum of 15 waves in each direction. The calculated confined energy level approximations exhibit slow and monotonic convergence. The slow convergence is further exacerbated by the repeated piecewise discontinuities of the material parameters across

the boundary interfaces. It turns out that the convergence to an accurate energy level is computationally prohibitive. Increasing the wave count above 15 waves in each direction, requires significant amount of swap memory and CPU execution time which eventually would negate the benefit of the fast version. To remedy this situation, the key monotonic convergence behavior is capitalized upon and recourse may be made to *Richardson* extrapolations. The crude conduction and valence energies $E_C^{(0)}(J)$ and $E_V^{(0)}(J)$ are used as guesstimates and are further refined through repeated extrapolations to more accurate final values such that

$$E_{band}^{(n)}(J) = \frac{2^n E_{band}^{(n-1)}(J) - E_{band}^{(n-1)}(J-2)}{2^n - 1}; J = 1(2)7, \tag{2.2.22}$$

where the subscript "band" in equation (2.2.22) refers to either conduction or valence and n is the order of *Richardson* extrapolation. The convergence accelerating approach is only necessary if a non-satisfactory energy convergence is witnessed for a total wave count of $15 \times 15 \times 15$.

IV.3 Quantitative Validation

Some considerations must be made before comparing the computed and measured energies. Throughout the following analysis, the available experimental data [49] is used as benchmark. In an effort to fit the current model results to the experimental ones, appropriately selected effective masses and confinement potentials are parametrically varied until the computed quantum dot emission energies are reconciled with their corresponding photoluminescence (PL) measurements [49] at a temperature of 77 °K. By doing so, it is hoped to account for effects due to the variation of strain and composition across the dot, as well as other effects the model does not account for.

The dot emission energies (i.e. interband transition energies) are given by

$$E_{emission} = E_C^{(\alpha,\beta,\kappa)} - E_V^{(\alpha,\beta,\kappa)} \tag{2.2.23}$$

where the zero level energy corresponds to the unstrained valence band edge in the dot. The transition selection rule in quantum dots, which is not discussed here, translates to a requirement

that the electron and hole quantized states are identical, $(\alpha, \beta, \kappa) \equiv (\alpha', \beta', \kappa')$.

Dot size [nm^3]	Computed [eV]		Measured [49] [eV]		% Absolute Relative Error
23×23×5	g[4]	1.187	g	1.20	1.08
	e[5]	1.273	e	1.28	0.55
23×23×6	g	1.133	g	1.15	1.48
	e	1.245	e	1.23	1.21
28×28×7	g	1.065	g	1.05	1.41
	e	1.137	e	1.12	1.49

Table 2.1: Comparison of *k.p.* Computed and (PL) Measured Transition Energies

The computed transition energies fit within a remarkable ±2% relative error margin from their measured counterparts at a temperature of 77°K as shown in table 2.1. Also, the spacing between the ground and first excited state energies is nearly 80 meV for both the computed and measured results. This is clear evidence of the reliability of the accelerated method..

IV.4 Qualitative Validation

Thus far, two aspects of the numerical computations have been successfully verified. Effectively, the convergence of the computed energy states yields remarkably close transition energies to the reported experimental ones. It remains now to ensure that the numerical results adhere to the anticipated physics of zero dimensional media. Following are some qualitative test cases designed

[4] Ground state

[5] First excited state

to complement the convergence and quantitative tests, thereby, offering a comprehensive validation test hierarchy.

IV.4.1 Test Case 1: Strain Effects on Electronic Structure

The shear strain components may be appreciable, especially at the interfaces, for high aspect ratio geometries. In such cases, a significant correction of the energy levels due to piezoelectric field is expected. Therefore, for rigorous strain treatment, a discretization method taking into account a varying strain profile within the dot and barrier is advised.

The computed electronic spectrum of a small aspect ratio (i.e. 0.1) lens-shaped dot shown in figure 2.6 meets however the anticipated effects peculiar to a biaxial compressive (tensile) strain in the dot (barrier). The compressive strain hydrostatic component induces both an upward shift on the conduction band edge by an energy amount, $\delta E_C = a_c(\varepsilon_{xx} + \varepsilon_{yy} + \varepsilon_{zz})$, of 352.6 meV and a downward shift, $\delta E_V = a_V(\varepsilon_{xx} + \varepsilon_{yy} + \varepsilon_{zz})$, on the valence band edge by an energy amount of 39.2 meV. Moreover, the compressive strain shear component affects only the valence subbands in that it induces an identical energy shift, $\delta E = b(2\varepsilon_{zz} - \varepsilon_{xx} - \varepsilon_{yy})$, both on the heavy and light hole subbands but in opposite energy directions by an energy amount of 269.4 meV. On the other hand, the compressive strain induces a lift up in the degeneracy between the heavy and light hole bands. This is materialized by two distinct effective bandgap energies such that $E_{HH}^{eff,QD} = 939.8meV$ ($\lambda_{HH}^{eff} = 1.32\mu m$) and $E_{LH}^{eff,QD} = 1018.1meV$ ($\lambda_{LH}^{eff} = 1.22\mu m$).

The band gap energy dilation in the strained *InAs* dot is due to the aggregation of the hydrostatic and shear strain shift effects on the band structure. The dilation is exactly the band gap energy stretch between the unstrained *InAs* bulk (i.e. 357 meV at T = 300°K) and the strained *InAs* dot as shown in figure 2.6. The deformation potentials a_C, a_V and b are given in table A1 (Appendix *A3).* The distribution in figure 2.4 shows very large strain components which would result in band splitting energies comparable to the interband separation energies in the bulk *InAs* material. This

consideration is adequately handled by the eight band *k.p* method because it accounts for the influence of remote valence bands on the conduction band. Alternative approaches where the valence and conduction bands are decoupled may actually prove inadequate in such circumstance.

IV.4.2 Test Case 2: Quantum Confinement Effect on Eiegenergy

Based on the results from table 2.1, the energy of the confined conduction and valence levels decreases following a decrease in the dot thickness. Alternatively stated, the bound-to-bound interband transition energy gets blue-shifted as a result of a stronger confinement as shown in figure 2.8. Similarly, the energy of the confined levels decreases pursuant to a lateral expansion of the dot. In summary, figure 2.8 depicts the anticipated decrease in the bound-to-bound transition energy following an increase of the dot volume.

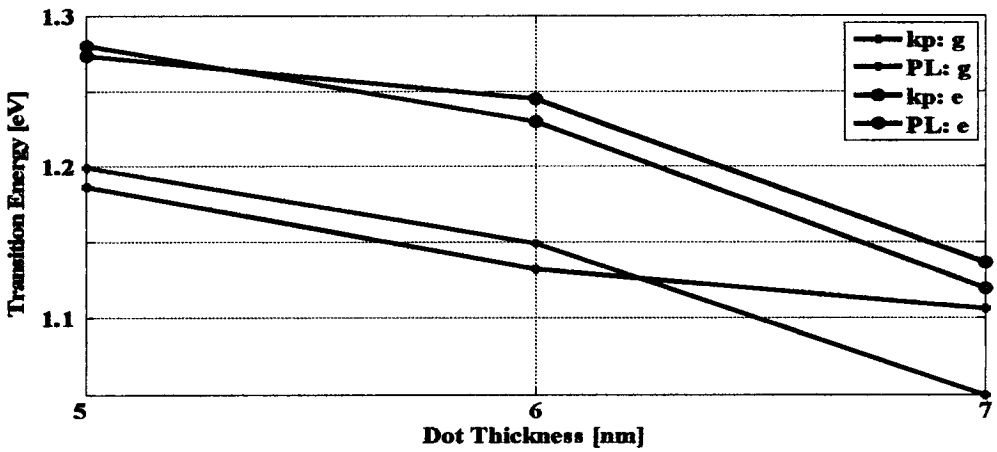

Figure 2.8: Quantum Confinement Effect on Transition Energy

IV.4.3 Test Case 3: Quantum Confinement Effect on Eigenstate

Two eigenstates near the band edge of the conduction and heavy hole bands are considered. The magnitudes of their corresponding normalized envelope functions are projected onto the *xz* plane. The spatial distributions of the normalized envelope functions are shown for a thickness varying between -0.5 nm to 0.5 nm. This illustrates the carrier densities near the base of the dot and

further into the wetting layer. It can be seen from figure 2.9.a that the conduction state electron is strongly confined (very dark distribution) to the middle of the dot. This central confinement is less pronounced for the hole (lighter distribution) as depicted in figure 2.9.b.

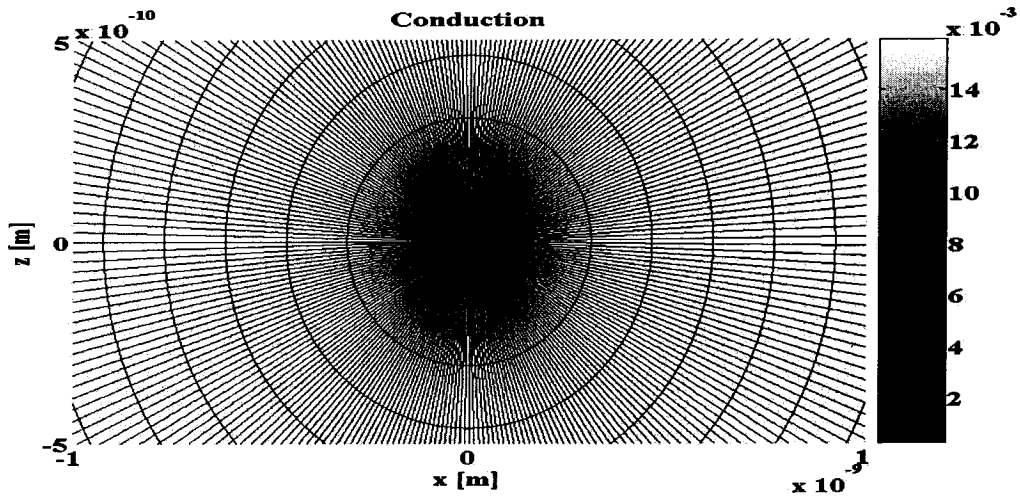

Figure 2.9.a: Envelope Function Magnitudes $|F|^2$ through the xz plane

The electron has a more elongated distribution along the confinement direction which permeates the wetting layer further than in the case of the hole. This may be attributed to the predominant *s*-type nature of the conduction wave function.

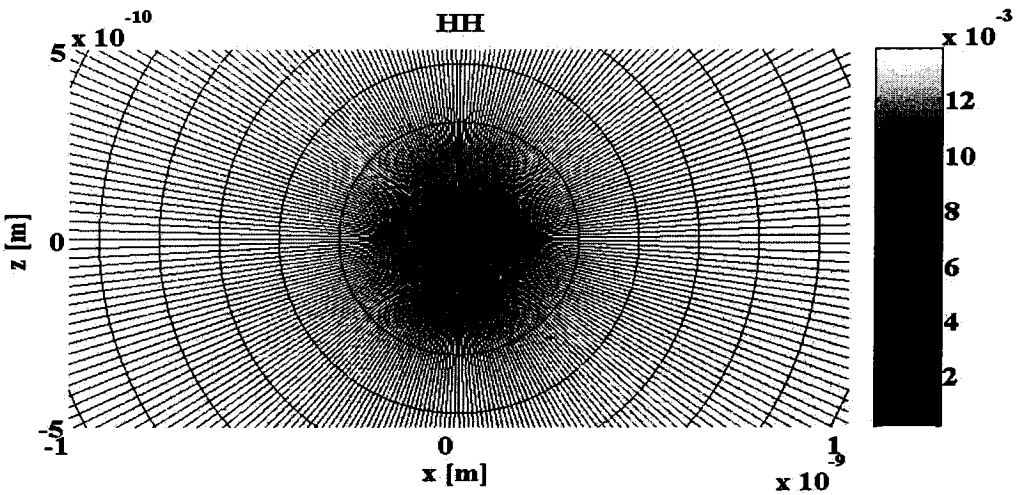

Figure 2.9.b: Envelope Function Magnitudes $|F|^2$ through the xz plane

On the other hand the hole exhibits a wider distribution along the lateral confinement direction than the electron does suggesting a stronger hole confinement to the dot circular base.

IV.4.4 Test Case 4: Repeated Vertical Close Stacking Effect

The tunability of the emission wavelength is often a highly desired feature for many optoelectronic devices. It can be artificially enabled by controlling the confined energy levels of the quantum nanostructure. One way to achieve this goal is to use vertical stacking of multiple quantum dot layers. The most practical advantage of the stacking technique is size control. Thus by choosing the barrier spacing thickness, the dot size and the quantized energies are tuned to meet the device requirements.

Figure 2.10 exhibits the repeated stacking effect on the ground emission wavelength for a nanostructure consisting of up to eight vertically stacked *InAs* quantum dot layers which are spaced by 3 nm thick *GaAs* barriers. For simplicity, the dots are assumed to undergo only a uniform-rate lateral expansion such that the first layer islands are 23 nm wide whereas those of the eighth layer are 44 nm wide. All islands are assumed to be 2.5 nm thick regardless of the layer level.

Additional vertical stacked layers inflict a tangible reduction in energy spacing between the discrete confined states yielding the observed red shift of the emission spectra in figure 2.10, in other words, the increase in the ground emission wavelength. This fact should not be surprising at all since the multi-fold closely stacked structure effectively behaves as a large volume dot. The emission spectra red shift characteristic is thus in utter agreement with the conclusions drawn from figure 2.8.

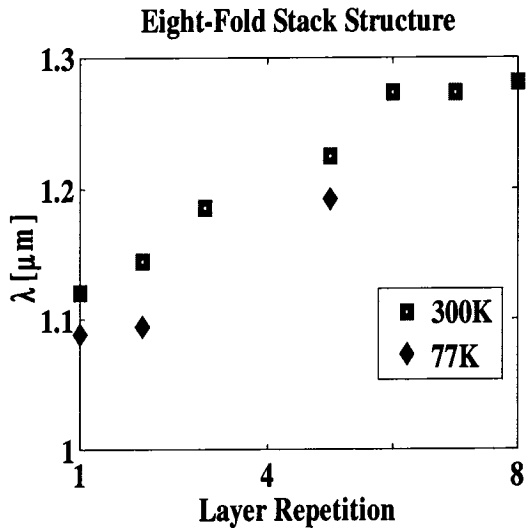

Figure 2.10: Vertical Stacking Effect on Ground Transition Energy

V. Conclusions

Successful calculations of the eigenenergies and eigenstates of *InAs/GaAs* quantum dot nanostructures have been carried out within the framework of eight band *k.p.* formalism. The merit of the accelerated implementation resides in its simplicity, reliability and execution speed. The produced eigenenergies fit quantitatively the corresponding PL measurements and agree qualitatively with the anticipated physical properties of quantum dots.

Chapter Three

Susceptibility Analysis

The three-dimensional quantum confinement affects the electronic density of states, which in turn, impacts the semiconductor material response following the light-matter interaction. The material electrical susceptibility quantifies such response. The real and imaginary parts of the susceptibility give expressions for the refractive index and material gain respectively. All susceptibility calculations are done within the framework of a resonant two-level energy system.

The quantum dot material gain is polarization sensitive due to geometrical asymmetries in the dots. The polarization dependence can be implicitly expressed in the dipole transition strength. The anisotropy factors of each interband transition type are derived and shown to satisfy a momentum conservation rule under both TE and TM polarizations.

Numerical simulations are provided in the case of lens-shaped *InAs* islands grown onto a thin wetting layer made out of the same binary compound and surrounded by *GaAs* potential barrier.

The optical gain spectra of these structures are closely examined. The dynamic performance through the differential gain and the noise characteristics through the linewidth enhancement factor are alluded to.

I. Introduction

The transition of an electron between the conduction and valence bands occurs by the transfer of the interband transition energy between the electron and photons. The light-matter interaction is facilitated by the electron and hole spatial confinement and becomes more efficient for highly dimensional quantum confinement. Owing to the high localization of carriers in quantum dots, the optical transitions occurring near the band edges exhibit attractive characteristics. Direct band gap semiconductor materials can efficiently host such interband transitions whereby the conduction

band minimum and valence band maximum are at the same electron wave vector position $\vec{k}_c \cong \vec{k}_v = \vec{k}$. Consequently, the interband optical transition must occur perpendicularly in the energy band dispersion diagram.

The electron-hole recombination must *a priori* satisfy a wave vector selection rule. Pertaining to quantum dots, the adopted transition selection rule translates to a requirement that the electron and hole quantized states are identical, $(\alpha,\beta,\kappa) \equiv (\alpha',\beta',\kappa')$, such that the interband transition energy E_{tr} is given by $E_{tr}(\alpha,\beta,\kappa) = E^C(\alpha,\beta,\kappa) - E^V(\alpha,\beta,\kappa)$, where E^C and E^V are the quantized conduction and valence energies respectively.

II. Transition Strength

The momentum matrix element $p_{CV} = \langle u_C \,|\, p \,|\, u_V \rangle$ determines the interband transition strength. In the case of three dimensional spatial confinement, the momentum matrix element can be written as

$$p_{CV} = \langle u_C \,|\, -i\hbar\nabla \,|\, u_V \rangle = \langle u_C \,|\, -i\hbar\partial_x \,|\, u_V \rangle \hat{x} + \langle u_C \,|\, -i\hbar\partial_y \,|\, u_V \rangle \hat{y} + \langle u_C \,|\, -i\hbar\partial_z \,|\, u_V \rangle \hat{z} \quad (3.2.1)$$

Or alternatively in integral form

$$|p_{CV}|^2 = \hbar^2 O_{CV}^2 \left| \iiint_{\Omega} d^3 r\, u_C^*(r) \nabla u_V(r) \right|^2 \quad (3.2.2)$$

where O_{CV} denotes the spatial overlap integral between the quantized envelope functions of the conduction and valence bands u_C and u_V respectively. Near the Γ point, keeping in mind the adopted transition selection rule, the spatial overlap simplifies to the three-dimensional delta function. Therefore, O_{CV} may be dropped altogether from the expression of the momentum matrix element (3.2.2) knowing it equals unity for the allowed transitions of interest.

Few remarks concerning the evaluation of p_{CV} are highlighted next. In a bulk zinc blend semiconductor, the optical matrix element, M_b, is usually isotropic. Generally speaking, this is not

the case for quantum-well and quantum-dot structures since the optical matrix element depends on the polarization of the electromagnetic field. The momentum matrix element p_{CV} is proportional to the bulk matrix element M_b. The proportionality weight is the anisotropy factor A_{CV} such that

$$\left|p_{CV}\right|^2 = A_{CV} M_b^2 \qquad (3.2.3)$$

To evaluate the anisotropy factor A_{CV}, the (squared) momentum matrix element $\left|p_{CV}\right|^2$ needs to be averaged over degenerate wave vector (or quantized) states depending on the symmetry of the crystal. In the case of lens-shaped dots with circular base, the anisotropy is mostly attributed to the asymmetry along the growth direction. Note that the anisotropy factors are spin-degenerate in that the same anisotropy factor applies to a particular interband transition type with either electromagnetic spin. The momentum matrix elements need to be averaged depending on the crystal symmetry. The averaging procedures vary depending on the dimension of the material. All detailed quantum mechanical calculations are deferred to Appendix B.

II.1 Wetting Layer

The wetting layer can be modeled as a thin quantum well. The anisotropy factors affecting the bulk momentum matrix element near the Γ point are tabulated next:

	C-HH	C-LH	C-SO
TE	1.5	0.5	1
TM	0	2.0	1

Table 3.1: Γ point Quantum Well Anisotropy Factors $A_{CV}^{(WL)}$

II. 2 Lens-Shaped Dot

Likewise for lens-shaped quantum dots, the anisotropy factors affecting the bulk momentum matrix element near the Γ point are tabulated next:

	C-HH	C-LH	C-SO
TE	9/8	7/8	1
TM	6/8	10/8	1

Table 3.2: Γ Point Lens Shaped Quantum Dot Anisotropy Factors $A_{CV}^{(QD)}$

II. 3 Momentum Conservation

The momentum matrix elements satisfy the following momentum conservation rules irrespective of the quantum confinement dimension[6]. The unit vector $\hat{e}$ specifies the polarization direction:

$$\left\langle \left| \hat{x} \cdot M_{C-V} \right|^2 \right\rangle + \left\langle \left| \hat{y} \cdot M_{C-V} \right|^2 \right\rangle + \left\langle \left| \hat{z} \cdot M_{C-V} \right|^2 \right\rangle = 3M_b^2 \qquad (3.2.4)$$

and

$$\left\langle \left| \hat{e} \cdot M_{C-HH} \right|^2 \right\rangle + \left\langle \left| \hat{e} \cdot M_{C-LH} \right|^2 \right\rangle + \left\langle \left| \hat{e} \cdot M_{C-SO} \right|^2 \right\rangle = 3M_b^2 . \qquad (3.2.5)$$

Each interband transition can be regarded as an ingredient for the aggregate material gain. The anisotropy factors prescribe each interband transition partial contribution to the overall gain.

III. Transition Line Broadening

The line profile of light scattered in quantum dots is a superposition of line shapes due to two different kinds of line broadenings. The inhomogeneous and homogeneous broadenings are briefly introduced and their joint effect is mathematically formulated.

III.1 Inhomogeneous Broadening

The inhomogeneous broadening of the quantized energies in an actual quantum dot ensemble is caused by fluctuations in the dot size and material chemical composition. To account for the

[6] To be yet checked for the two dimensional quantum confinement case (i.e. Quantum wire)

effect of these fluctuations, it is assumed that the broadening inhomogeneity has a Gaussian spectral profile $B_g(\nu - \nu_{CV})$ such that

$$B_g(\nu-\nu_{CV}) = \frac{1}{\sqrt{2\pi}\zeta_0}\exp\left[-\frac{(\nu-\nu_{CV})^2}{2\zeta_0^{\,2}}\right] \qquad (3.3.1)$$

where $\Gamma_0 = 2.35\hbar\zeta_0$ represents the full width at half maximum (FWHM) of the inhomogeneous broadening distribution and $\nu - \nu_{CV}$ the frequency dephasing from the average resonance ν_{CV}.

III.2 Homogeneous Broadening

The homogeneous broadening of the gain in a single quantum dot is attributed to the scattering process to exchange electrons (holes) between the ground state and excited states. It increases with temperature. At low temperature (i.e. ~ 77°K) it displays a δ-like spectral profile (i.e. $\lim_{\Gamma_{CV}\to 0} B_l(\nu-\nu_{CV}) = \delta(\nu-\nu_{CV})$). At room temperature (i.e. ~ 300°K), it becomes comparable to the inhomogeneous broadening in magnitude and exhibits a Lorentzian spectral profile $B_l(\nu - \nu_{CV})$ such that

$$B_l(\nu-\nu_{CV}) = \frac{\Gamma_{CV}/\pi}{(\nu-\nu_{CV})^2 + \Gamma_{CV}^2} \qquad (3.3.2)$$

where the FWHM of the homogeneous broadening distribution is $2\hbar\Gamma_{CV}$ with scattering rate Γ_{CV}. The mechanism of carrier relaxation in quantum dots is yet a challenging research area. The transverse relaxation rate is commonly reported to vary in the range 1-10 Ts^{-1} [65]. Pending reliable scattering values, the gain simulations assume a constant transverse relaxation rate for all transitions, such that $\hbar\Gamma_{CV} = E_{ho}$ where E_{ho} denotes the homogeneous broadening in energy units. Quantum dot technology reports a common homogeneous broadening of 16-19 meV [64,65]. The third-order non-linear homogeneous broadening is given by

$$B_l^{(3)}(\nu-\nu_{CV})=\frac{2\Gamma_{CV}^3/\pi}{\left((\nu-\nu_{CV})^2+\Gamma_{CV}^2\right)^2}. \qquad (3.3.3)$$

III.3 Joint Broadening

To determine the line shape of the interband transitions, the inhomogeneous and homogeneous broadenings must be taken into account jointly. The resulting line shape spectral profile is given by the convolution of the Lorentzian and Gaussian profiles in the frequency domain such that:

$$B = B_g \otimes B_l \qquad (3.3.4)$$

IV. Fermi Level Energies

For simplicity, it is assumed that under bias conditions all carriers are directly injected into the uppermost layer of the active region as shown in figure 3.1. It is also assumed that all carriers diffuse into the separate confinement heterostructure (SCH) layer (3D), relax into the wetting layer (2D) and into the dots (0D) where charge neutrality always holds. Nonetheless, the fact that carriers can relax into the wetting layer surrounding the dots from underneath is not envisaged in the gain calculations. Recall that the zero dimensional gain emanating from the dots is the main highlight of the current work. The gain calculations exclude therefore any possible transition into the states confined in the two dimensional wetting layer.

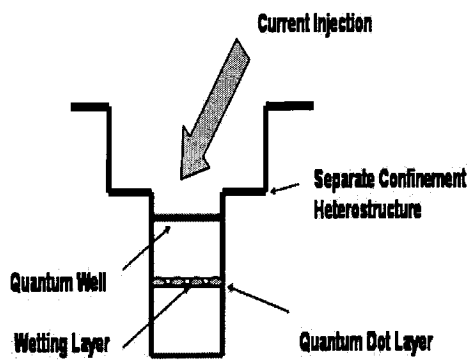

Figure 3.1: Active Region Physical Layers Breakdown

Let n and p be the electron and hole densities, respectively, present in the wetting layer of thickness t_{WL}, such that [53]:

$$n = \frac{m_e^* kT}{\pi\hbar^2 t_{WL}} \ln\left(1 + e^{\frac{\mu_C - E^C}{kT}}\right) \tag{3.4.1}$$

$$p = \frac{kT}{\pi\hbar^2 t_{WL}} \left\{ m_{hh}^* \ln\left(1 + e^{\frac{\mu_V - E^{HH}}{kT}}\right) + m_{lh}^* \ln\left(1 + e^{\frac{\mu_V - E^{LH}}{kT}}\right) \right\} \tag{3.4.2}$$

The Fermi levels μ_C and μ_V are numerically solved for by an adapted *Newton* numerical method. Linearization of equations (3.4.1-2) yields initial guess solutions for the Fermi level energies, $\mu_C^{(0)}$ *and* $\mu_V^{(0)}$ which are then iteratively brought closer to their respective exact values within a preset tolerance. Alternatively, the Fermi levels μ_C and μ_V may be approximated analytically using the *Joyce-Dixon* approximation [53] in terms of the *effective* density of states $N_{band} = 2\left(\frac{m_{band}^* k_B T}{2\pi\hbar^2}\right)^{\frac{3}{2}}$ such that:

$$\mu_C(n) = E_C + k_B T \left(\ln\left(\frac{n}{N_C}\right) + \frac{1}{\sqrt{8}} \frac{n}{N_C} \right) \tag{3.4.3}$$

$$\mu_V(p) = E_V - k_B T \left(\ln\left(\frac{p}{N_V}\right) + \frac{1}{\sqrt{8}} \frac{p}{N_V} \right) \tag{3.4.4}$$

The Fermi level dependence on the injection level embodies that of the gain on the bias current or carrier density. Typically, this dependence reflects the density of states characterizing the quantum confinement dimension of the material. Here, the Fermi levels correspond to the two dimensional wetting layer meanwhile the interband transitions included in the zero dimensional gain calculations are between discrete conduction and valence states of the dots. It is hoped that

this inconsistency can be partially justified by the fact that the carriers in the dots do somewhat permeate the wetting layer as depicted earlier in figure 2.9 (Refer to chapter two). The intrinsic material response observes noticeable changes from the wetting layer to the quantum dots given the material dimension change. Figure 3.2 depicts the anticipated behavior for the conduction and valence Fermi levels in the wetting layer for a carrier density range of 10^{23}-7×10^{24} m^{-3}. The Fermi levels observe an increase, materialized by a reduction of the energy offset between the band edges and Fermi level energies which clearly reflect the *effective* density of states profile. Moreover, figure 3.2 shows that the (WL) conduction Fermi level penetrates the conduction discrete levels starting at a carrier density threshold of 6×10^{24} m^{-3}.

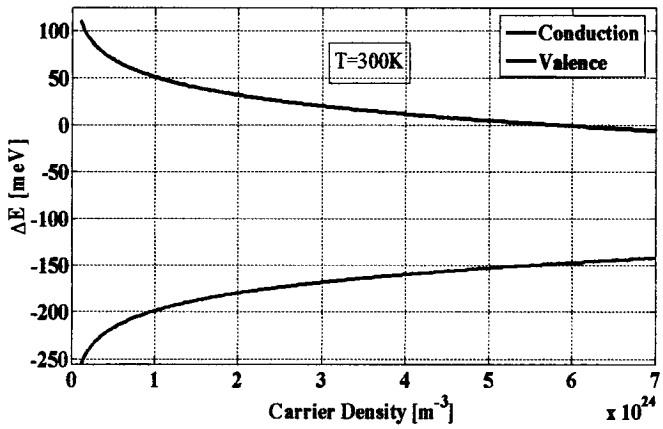

Figure 3.2: Energy Offset between Band Edges and Fermi Levels

In a two-level discrete energy medium, the transition energy between conduction level A and valence level B is given by $E_{tr} = E_A^C - E_B^V$.

Near resonance such that $\nu \approx \nu_{CV}$, the photon energies at levels A and B are given by

$$E_A(\nu) = (h\nu - E_{tr})\frac{m_V^r}{m_e^*} + E^C \qquad (3.4.5)$$

$$E_B(\nu) = -(h\nu - E_{tr})\frac{m_V^r}{m_V^*} + E^V \qquad (3.4.6)$$

where m_V^r is the reduced mass given by $\frac{1}{m_V^r} = \frac{1}{m_e^*} + \frac{1}{m_V^*}$.

Once the energy levels E_A and E_B are calculated, recourse is made to Fermi-Dirac distributions $f_C(E_A(\nu))$ and $f_V(E_B(\nu))$ to determine their population probabilities at temperature T such that:

$$f_C(E_A(\nu)) = \left[1 + \exp\left\{\frac{\left(h\nu - E_A(\nu)\right)\frac{m_V^r}{m_e^*} - \mu_C}{k_B T}\right\}\right]^{-1} \qquad (3.4.7)$$

$$f_V(E_B(\nu)) = \left[1 + \exp\left\{\frac{\left(h\nu - E_B(\nu)\right)\frac{m_V^r}{m_e^*} - \mu_V}{k_B T}\right\}\right]^{-1} \qquad (3.4.8)$$

where K_B is the *Boltzman* constant, T the lattice temperature, m_e^* and m_V^* are the effective masses of the electron and (heavy or light) holes respectively. Due to the large spin-orbit splitting, for most purposes, only the heavy and light hole bands play a prominent role in electronic or optoelectronic properties.

V. Material Susceptibility

Recall from basic electromagnetics that for a two-level energy medium, the induced polarization *P(r,t)* of the isotropic material in the presence of an electric field *E(r,t)* can be expanded up to a third-order perturbation such that

$$P(r,t) = \varepsilon_0 \chi^{(1)} E(r,t) + \varepsilon_0 \chi^{(3)} E(r,t) E(r,t) E(r,t) \qquad (3.5.1)$$

where ε_0 is the vacuum permittivity, $\chi^{(1)}$ and $\chi^{(3)}$ are the linear and third-order non-linear susceptibilities of the material, respectively. The above polarization expression is deliberately missing a second-order term since it is known from density matrix theory that even order polarization is erased in two-level media.

The susceptibilities describe the material response to the interaction between matter (i.e. electron) and light (i.e. photon), such that the linear susceptibility $\chi^{(1)}$ at photon frequency v is given by [65],

$$\chi^{(1)}(v-v_{CV})=\frac{e^2}{\pi\varepsilon_0 m_0^2 vV}\sum_C\sum_V\frac{\left|P_{CV}^{\hat{e}}\right|^2(f_C-f_V)}{E_{tr}^{CV}}\left[\frac{1}{(v-v_{CV})+i\Gamma_{CV}}+\frac{1}{(v+v_{CV})+i\Gamma_{CV}}\right] \quad (3.5.2)$$

The third-order non-linear susceptibility $\chi^{(3)}$ at pump beam frequency v_1 and probe beam frequency v_2 is given by [65]

$$\chi^{(3)}(2v_2-v_1;v_2,v_2,-v_1)=$$
$$\frac{2e^4}{3\varepsilon_0 h^3 m_0^4 v_1 v_2^2}\sum_{C,V}\frac{|P_{CV}|^4(f_c-f_v)}{v_{CV}(2v_2-v_1-v_{CV}+i\Gamma_{CV})}\left[\frac{1}{v_2-v_1+i\Gamma_{\parallel}^{V}}+\frac{1}{v_2-v_1+i\Gamma_{\parallel}^{C}}\right]\left[\frac{1}{v_2-v_{CV}+i\Gamma_{CV}}-\frac{1}{v_2-v_{CV}-i\Gamma_{CV}}\right] \quad (3.5.3)$$

V.1 Linear Material Gain

Discarding the non resonant term of the linear susceptibility and incorporating the joint broadening effect yields an expression for the linear material gain $g^{(1)}(v)$, near resonance (i.e. $v\approx v_{CV}$) such that

$$g^{(1)}(v)=-\frac{v}{cn_r}\mathrm{Im}(\chi^{(1)}(v))=\frac{\pi e^2 E_p}{3cn_r\varepsilon_0 m_0}\sum_C\sum_V\frac{A_{CV}^{\hat{e}}(f_C-f_V)}{E_{tr}^{CV}}(B_l\otimes B_g)(v-v_{CV}) \quad (3.5.4)$$

where n_r is the background refractive index of the dot material.

V.2 Non-Linear Material Gain

The nonlinear susceptibility in the degenerate case can be expressed as follows [65],

$$\chi^{(3)}(v)=-\frac{2\pi e^4}{27\varepsilon_0 m_0^2 h^2 v^3}\sum_C\sum_V\frac{A_{CV}^{\hat{e}2}(f_C-f_V)}{E_{tr}^{CV}}\frac{\Gamma_{CV}}{\Gamma_{\parallel}}\frac{(v-v_{CV}-i\Gamma_{CV})}{\left[(v-v_{CV})^2+\Gamma_{CV}^2\right]^2} \quad (3.5.5)$$

The non linear material gain $g^{(3)}(\nu)$ is given by

$$g^{(3)}(\nu) = -\frac{3\nu}{2\varepsilon_0 c^2 n_r^2}\mathrm{Im}(\chi^{(3)}(\nu))I_p(\nu) \tag{3.5.6}$$

where $I_p(\nu)$ is the power density of the electromagnetic field given by

$$I_p(\nu) = \frac{cn_r\varepsilon_0}{2}|E(\nu)|^2. \tag{3.5.7}$$

The time constant for non linear gain is $\Gamma_{\parallel}^{-1} = \left(\Gamma_{\parallel}^{C}\right)^{-1} + \left(\Gamma_{\parallel}^{V}\right)^{-1} = \tau_p$, which corresponds to the inverse of the photon lifetime in the cavity [65].

Including the expression of the momentum matrix element in terms of the anisotropy factor, the non linear material gain for a single quantum-dot becomes

$$g^{(3)}(\nu) = -\frac{\pi^2 e^4 E_p^2 I_p(\nu)}{2(3h\nu cn_r\varepsilon_0 m_0)^2}\sum_C\sum_V \frac{A_{CV}^{\hat{e}2}(f_C - f_V)}{E_{tr}^{CV}}\frac{(B_l^{(3)} \otimes B_g)(\nu - \nu_{CV})}{\Gamma_{\parallel}\Gamma_{CV}} \tag{3.5.8}$$

V.3 Gain Simulations

The calculation of the material gain can now proceed for an ensemble of quantum dots. The material gain is the sum of individual contributions from all dots within the homogeneous broadening at a certain frequency. The material gain for an ensemble of quantum dots is given by

$$g(\nu) = N_D(g^{(1)}(\nu) + g^{(3)}(\nu)), \tag{3.5.9}$$

where the volume density N_D is the inverse of the average dot volume $N_D = \overline{V}^{-1}$.

The non linear gain $g^{(3)}(\nu)$ is intensity dependent and has opposite sign to the linear gain $g^{(1)}(\nu)$. Consequently, the higher the power in the cavity the smaller the gain. In the actual gain simulation, a unit input static electromagnetic field is assumed (i.e. $|E(\nu)| = 1\,\mathrm{V^2m^{-2}}$). The inhomogeneous broadening FWHM is 40 meV. The lattice temperature is 300K. The active region consists of a single layer of $12.5\times12.5\times2.5\,\mathrm{nm}^3$ *InAs* lens-shaped dots deposited onto a

0.5 nm thick wetting layer. One quantum dot confined excited state is included in the gain calculations.

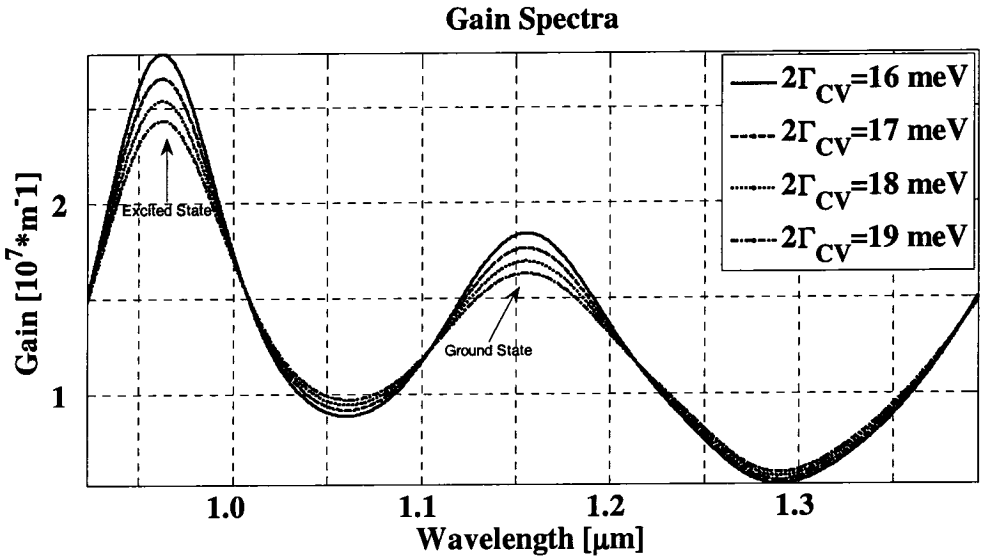

Figure 3.3: Material Gain Spectra

V.4 Differential Gain

At a specified carrier density (or current injection) level, the peak gain is numerically given by the maximum of the material gain spectral distribution. The peak gain spectral distribution, as shown in figure 3.4 below, shows an abrupt shoot up for low injection prior to it stabilizing in the carrier density range of 2×10^{23} - 5×10^{23} m^{-3}.

The peak gain carrier density dependence exhibits some flattening indicative of gain saturation. The high peak gain of 10^7 m^{-1} for a single layer of quantum dots is in line with that predicted by *Bimberg et.al.* [15]. The differential gain can be defined as the rate of change of the peak gain with respect to the injected carrier density. It is clear from figure 3.4 that the differential gain is very high (i.e. the peak gain rate of change is very steep) before the onset of gain saturation.

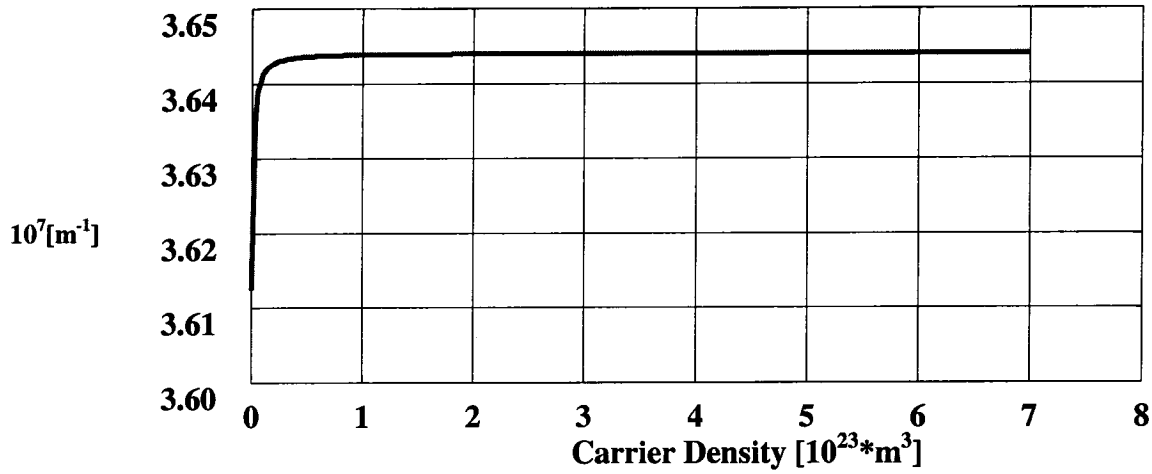

Figure 3.4 : Material Gain Peak vs. Carrier Density

V.5 Linewidth Enhancement Factor

The refractive index is of interest here. The change in the refractive index can be described by a symmetric detuned oscillator around the interband resonance frequency as shown in figure 3.5. At resonance, the refractive index corresponds to the background refractive index of the material n_r. An experimental measurement of $n_r(InAs)$ at 300K gives 3.51 [32]. The change in the refractive index can be deduced from the real part of the linear susceptibility such that:

$$n(\nu) = n_r + \frac{1}{2n_r}\mathrm{Re}(\chi^{(1)}(\nu)) = n_r + \sum_c \sum_v \frac{e^2 E_p N_D}{12 n_r \varepsilon_0 m_0} \frac{A_{CV}^{\dot{e}} (f_C - f_V)}{\Gamma_{CV} E_{tr}^{CV}} \left(1 - \frac{\nu_{CV}}{\nu}\right) B_g(\nu - \nu_{CV}) \quad (3.5.10)$$

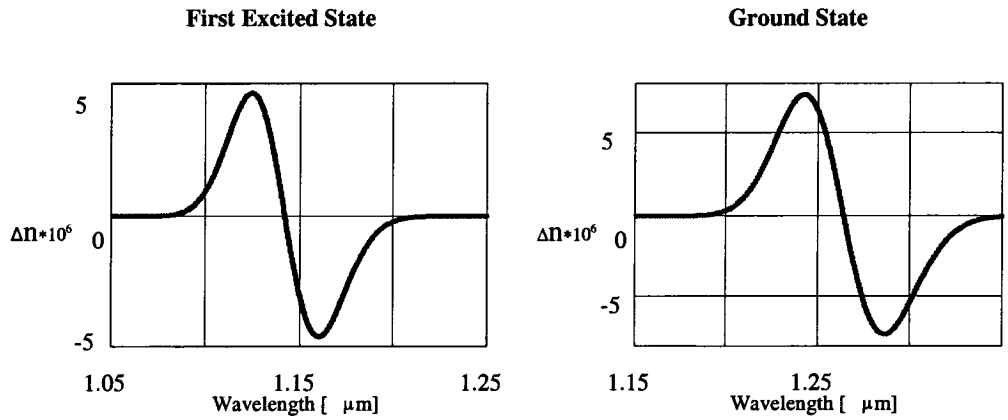

Figure 3.5: Refractive Index Change vs. Wavelength

By virtue of the phenomenon observed in figure 3.4, it is expected that a small change in carrier density would hardly inflict any significant shift on the resonant wavelength. It can be deduced that an almost zero refractive index change can be achieved for a negligible change in carrier density. Given that the carrier density dependent refractive index change is tied to the change in the optical gain through the *Kramers-Kronig* relation namely,

$$\alpha_e = -\frac{4\pi}{\lambda}\frac{\partial n/\partial N}{\partial g/\partial N} \qquad (3.5.11)$$

quantum dots are well poised to have a very small linewidth enhancement factor α_e. λ is the free-space photon wavelength. The computed linewidth enhancement factors corresponding to the ground and first excited transition resonances are approximately, 0.001 and 0.17 , respectively for a carrier density of 5×10^{23} m^{-3}.

In figure 3.5, the red and green arrows point to the resonance wavelengths corresponding to the ground and first excited states respectively. The blue arrow points to the average resonance wavelength. The linewidth enhancement factor reaches an almost zero absolute minimum at the resonance wavelengths.

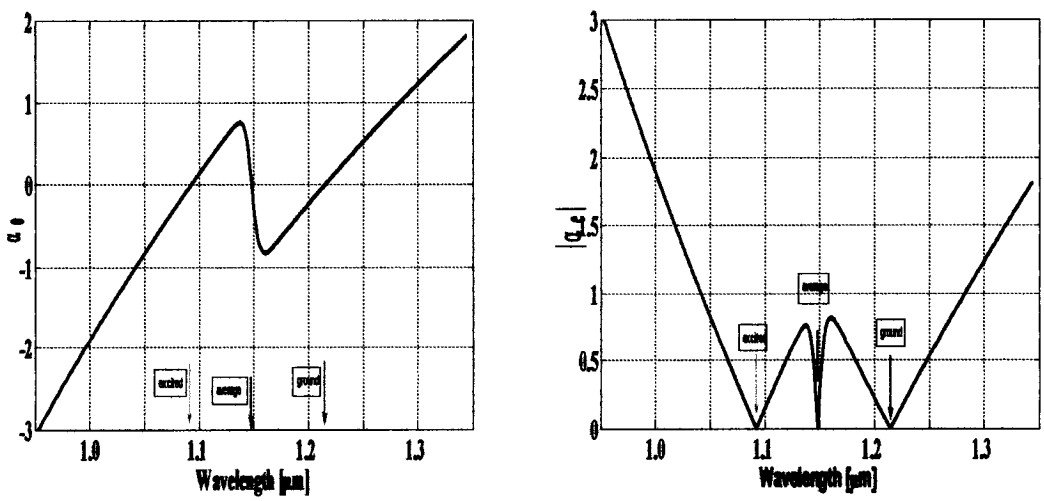

Figure 3.6: Linewidth Enhancement Factor Dispersion

a. $\alpha_e(\lambda)$ b. $|\alpha_e(\lambda)|$

Ideally, the material gain spectrum would have a perfect Gaussian profile for a quantum dot ensemble with a single confined electron and hole energy levels. The material gain peak occurs then at the single resonant wavelength and the quantum dot laser may operate chirp-free. However, a more realistic gain spectrum includes contributions from other excited transitions as discussed before. Asymmetries in the gain spectrum are therefore expected, which in turn, increase the linewidth enhancement factor magnitude $|\alpha_e|$ for some detuning around the resonance wavelengths as shown in figure 3.6.b. Note also that the detuning bandwidth around the average resonance for which $|\alpha_e|$ is practically small shrinks further at saturating injection levels , 2×10^{24} m^{-3} and higher (refer to figure 3.4). In fact such detuning bandwidth could reduce altogether to a spectral streak, as depicted in figure 3.7, at carrier densities allowing penetration of the Fermi-level into the conduction band, 6×10^{24} m^{-3} and higher (refer to figure 3.2).

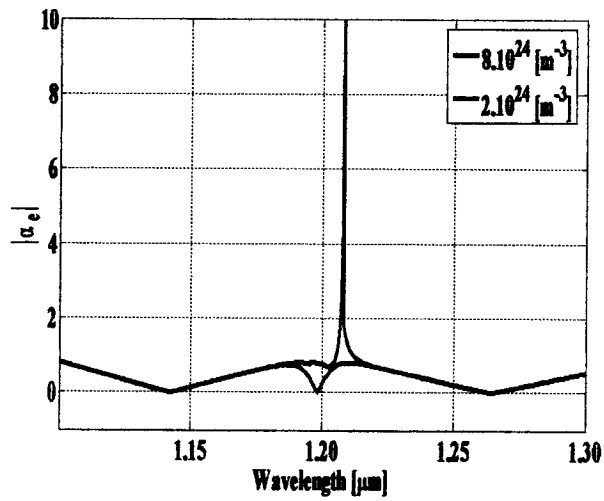

Figure 3.7: $|\alpha_e(\lambda)|$ at Saturating Carrier Density Levels

VI. Conclusion

Successful quantum dot material gain calculations have been carried out under the assumption of

a resonant two energy-level system. The gain calculations depend critically on the interband transition energies obtained from the electronic structure of the quantum dot material. It should be emphasized that an in-depth understanding of the scattering processes (electron-hole and carrier-phonon) would be useful in modeling the material gain. To remain within the scope of this thesis, the cavity structure optimization and modal analysis of the waveguide can proceed in confidence at this time.

Chapter Four

Waveguide Modal Analysis

The design of polarization-insensitive semiconductor waveguides requires thorough modal analysis of the optical field confined to the embedded waveguide layers and optimization of the waveguide structure geometry. The approach considered herein to immunize a nonplanar waveguide against the state of polarization revolves around tailoring the aspect ratio of the active core of the structure while preserving the inherent quantum dot material anisotropic nature. The ensuing flexibility in the fabrication of polarization-insensitive waveguides is highlighted briefly.

I. Introduction

Several reported processes for the design of polarization-insensitive waveguides are based on the use of tensile-strained-barrier-well multiple quantum-well (MQW) structures. Such processes aim to achieve an anisotropic gain medium able to compensate for the difference in the polarization-dependent confinement factors. Devices based on these processes are complicated to design and fabricate because they imply the introduction of well-controlled anisotropy into the gain medium. This approach is quite involved as it alters the active medium optical properties such as material gain, refractive index and optical confinement.

The alternative approach with greater flexibility in equalizing the polarization-dependent *modal gain* factors, and not the *material gain* factors, resides in optimizing the nonplanar waveguide aspect ratio in order to make up for the *non-altered* anisotropy of the gain medium. With current micro-fabrication technology, the waveguide geometry can be controlled to a high accuracy and many waveguide shapes can be fabricated.

The analysis of some potential waveguide structures may require sophisticated mathematical

formulations. For simplicity, the selected waveguide structure has a rectangular active core fully buried in a surrounding $Al_xGa_{1-x}As$ cladding layer. The composite active core consists of a single or multi-fold vertical stack of self-assembled lens-shaped *InAs/GaAs* quantum dot layers sandwiched between two separate confinement heterostructure (SCH) layers. Each single quantum dot layer measures 3.5 nm along the growth direction corresponding to the aggregate thickness of the granular layers namely, 0.5 nm-thick *InAs* wetting layer, 2.5 nm-thick *InAs* island and 0.5 nm-thick *GaAs* spacing barrier. The *GaAs* SCH layers are 15 nm-thick each. The critical dimension being the active core thickness is therefore *a priori* known and fixed throughout the calculations. The free dimension being the width of the active core remains yet to be determined. The associated mathematical problem ultimately reduces to nonlinear optimization of the core width subject to the constraint of polarization-insensitive modal gain.

II. Refractive Index

A transverse view of the active core shown in figure 4.1 depicts its constitutive embedded layers.

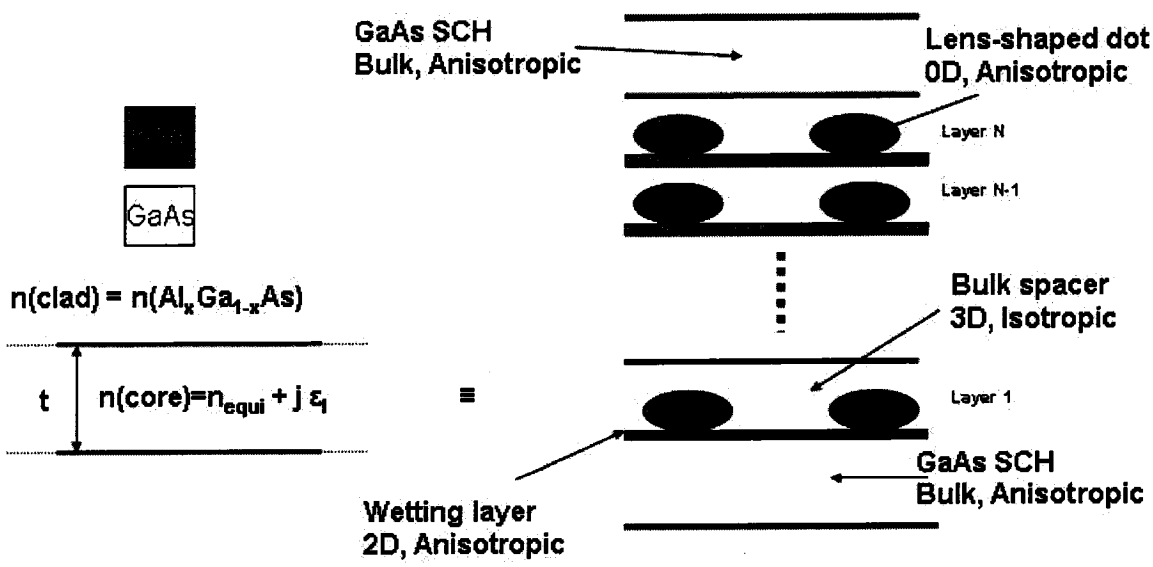

Figure 4.1: Schematic View of the Embedded Active Layers

The *InAs* islands are surrounded by a higher band gap material, *GaAs,* barrier to effectively

confine the injected carriers. The active core with refractive index *n(core)* is sandwiched between upper and lower $Al_xGa_{1-x}As$ cladding layers with a smaller refractive index *n(clad)* resulting in optical waveguiding. Given the inhomogeneous nature of the active core, the refractive index distribution is expected to be spatially varying as depicted in figure 4.2.

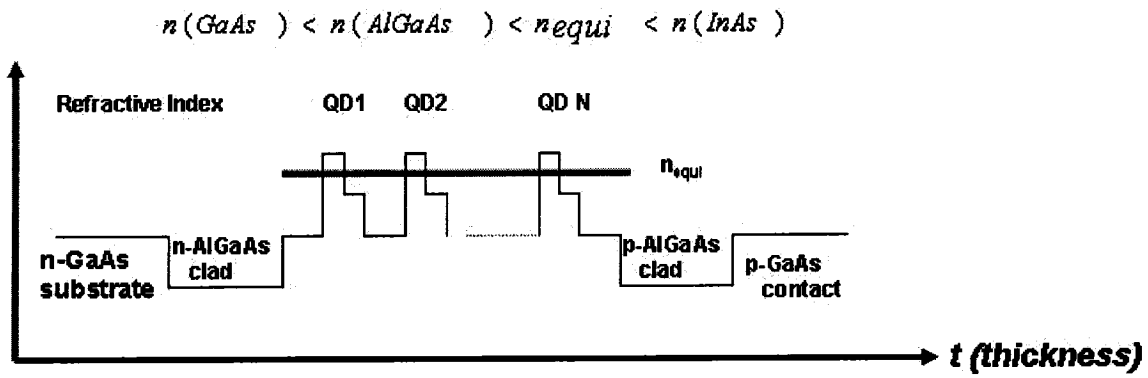

Figure 4:2 Refractive Index Spatial Profile

To simplify the mathematical formulations, a non-spatially varying refractive index in the active core is sought. An elementary mathematical formula based on the *InAs xz*-plane aerial coverage per quantum dot layer ξ_{xz}[7] and individual thicknesses of the constitutive sub-layers yields a static refractive index n_{equi} associated with an equivalent homogeneous isotropic core such that:

$$n_{equi} = \frac{(t_{WL} + \xi_{xz}\, t_{QD} N_{QD}) n_{InAs} + (t_{BB} + (1-\xi_{xz}) t_{QD} N_{QD} + 2t_{SCH}) n_{GaAs}}{t_{WL} + N_{QD}\, t_{QD} + t_{BB} + 2t_{SCH}} \qquad (4.2.1)$$

where N_{QD} is the repetition number of the quantum dot layers. Note that an expression for ξ_{xz} can be easily obtained by projecting the dot surface equation (2.1.2) onto the *xz*-plane (i.e. $y=0$) and solving for the *InAs* area integral such that $\xi_{xz} = t_{QD} \int_{-R}^{+R} \sqrt{1 - \frac{x^2}{R^2}}\, dx \approx 70\%$.

[7] Refer to the right-hand-side plot in figure 2.3

An increase in the repetition number results in a depreciation of the equivalent refractive index leading to even weaker guiding. Throughout this work, the high-frequency refractive indices of *InAs* and *GaAs* at a temperature of 300 °K are used and are 3.51 and 3.3 respectively [32] whereas that of the cladding layer is given by:

$$n(Al_xGa_{1-x}As) = \sqrt{10.89 - 2.73 \times x} \qquad (4.2.2)$$

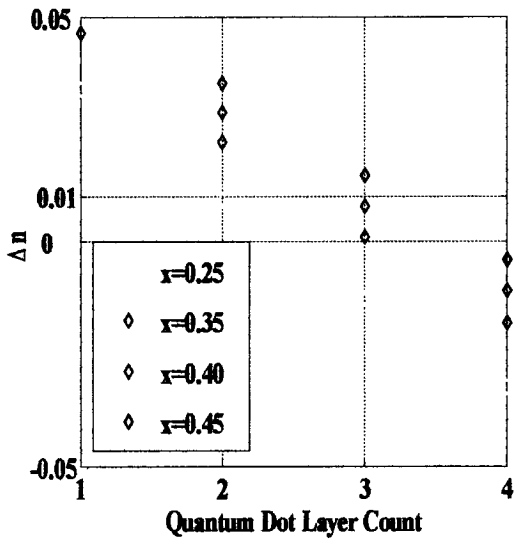

Figure 4.3: Core-Clad Refractive Index Contrast

The repetition number N_{QD} and *Al* molar fraction x can be varied so that the core-clad refractive index contrast Δn ensures (weak) guiding of the structure such that:

$$0 < \Delta n = \frac{n_{equi}^2 - n_{Al_xGa_{1-x}As}^2}{n_{equi}^2} \leq 0.01 \qquad (4.2.3)$$

For example, three quantum dot layers can be supported by a weakly guiding structure for an *Al* molar fraction range of $0.35 \leq x \leq 0.40$ as shown in figure 4.3. Likewise, a two-quantum dot layer weakly guiding structure can be supported at an *Al* molar fraction of 0.25.

III. Waveguide Modal Analysis

A symmetric rectangular core waveguide with known thickness $2t$ and unknown width $2w$ is considered. $n_1=n_{equi}$ and $n_0=n(Al_xGa_{1-x}As)$ are the refractive indices of the active core and the surrounding cladding layers respectively with $n_1>n_0$. The active core semiconductor magnetic permeability equals that *in vacuum* such that $\mu = \mu_0$. Unlike their passive counterparts, active waveguides require complex-valued material parameters to include effects of gain and loss. For example, the active core complex relative permittivity can be written $\varepsilon = \varepsilon_r + j\varepsilon_i$ where the real part ε_r accounts for dispersion and the imaginary part ε_i is responsible for gain or absorption. Typically the refractive index imaginary part is much smaller than its real part $\sqrt{\varepsilon_i} << \sqrt{\varepsilon_r}$ so it can be considered as a perturbation. Under this circumstance, it can be reasonably assumed that the transverse field distribution in an active waveguide (i.e. $\varepsilon_i \neq 0$) is very similar to that in its passive waveguide analog (i.e. $\varepsilon_i = 0$). Thus the modal gain in the passive configuration can be used to predict that in the active analog. Such indirect method to estimate the modal gain uses the real-valued passive waveguide parameters and must be distinguished from other direct methods analyzing the active waveguide with its complex-valued parameters.

III.1 Rectangular Waveguides: 2D Problem

The rectangular core waveguide is assumed to have a uniform transverse cross-section regardless of the position along the axis of propagation which is parallel to the structure symmetry axis z[8] as shown in figure 4.4. The goal then is to determine both the propagation constant $\beta = \beta_r + j\beta_i$ ($\beta^2 = \beta_R^2 + j\beta_I^2$ where $\beta_R^2 = \beta_r^2 - \beta_i^2$ and $\beta_I^2 = 2\beta_r\beta_i$) and the electromagnetic field distribution in the transverse xy-plane associated with a guided mode propagating along the

[8] z denotes the longitudinal axis of propagation whereas y denotes the growth direction

positive longitudinal z-direction in the following form:

$$\begin{cases} E = E_t(x,y)\, e^{j(\omega t - \beta z)} \\ \\ H = H_t(x,y)\, e^{j(\omega t - \beta z)} \end{cases} \tag{4.3.1}$$

The subscript t in equation (4.3.1) refers to a vector lying in the xy-transverse plane such that

$$E_t(x,y) = E_x(x,y)\hat{x} + E_y(x,y)\hat{y}\,.$$

Such field distributions satisfy *Maxwell* equations in the equivalent homogeneous core, nonmagnetic (i.e. $\mu = \mu_0$) and lossless dielectric medium (passive waveguide analog) given by:

$$\begin{cases} \nabla \times E = -\mu_0 \dfrac{\partial H}{\partial t} \\ \\ \nabla \times H = \varepsilon_0 n^2 \dfrac{\partial E}{\partial t} \end{cases} \tag{4.3.2}$$

The electromagnetic fields and their corresponding phasors in equation (4.3.2) are referred to as the same entities for the sake of light notation (i.e. time dependence *exp(jωt)* is dropped).

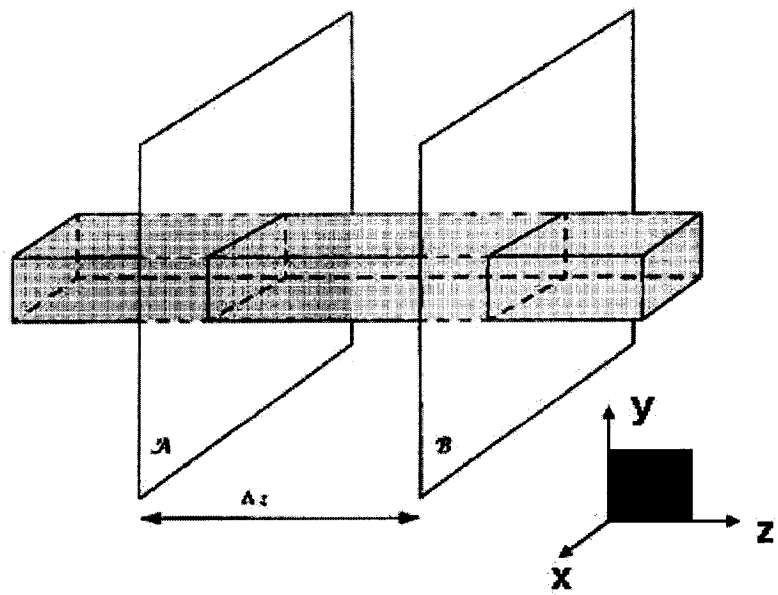

Figure 4.4: Rectangular Waveguide with a Uniform Transverse Cross-Section

Two hybrid mode classes are supported by the rectangular waveguide structure such that the field components E_x and H_y are predominant in the E_{pq}^x mode (i.e. Quasi-TE), whereas the components E_y and H_x are predominant in the E_{pq}^y mode (i.e. Quasi-TM). The positive integers *p-1* and *q-1* indicate the number of field zeros in the *x* and *y*-directions respectively.

III.1.1 Quasi-TE Wave Equation

The E_{pq}^x mode wave equation is obtained by setting $H_x = 0$ in equations (4.3.2) such that

$$\nabla_t^2 H_y + (k^2 n^2 - \beta^2) H_y = 0 \qquad (4.3.3)$$

where the scalar operator $\nabla_t^2 \equiv \frac{\partial^2}{\partial x^2} + \frac{\partial^2}{\partial y^2}$ is the transverse *Laplacian* operator.

III.1.2 Quasi-TM Wave Equation

The E_{pq}^y mode wave equation is obtained by setting $H_y = 0$ in equations (4.3.2) such that

$$\nabla_t^2 H_x + (k^2 n^2 - \beta^2) H_x = 0 \qquad (4.3.4)$$

III.2 Marcatili Method

Marcatili method [43] is used to simplify the analysis of the hybrid modes in the rectangular core waveguide. The two important assumptions ***A1*** and ***A2*** of this method read

A1 The electromagnetic field of the guided mode decays quite rapidly in the cladding region;

A2 The transverse E_{pq}^x and E_{pq}^y mode electromagnetic fields are separable such that

$$\begin{cases} E_x(x,y) \cong \psi_{TM}(x)\psi_{TE}(y) \\ \\ E_y(x,y) \cong \psi_{TE}(x)\psi_{TM}(y) \end{cases} \qquad (4.3.5).$$

In the present study, only the fundamental modes E_{11}^x and E_{11}^y are considered. For the E_{11}^x [E_{11}^y] mode, $\psi_{TM}(x)$ [$\psi_{TE}(x)$] is the TM_0 [TE_0] field in the horizontal slab waveguide formed by extending the thickness of the rectangular core to infinity. Similarly, for the E_{11}^x [E_{11}^y] mode, $\psi_{TE}(y)$ [$\psi_{TM}(y)$] is the TE_0 [TM_0] field in the vertical slab waveguide formed by extending the width of the rectangular core to infinity as shown in figure 4.5.

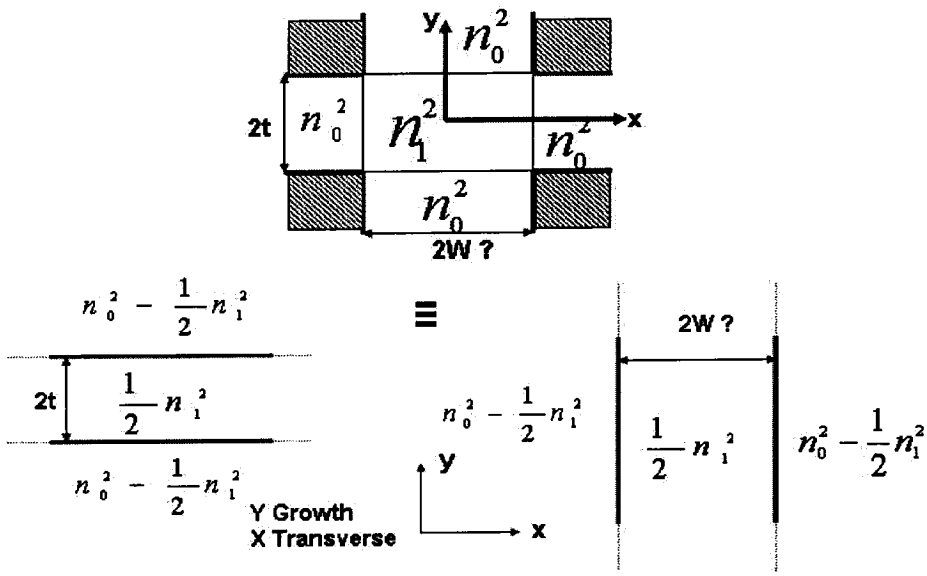

Figure 4.5: Rectangular Waveguide and Its Equivalent Independent Slab Waveguides

The refractive index distribution of the rectangular waveguide can be expressed in terms of its transverse components as:

$$n^2(x,y) = N_x^2(x) + N_y^2(y) \qquad (4.3.6)$$

such that in each slab waveguide, the corresponding refractive index distribution is given by:

$$N_x^2(x)=\begin{cases}\dfrac{n_1^2}{2} & |x|\le w\\[2ex] n_0^2-\dfrac{n_1^2}{2} & |x|>w\end{cases} \qquad N_y^2(y)=\begin{cases}\dfrac{n_1^2}{2} & |y|\le t\\[2ex] n_0^2-\dfrac{n_1^2}{2} & |y|>t\end{cases}$$

(4.3.7) (4.3.8)

III.3 Slab Waveguides: 1D Problem

The analysis can be carried further for each of the slab waveguides shown in figure 4.5. For brevity only the case of the vertical slab waveguide (i.e. $n=n(y)$) is presented. The analysis of the horizontal slab waveguide can be reproduced in a similar fashion by noting that $\boldsymbol{n=n(x)}$ and the electromagnetic field has no y-dependence in that particular case.

III.3.1 Vertical Slab Waveguide (Growth Direction)

In the vertical slab waveguide the electromagnetic field can either be TE or TM polarized. Substituting equations (4.3.1) into (4.3.2) yields the following coupled sets of equations for the electromagnetic components:

$$\begin{cases}-j\beta E_y-\dfrac{\partial E_z}{\partial y}=-j\omega\mu_0 H_x\\[2ex] \dfrac{\partial E_z}{\partial x}+j\beta E_x=-j\omega\mu_0 H_y\\[2ex] \dfrac{\partial E_x}{\partial y}-\dfrac{\partial E_y}{\partial x}=-j\omega\mu_0 H_z\end{cases} \quad \text{and} \quad \begin{cases}-j\beta H_y-\dfrac{\partial H_z}{\partial y}=j\omega\varepsilon_0 n^2 E_x\\[2ex] \dfrac{\partial H_z}{\partial x}+j\beta H_x=j\omega\varepsilon_0 n^2 E_y\\[2ex] \dfrac{\partial H_x}{\partial y}-\dfrac{\partial H_y}{\partial x}=j\omega\varepsilon_0 n^2 E_z\end{cases}$$

(4.3.9) (4.3.10)

Furthermore, the electromagnetic fields E and H do not have x-axis dependency therefore the two sets of equations (4.3.9-10) become decoupled and yield two independent wave equations.

III.3.2 TE Field Distribution

The electromagnetic field in the TE configuration satisfies the following wave equation:

$$\frac{d^2E_x}{dy^2} + (k^2n^2 - \beta^2)E_x = 0 \qquad (4.3.11)$$

Note that the electric field component E_x in equation (4.3.11) denotes the one-dimensional field $\psi_{TE}(y)$ from equation (4.3.5).

where
$$\begin{cases} H_y = -\dfrac{\beta}{\omega\mu_0}E_x \\ H_z = \dfrac{j}{\omega\mu_0}\dfrac{dE_x}{dy} \\ E_y = E_z = H_x \equiv 0. \end{cases} \qquad (4.3.12)$$

The tangential components E_x and H_z must be continuous at the core-clad interface. Since the electric field lies in the transverse xy-plane perpendicular to the propagation direction z; this electromagnetic field distribution is called the *transverse electric* (TE) mode and is given by

$$E_x = \mathrm{A}^{TE}\cdot\begin{cases} \cos(\kappa_y t - \phi)\cdot e^{-\sigma_y(y-a)} & y > t \\ \cos(\kappa_y y - \phi) & -t \le y \le t \\ \cos(\kappa_y t + \phi)\cdot e^{\sigma_y(y+a)} & y < -t \end{cases} \qquad (4.3.13).$$

where A^{TE} is the amplitude of the field component E_x, κ_y and σ_y are vertical wavenumbers in the core and cladding regions respectively such that:

$$\begin{cases} \kappa_y = \sqrt{k^2\dfrac{n_1^2}{2} - \beta_y^2} \\ \sigma_y = \sqrt{\beta_y^2 - k^2\left(n_0^2 - \dfrac{n_1^2}{2}\right)} \end{cases} \qquad (4.3.14)$$

where β_y is the vertical component of the mode propagation constant. The magnetic field

component H_z and therefore $\frac{dE_x}{dy}$ must be continuous at the core-clad interfaces $y = \pm t$. Applying the boundary conditions, and defining normalized vertical wavenumbers such that:

$$\begin{cases} u_y = \kappa_y kt \\ s_y = \sigma_y kt \end{cases} \qquad (4.3.15)$$

The dispersion equation for the TE_q (q=0,1,...) mode is given by:

$$\begin{cases} u_y = \frac{q\pi}{2} + \tan^{-1}\left(\frac{s_y}{u_y}\right) \\ \phi = \frac{q\pi}{2} \end{cases} \qquad (4.3.16)$$

The vertical wavenumbers are not independent, rather they are related by the following equation $s_y^2 + u_y^2 = v_y^2$ where $v_y = kt\sqrt{n_1^2 - n_0^2}$ is the normalized frequency of the vertical slab waveguide. Once the wavelength of the optical signal and the geometrical parameters of the slab waveguide are specified, in other words when the normalized frequency is determined, the dispersion equation (4.3.16) can be solved and the propagation constant β_y can be evaluated. The transverse wavenumber κ_y should be a real number for the main part of the optical field to be confined in the core region. Then the following condition must be satisfied by the guided mode

$$n_0^2 - \frac{1}{2}n_1^2 \le \left(\frac{\beta_y}{k}\right)^2 \le \frac{1}{2}n_1^2 \qquad (4.3.17)$$

$n_{eff}^y = \frac{\beta_y}{k}$ is the TE_q mode effective index for the plane wave.

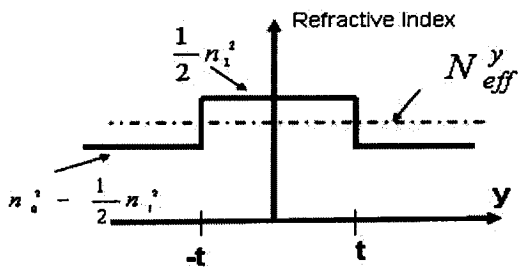

Figure 4:6 Refractive Index Vertical Profile

III.3.3 TM Field Distribution

The electromagnetic field in the TM configuration satisfies the following wave equation:

$$\frac{d}{dy}\left(\frac{1}{n^2}\frac{dH_x}{dy}\right)+\left(k^2-\frac{\beta^2}{n^2}\right)H_x=0 \qquad (4.3.18)$$

where

$$\begin{cases} E_y=\dfrac{\beta}{\omega\varepsilon_0 n^2}H_x \\ E_z=-\dfrac{j}{\omega\varepsilon_0 n^2}\dfrac{dH_x}{dy} \\ E_x=H_y=H_z\equiv 0. \end{cases} \qquad (4.3.19)$$

The magnetic field lies in the transverse *xy*-plane perpendicular to the propagation direction *z*; this electromagnetic field distribution is called the *transverse magnetic* (TM) mode and given by

$$H_x=\mathrm{A}_{TM}\cdot\begin{cases} \cos(\kappa_y t-\varphi)\cdot e^{-\sigma_y(y-a)} & y>t \\ \cos(\kappa_y y-\varphi) & -t\le y\le t \\ \cos(\kappa_y t+\varphi)\cdot e^{\sigma_y(y+a)} & y<-t \end{cases} \qquad (4.3.20)$$

Defining appropriate (normalized) wavenumbers and applying the boundary conditions in a similar fashion as for the TE mode, the following dispersion equation for the TM_q mode (q=0,1,...) is obtained:

$$\begin{cases} u_y=\dfrac{q\pi}{2}+\tan^{-1}\left(\left(\dfrac{n_1^2}{2n_0^2-n_1^2}\right)\dfrac{s_y}{u_y}\right) \\ \varphi=\dfrac{q\pi}{2} \end{cases} \qquad (4.3.21)$$

Again, once the TM_q modal dispersion equation (4.3.21) is solved, the propagation constant β_y and the associated effective index n_{eff}^{y} can be evaluated.

III.3.4 Horizontal Slab Waveguide (Width Direction)

As mentioned earlier, the lateral slab waveguide is analyzed in a similar fashion by using

appropriate (normalized) parameters and solving the corresponding modal dispersion equations for both TE and TM configurations. The outcome of the analysis yields the other component β_x (n_x^{eff}) of the propagation constant (effective index) such that:

$$\begin{cases} \beta^2 = \beta_x^2 + \beta_y^2 \\ \left(n^{eff}\right)^2 = \left(n_x^{eff}\right)^2 + \left(n_y^{eff}\right)^2 \end{cases} \tag{4.3.22}$$

III.4 Optical Confinement Factors

It is assumed that the entire core is the only active region in the waveguide. Consequently, only the portion of the mode field confined to the active core is of particular interest. It is worthwhile noting that the actual confinement to the dots is much less than to the active core because of low aerial coverage of the *InAs* islands in the active layer. Two-dimensional confinement of the optical power occurs along both the x and y-directions and can be expressed as the product of the confinement to each of the slab waveguides shown in figure 4.5. The one-dimensional modal confinement factors Γ_r^{TE} and Γ_r^{TM}, $r = x$ or y, are given by:

$$\begin{cases} \Gamma_x^{TE} = \dfrac{\int_{-w}^{+w} |E_y|^2 dx}{\int_{-\infty}^{\infty} |E_y|^2 dx} \equiv \dfrac{\int_{-w}^{+w} |\psi_{TM}(x)|^2 dx}{\int_{-\infty}^{\infty} |\psi_{TM}(x)|^2 dx} \\ \Gamma_x^{TM} = \dfrac{\int_{-w}^{+w} |E_x|^2 dx}{\int_{-\infty}^{\infty} |E_x|^2 dx} \equiv \dfrac{\int_{-w}^{+w} |\psi_{TE}(x)|^2 dx}{\int_{-\infty}^{\infty} |\psi_{TE}(x)|^2 dx} \end{cases} \tag{4.3.23}$$

$$\begin{cases} \Gamma_y^{TE} = \dfrac{\int_{-t}^{+t} |E_x|^2 dy}{\int_{-\infty}^{\infty} |E_x|^2 dy} \equiv \dfrac{\int_{-t}^{+t} |\psi_{TE}(y)|^2 dy}{\int_{-\infty}^{\infty} |\psi_{TE}(y)|^2 dy} \\ \Gamma_y^{TM} = \dfrac{\int_{-t}^{+t} |E_y|^2 dy}{\int_{-\infty}^{\infty} |E_y|^2 dy} \equiv \dfrac{\int_{-t}^{+t} |\psi_{TM}(y)|^2 dy}{\int_{-\infty}^{\infty} |\psi_{TM}(y)|^2 dy} \end{cases} \tag{4.3.24}$$

The two-dimensional modal confinement factors are then

$$\begin{cases} \Gamma^{E^x_{pq}} = \Gamma_x^{TM_{p-1}} \cdot \Gamma_y^{TE_{q-1}} \\ \\ \Gamma^{E^y_{pq}} = \Gamma_x^{TE_{p-1}} \cdot \Gamma_y^{TM_{q-1}} \end{cases} \tag{4.3.25}$$

Note that the TE confinement factor Γ^{TEq-1} equals the field *power* confinement ratio. However, this is not necessarily the case for the TM confinement factor Γ^{TMp-1} as is commonly thought. This observation is made in [57] where the starting point of the confinement factor derivations is the wave equation for TE and TM rather than the complex *Poynting* theorem [66,67]. Confinement factors that do involve the *Poynting* vector can give unacceptable results for TM polarized waves under typical circumstances. For this reason, the factors Γ^{TE} and Γ^{TM} can be written as follows [69]:

$$\begin{cases} \Gamma^{TE} = \dfrac{P_{core(TE)}}{P_{Total(TE)}} \\ \\ \Gamma^{TM} = \dfrac{P_{core(TM)}}{P_{Total(TM)}} - \eta_{TM} \end{cases} \tag{4.3.26}$$

An expression of the parameter η_{TM} in terms of the slab waveguide parameters is given in [69].

III.5 Modal Gain

Under the framework of the following practical assumptions:

A3 The propagation is weakly guiding;

A4 The mode birefringence is negligible;

A5 The equivalent homogeneous active core is thought of as a single layer;

A6 The confinement factors are derived by using the appropriate configuration wave equations;

an approximation explicitly relating the modal gain $g_{\text{mod}} = -\dfrac{\beta_I^2}{\beta_R}$ to the material gain g_{mat} is given in [69]:

$$\begin{cases} g_{\text{mod}}^{E_{pq}^{x}} \cong \dfrac{g_{mat}^{TE} k^2 \Gamma_x^{TM_{p-1}} \Gamma_y^{TE_{q-1}}}{\beta_R} \\ \\ g_{\text{mod}}^{E_{pq}^{y}} \cong \dfrac{g_{mat}^{TM} k^2 \Gamma_x^{TE_{p-1}} \Gamma_y^{TM_{q-1}}}{\beta_R} \end{cases} \tag{4.3.27}$$

where k is the wavenumber in *vacuum* such that the real part of the propagation constant $\beta_R^2 = \beta_r^2 - \beta_i^2 \cong \beta_r^2$ is identical for both E_{pq}^x and E_{pq}^y modes under assumption ***A4***.

IV. Polarization-Insensitive Modal Gain Analysis

Some nominal polarization dependence is practically unavoidable. A realistic design must tolerate a residual amount of polarization, say $\delta = 2\%$ such that the modal gain ratio is allowed to deviate between pre-specified tolerance bounds.

IV.1 Problem Statement

The considered physical problem can be stated as the reduction, to within a pre-specified tolerance, of the polarization-dependent modal gain ratio of the fundamental modes E_{11}^x and E_{11}^y propagating along the rectangular core waveguide shown in figure 4.5 meanwhile the active core thickness is kept fixed and its anisotropy nature is non-altered. An optimal core width must be determined such that the corresponding electromagnetic field distribution compensates for the gain medium anisotropy. The associated mathematical problem translates to an iterative optimization of the core width such that the optical confinement factors along the lateral x-direction yield an almost unity modal gain ratio:

$$1-\delta \le \frac{g_{mat}^{TE}\,\Gamma_y^{TE_0}}{g_{mat}^{TM}\,\Gamma_y^{TM_0}} \cdot \frac{\Gamma_x^{TM_0}}{\Gamma_x^{TE_0}} \le 1+\delta \tag{4.4.1}$$

IV.2 Solution Overview

The high-level steps involved in reducing the polarization sensitivity to an acceptable tolerance are summarized in the flow chart shown in figure 4.7. It should be emphasized that the core width optimization is based on a non-linear iterative algorithm whose implementation is an adapted version of *Newton's* method. An initial intuitive estimate of the core width *W0* is required to start the calculations.

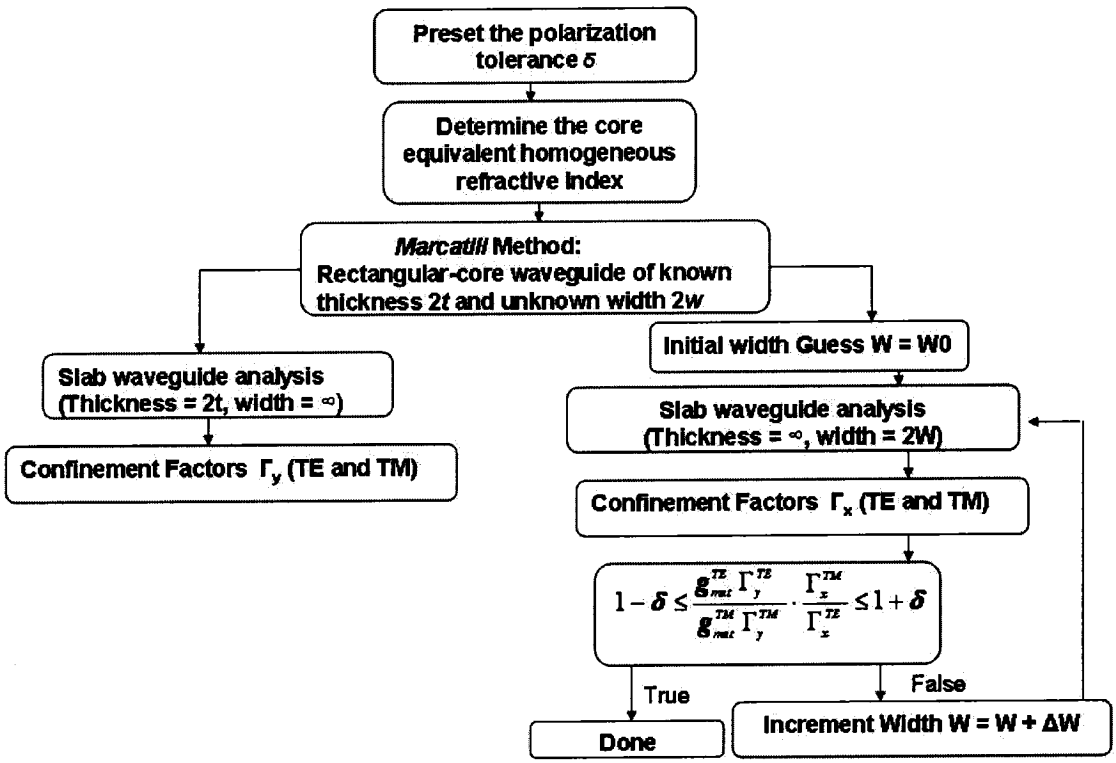

Figure 4.7: Core Width Optimization Process

IV.3 Numerical Illustrations

In figures 4.8-9, the curves labeled "1" give the strict polarization-independence condition for the fundamental mode E_{11}^{x}. The value of *2w* along these curves at a given free space wavelength gives the theoretical polarization-independent modal gain meaning a modal gain ratio of unity.

The curves labeled "*1+δ*" and "*1-δ*" give two boundaries that define the optimal range of the rectangular core width. These two curves can be used for the design of a polarization-insensitive waveguide where $\delta = 0.02$ is assumed. Since a strictly polarization-independent waveguide ($\delta = 0$) is impossible to achieve, these latter two curves set the tolerance in the design of the waveguide in terms of the tolerance allowed for the modal gain ratio.

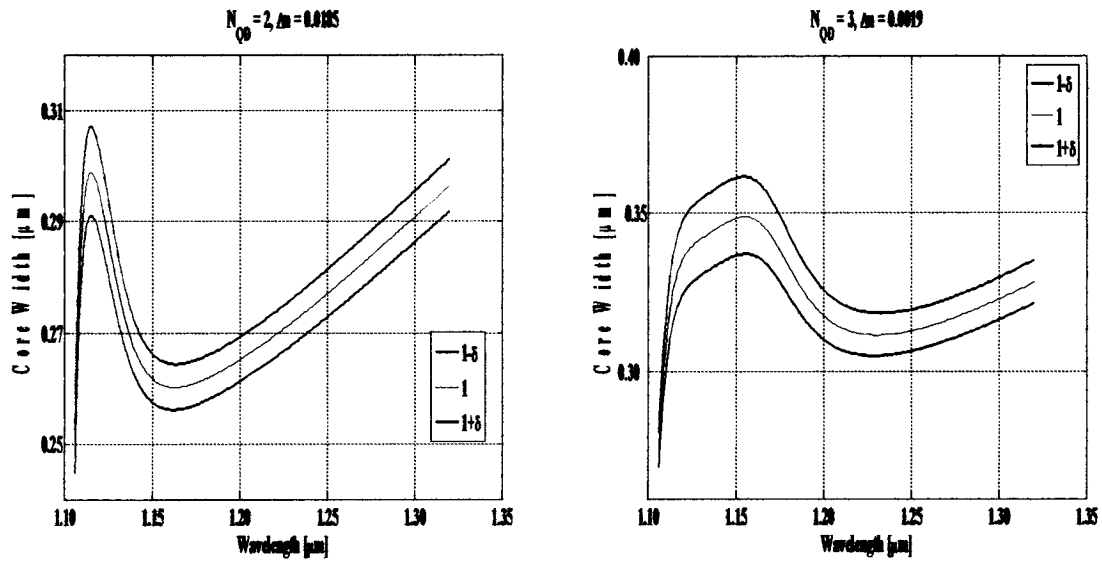

Figure 4.8: Optimal Waveguide Core Width Dispersion

The plots in figure 4.8.a correspond to an active core consisting of two quantum dot layers with thickness $2t = 37$ nm and refractive index contrast Δn=0.0185 at an *Al* molar fraction x=0.25. The material gain calculations assume one transition between the ground conduction and valence zero-dimensional discrete states such that the emission wavelength is λ_{gronnd}=1.1225 μm. An optimal core width inducing a polarization-insensitive modal gain is shown to vary between 0.284 to 0.298 μm for a free space wavelength λ=1.122 μm. The optimal aspect ratio of the rectangular core is then in the range $7.7 \leq \frac{2w}{2t} \leq 8.1$.

Moreover, the results in figure 4.8.b (4.9) correspond to an active core consisting of three

quantum dot layers with thickness $2t$ = 40.5 nm and refractive index contrast Δn=0.0019 (Δn=0.0156) at an *Al* molar fraction x=0.35 (x=0.40). The material gain calculations assume one transition between the ground conduction and valence zero-dimensional discrete states such that the emission wavelength is λ_{ground}=1.1834 μm. An optimal core width inducing a polarization-insensitive modal gain is shown to vary between 0.322 to 0.341 μm (0.289 to 0.302 μm) for a free space wavelength λ=1.183 μm. The optimal aspect ratio of the rectangular core is then in the range $8.0 \le \frac{2w}{2t} \le 8.4$ ($7.1 \le \frac{2w}{2t} \le 7.9$).

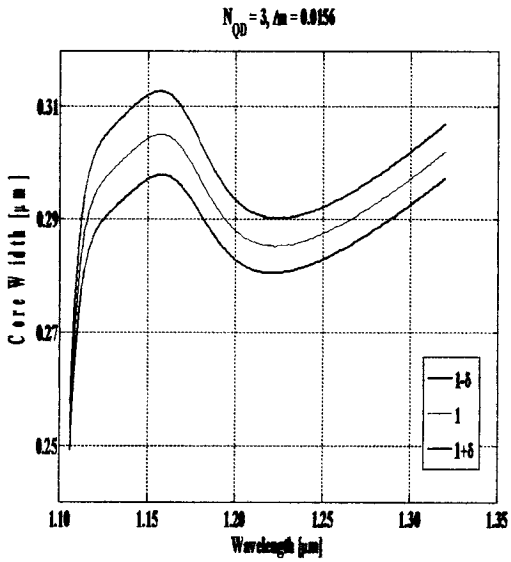

Figure 4.9: Optimal Waveguide Core Width Dispersion

The *optimal* aspect ratio does not decrease for multi-fold layer structures as it can be hastily concluded due to an appreciation of the core thickness. In fact, visually comparing figures 4.8.a and 4.9 reveals that in the latter structures the emission wavelength red-shift is accompanied by an appreciation of the optimal core width. Nonetheless, in the same multi-fold structure, the weaker the guiding the wider the core leading to a decrease in the optimal aspect ratio.

In figure 4.10 the cutoff condition for the higher-order mode E_{21}^{x} is shown so that the waveguide

supports only the fundamental mode. Note that in the case of the *symmetric* horizontal slab waveguide, the cutoff width is given by $2w_{cut-off} = \frac{\lambda}{2\sqrt{n_1^2 - n_2^2}}$ for both TE_1 and TM_1 modes. For *symmetric* vertical slab waveguide, only the TE_0 and TM_0 modes are supported for the obvious reason that $2t << \frac{\lambda}{2\sqrt{n_1^2 - n_2^2}}$ since the thickness $2t$ is in the order of tens of nanometers whereas the wavelength is in the order of a micrometer.

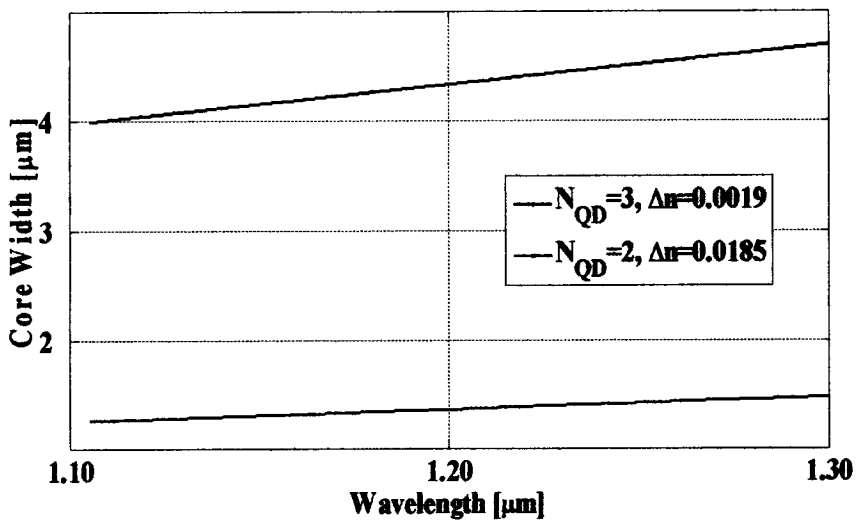

Figure 4.10 E_{21}^{x} Mode Cutoff Widths

Recall from chapter two the *InAs/GaAs* lens-shaped dots considered are $25 \times 25 \times 2.5\ nm^3$ in size and known to emit at ground state near 1.20 μm. Due to the circular base of the islands, the zero-dimensional material gain anisotropy is moderate and can be attributed for the most part to the geometrical asymmetry along the growth direction *y*. Further red-shifting of the emission wavelength near 1.30 μm can be attained by vertical stacking of the quantum dot layers as shown in table 4.1

Table 4.1: Emission Wavelengths of a Multi-Fold Layer Quantum Dot Structure

N_{QD}	1	2	3
λ_{ground} [μm]	1.1225	1.1443	1.1834
$\lambda_{excited}$ [μm]	1.0345	1.0257	1.0532

On the other hand, the emission at excited states in the wetting layer may occur near 1.0 μm wavelength range. The one-dimensional material gain due to transitions in the wetting layer is far more anisotropic than the dot gain (Refer to tables 3.1-2 in chapter three). Therefore, the observations and conclusions drawn from the depicted optimal core width profiles pertain specifically to the 1.10 – 1.30 μm wavelength range and cannot be extrapolated to the wetting layer emission wavelength region.

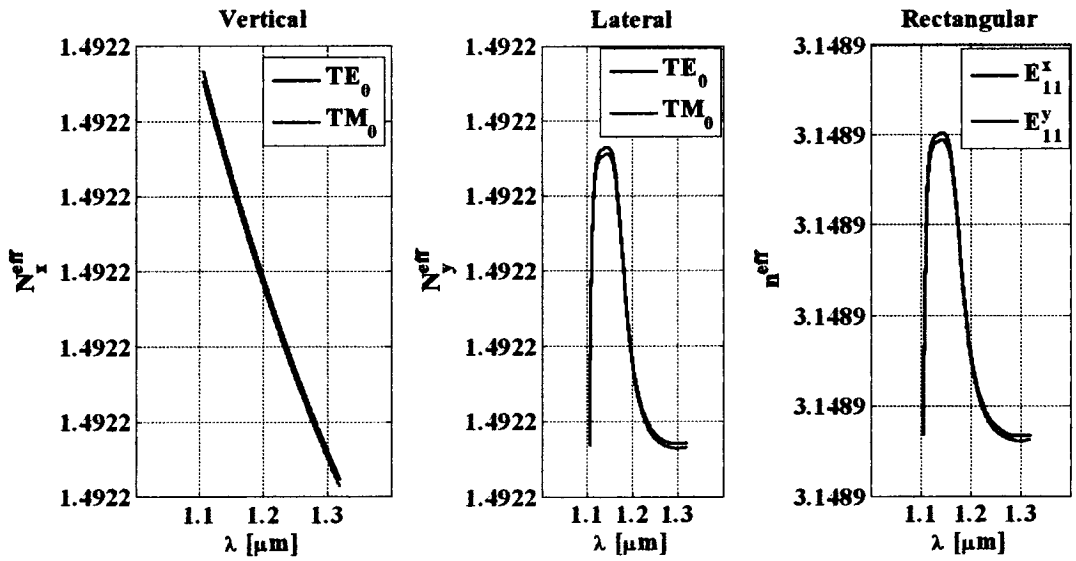

Figure 4.11: (Optimal) Effective Index Dispersion

The optimal effective index $n^{eff} = \sqrt{\left(N_x^{eff}\right)^2 + \left(N_y^{eff}\right)^2}$ has two components such that N_x^{eff} corresponds to the vertical slab waveguide of fixed thickness $2t$

whereas N_y^{eff} corresponds to the horizontal slab waveguide with an optimal width inducing a polarization-insensitive modal gain. The TE effective indices are slightly larger than the TM effective indices as shown in figure 4.11. This observation implies that the TE mode is slightly better confined to the core than is the TM mode as can be verified by the power confinement contour plots in figure 4.12. Indeed this is common knowledge and does validate the numerical results obtained here. Moreover, the rectangular effective index as shown in the rightmost plot of figure 4.11 shows very negligible fundamental mode birefringence under assumption *A4*.

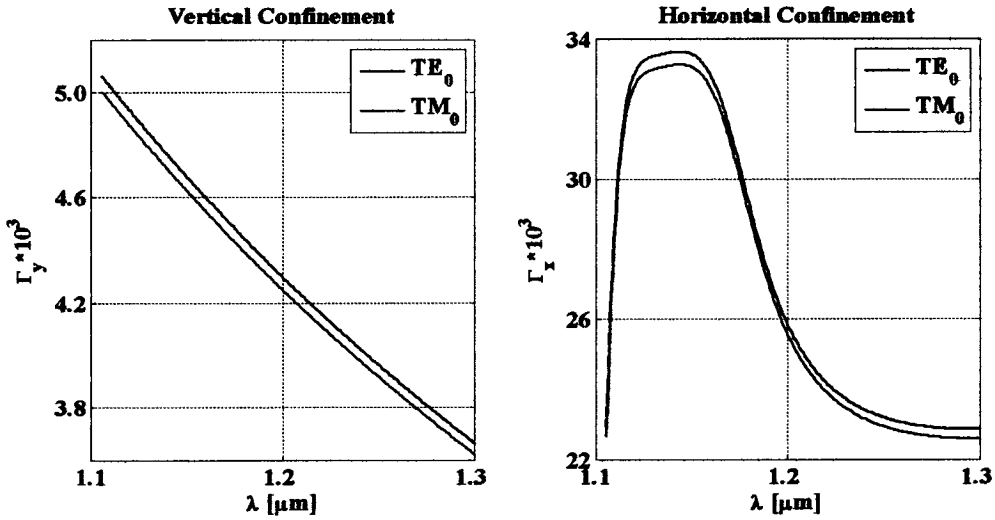

Figure 4.12: (Optimal) Power Confinement Dispersion

The multi-fold layer quantum dot structures offer a larger vertical power confinement to the active core, and hence larger modal gain, than do their single-layer counterparts. However such feature may jeopardize the performance of the waveguide as it is conducive to faster saturation.

Finally, the optimal core width under strict polarization independence is calculated for both E_{11}^x and E_{11}^y modes in the case of a weakly guiding structure where N_{QD} = 3 and Δn=0.0019. The optimal core width offset between the modes E_{11}^x and E_{11}^y is very negligible as shown in figure 4.13. This follows from the negligible modal birefringence shown in figure 4.11.

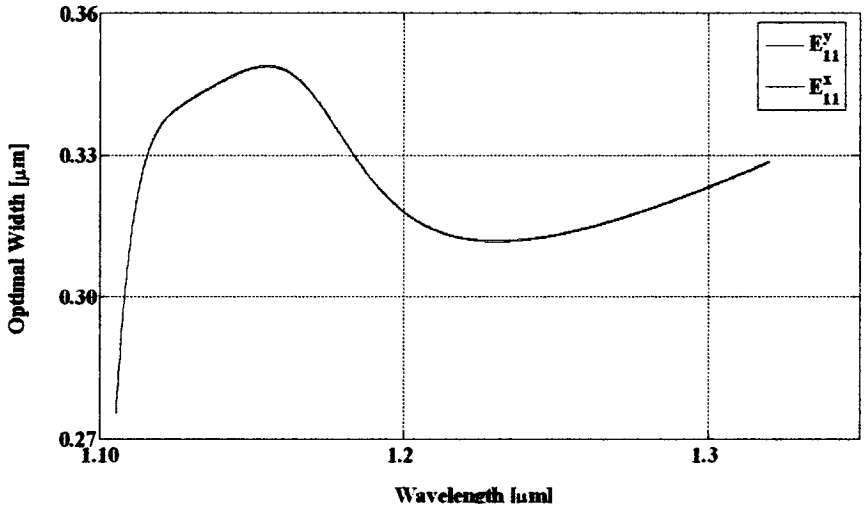

Figure 4:13: Optimal Core width Birefringence

V. Conclusion

The principle of achieving modal polarization-insensitive waveguiding has been demonstrated successfully. The *Marcatili* method allows dividing the non-planar waveguide into two separate slab structures. The indirect method used allows full real analysis by considering the passive waveguide analog. The optimization of the core width gives rise to modal confinement factors that compensate for the composite active core anisotropy. The optimized core width shows a large tolerance in particular at the material gain peak wavelength. It ensues that fabrication should not be problematic under the preset tolerance.

Chapter Five

Photonic Device Application

Owing to their intrinsic zero dimensional characteristics, quantum dots are promising novel materials for optoelectronic devices. An immediate example is semiconductor optical amplifiers with quantum dot active regions. Such versatile devices are poised to play a prominent role in the next generation photonic technology since they can perform linear amplification due to large gain and output saturation power or process ultrafast signals due to large nonlinearity. In this chapter, a near traveling-type semiconductor optical amplifier model reported in the literature is extended to quantum dot active regions under polarization-insensitive operation.

I. Device Structure

The considered semiconductor optical amplifier (SOA) has an active region consisting of three *InAs* quantum dot layers overgrown on *GaAs as* depicted in figure 5.1. Recall that each single quantum dot layer measures 3.5 nm along the growth direction corresponding to the aggregate thickness of the granular layers namely, 0.5 nm-thick *InAs* wetting layer, 2.5 nm-thick *InAs* island and 0.5 nm-thick *GaAs* spacing barrier. The lens shaped *InAs* islands have a 25 nm-wide circular base. The *GaAs* SCH layers are 15 nm-thick each. The weakly guiding amplifier waveguide has a rectangular core fully buried in a surrounding $Al_{0.65}Ga_{0.35}As$ cladding layer. Both facets are AR-coated to reduce facet reflectivity. The amplifier cavity measures 0.8 mm in length. The optimal core width amounts to 0.33 μm at the material gain peak. At each section of the amplifier cavity, the optimal width of the core is determined according to the polarization-insensitive process explained in chapter four.

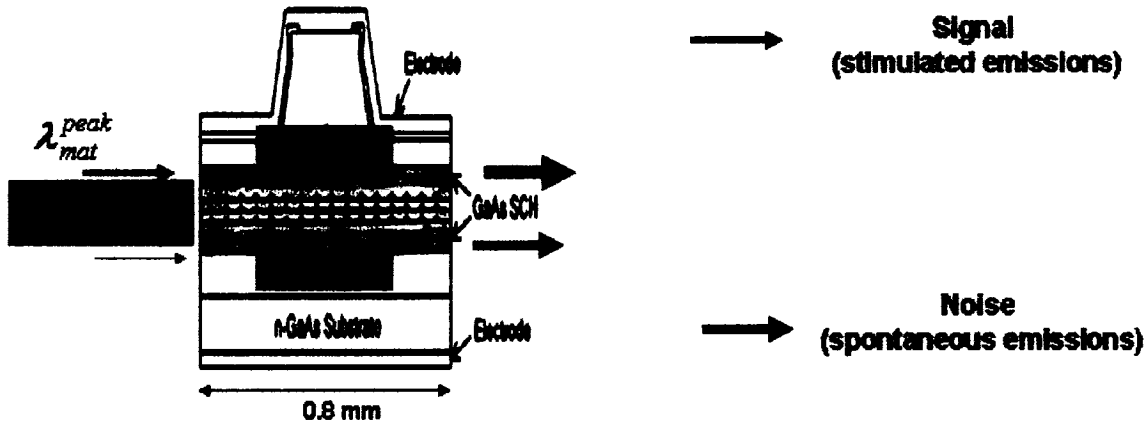

Figure 5.1: Device and Active Layer Structures

II. Amplifier Model

The SOA model proposed by *Connelly* [21-22] is adopted herein and affected with few alterations specific to a quantum dot active region. This explains why some parameters and equations (e.g. gain) used in the simulations are different than those of higher dimensional materials in [21-22]. Note that in this section, $n = n(z)$ denotes the carrier density and not the refractive index of the medium. *Connelly's* SOA model discriminates between the way the stimulated emission and spontaneous emission (ASE) are treated. A brief summary of the SOA model follows next.

II.1 Signal Propagation

The light wave representing the signal is treated coherently since its propagation through the amplifier depends on its frequency and phase (i.e. or propagation constant β) when reflecting facets are present. The following assumptions ***A7-A10*** pertain to the signal field:

. ***A7*** The input and output facets have power reflectivities R_1 and R_2 respectively.

. ***A8*** The spatially varying component of the optical field due to the signal can be decomposed into two complex traveling-waves E^+ and E^- propagating in the positive and negative z-directions respectively along the amplifier cavity.

. ***A9*** The modulus squared of the amplitude of a traveling-wave is equal to the photon rate (s^{-1}) of the wave in that direction,

$$N^{+} = \left|E^{+}\right|^{2} \text{ and } N^{-} = \left|E^{-}\right|^{2} \tag{5.2.1}$$

. ***A10*** The transverse variations (i.e. normal to the propagation direction) in the photon rates and carrier densities are negligible. (i.e. $\nabla_t N^{+} = \nabla_t N^{-} \approx 0$[9]and $\nabla_t n \approx 0$)

Assumption ***A10*** can be justified by a very thin active region of the SOA, 40.5 nm in this case. The transmitted (forward) and reflected (backward) light waves representing the signal obey the following complex traveling-wave equations:

$$\begin{cases} \dfrac{dE^{+}}{dz} = \left(-j\beta + \dfrac{1}{2}(\Gamma g_{mat}(\nu, n) - \alpha(n))\right)E^{+}(z) \\ \dfrac{dE^{-}}{dz} = \left(+j\beta - \dfrac{1}{2}(\Gamma g_{mat}(\nu, n) - \alpha(n))\right)E^{-}(z) \end{cases} \tag{5.2.2}$$

subject to the following boundary conditions:

$$\begin{cases} E^{+}(0) = \left(1 - \sqrt{R_1}\right)E_{in} + \sqrt{R_1}E^{-}(0) \\ E^{-}(L) = \sqrt{R_2}E^{+}(L) \end{cases} \tag{5.2.3}$$

where L denotes the total length of the amplifier cavity whereas Γ is the optimal two-dimensional optical confinement factor inducing polarization-insensitive modal gain of the fundamental hybrid mode E_{11}^{x} (E_{11}^{y}). $\alpha(n)$ denotes the material loss factor due to various scattering mechanisms and displays a linear dependence on the injected carrier density n such that:

$$\alpha(n) = K_0 + \Gamma K_1 n \tag{5.2.4}$$

where K_0 is the carrier-density-independent loss parameter and K_1 the carrier-dependent absorption loss coefficient. E_{in} is the input signal field at the input facet of the SOA such that:

---

[9] $\nabla_t \equiv \partial_x \hat{x} + \partial_y \hat{y}$

$$E_{in}(\nu) = \sqrt{\frac{\eta_{in} P_{in}}{h\nu}} \qquad (5.2.5)$$

where η_{in} is the input coupling loss which has been reduced down to almost 1dB recently [3]. P_{in} is the signal input power.

II.2 Noise Propagation

The ASE noise is described in terms of power alone since it distributes itself continuously over a relatively wide band of wavelengths with random phases between adjacent wavelength components. The following assumption ***A11*** pertains to the ASE:

. ***A11*** Noise photons exist only at discrete frequencies corresponding to integer multiples of cavity resonances.

Note that ***A11*** holds true since whenever reflecting facets are present, the ASE shows longitudinal cavity modes. The cavity resonant frequencies ν^{res} are multiples of the longitudinal mode frequency spacing $\Delta\nu_m$ given by

$$\Delta\nu_m = \frac{c}{2\int_0^L n_{equi}\, dz} \qquad (5.2.6)$$

where n_{equi} denotes the equivalent refractive index of the amplifier waveguide (refer to section II of chapter four). The noise frequencies $\nu_j, j = 0(1)...N_m$, are be given by

$$\nu_j = \nu_c + \Delta\nu_C + jK_m\Delta_m \qquad (5.2.7)$$

where ν_c represents the cut-off frequency at zero injected carrier density and corresponds to the effective quantum dot bandgap energy such that

$$\nu_c = \frac{E_{bandgap}^{QD}}{h} \qquad (5.2.8)$$

and $\Delta\nu_c$ represents a frequency offset to match ν_0 to a resonance frequency. K_m is a

dimensionless constant chosen according to the desired noise bandwidth.

In a frequency spacing centered around frequency ν_j, the forward and backward-traveling ASE photon rates, N_j^+ and N_j^- respectively, obeys the following traveling-wave equations:

$$\begin{cases} \dfrac{dN_j^+(z)}{dz} = +\left(\Gamma g_{mat}(\nu_j, n) - \alpha(n)\right)N_j^+ + R_{sp}(\nu_j, n) \\ \dfrac{dN_j^-(z)}{dz} = -\left(\Gamma g_{mat}(\nu_j, n) - \alpha(n)\right)N_j^- + R_{sp}(\nu_j, n) \end{cases} \tag{5.2.9}$$

subject to the following boundary conditions:

$$\begin{cases} N_j^+(0) = R_1 N_j^-(0) \\ N_j^-(0) = R_2 N_j^+(L) \end{cases} \tag{5.2.10}$$

where R_{sp} is the spontaneous emitted noise coupled into N^+ or N^-. An expression of R_{sp} is given in [22] in terms of an ideal material gain coefficient g_{mat}^{ideal} assuming no carrier density depletion, loss, reflection and so on.

$$R_{sp}(\nu_j, n) = \Gamma g_{mat}^{ideal}(\nu_j, n) K_m \Delta\nu_m \tag{5.2.11}$$

II.3 Carrier Density Rate Equations

The characterization of the carrier density in the amplifier requires both spatial and temporal analyses. At a specific longitudinal position z along the amplifier cavity, the carrier density $n(z)$ obeys the following rate equation:

$$\frac{\partial n(z)}{\partial t} = \frac{I}{etLW_{opt}(\nu)} - R(n) - \frac{\Gamma_{opt}(\nu)}{tW_{opt}(\nu)}\left\{g_{mat}(\nu, n)\left[N^+(z) + N^-(z)\right]\right\} - \frac{2}{t}\left\{\sum_{j=1}^{N_m}\frac{\Gamma_{opt}(\nu_j)}{W_{opt}(\nu_j)} g_{mat}(\nu_j, n) K_j \left[N_j^+(z) + N_j^-(z)\right]\right\}, \tag{5.2.12}$$

I denotes the bias current uniformly applied across the active region of width W_{opt}. t is the active region thickness. The injected carriers are depleted by various radiative and nonradiative

recombinations such that $R(n) = R_{rad}(n) + R_{nrad}(n)$. All (non) radiative coefficients used in the simulations are relegated to appendix C. The third and fourth terms on the RHS of the rate equation (5.2.12) represent the radiative recombination of carriers due to the amplified signal and amplified spontaneous emission (ASE) respectively.

II.4 Steady-State Model

The high-level steps involved in solving for the carrier density longitudinal distribution are summarized in the flow-chart shown in figure 5:2.

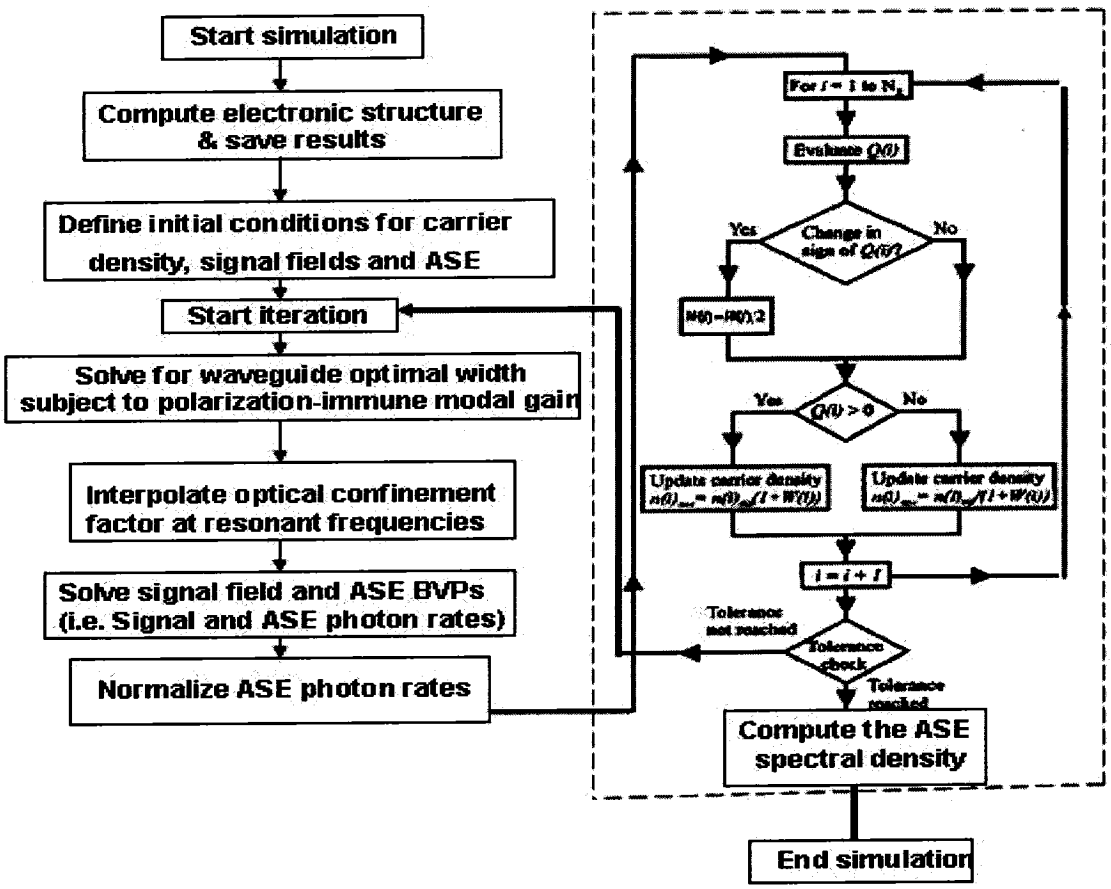

Figure 5:2 Steady-State Polarization-Insensitive SOA Amplifier Model[10]

[10] M. J. Connelly kindly offered permission to reproduce the chart enclosed within the dashed rectangle

The model iteratively calculates the carrier densities at each section of the SOA cavity and therefore requires an intuitive guess to start the computations. At steady state, an initial estimate to the carrier densities follows from a quadratic approximation which accounts solely for the carriers supplied by the bias current, radiative and nonradiative mechanisms of up to a quadratic dependence on the carrier density.

$$n^{initial} \approx \frac{-(A_{rad}+A_{nrad})+\sqrt{(A_{rad}+A_{nrad})^2+\dfrac{4I_{bias}(B_{rad}+B_{nrad})}{edLW}}}{2(B_{rad}+B_{nrad})} \tag{5.2.13}$$

The initial approximation (5.2.13) neglects the carrier density depletions due to the amplifying radiative mechanisms (i.e. stimulated and spontaneous emissions) and any other recombination mechanism with a cubic or higher dependence on the carrier density (i.e. *Auger* recombination, leakage).

II.5 Solution Overview

The cavity length is divided into a coarse partition of equidistant nodes $\{z_i\}_{i=1}^{N_{z1}} = (i-1)\cdot\Delta z$, such that $z_1 = 0$ and $z_{N_{sec}+1} = L$ at the input and output facets respectively. The uniform step-size is given by $\Delta z = \frac{L}{N_z}$. Forward (backward) finite differences are applied to the forward (backward) traveling wave equation. Incorporating the boundary conditions (5.2.3) at the extreme nodes and recasting the coupled two-point boundary value problem (BVP) (5.2.2) at the discretized nodes z_i gives rise to a set of difference equations which can be written in concise matrix form such that:

$$M.E = R \tag{5.2.14}$$

where M is the matrix of coefficients given by (case $N_z = 3$)

$$M=\begin{bmatrix} 1 & 0 & \cdots & 0 & -\sqrt{R_1} & 0 & \cdots & 0 \\ 1 & -1+w_1 & 0 & \vdots & 0 & \vdots & \vdots & \vdots \\ 0 & 1 & -1+w_2 & 0 & \vdots & \vdots & \vdots & \vdots \\ \vdots & 0 & 1 & -1+w_3 & 0 & 0 & \vdots & \vdots \\ \vdots & \vdots & 0 & 0 & -1+w_1 & 1 & 0 & \vdots \\ \vdots & \vdots & \vdots & \vdots & 0 & -1+w_2 & 1 & 0 \\ \vdots & \vdots & \vdots & 0 & \vdots & 0 & -1+w_3 & 1 \\ 0 & \cdots & 0 & -\sqrt{R_2} & 0 & \cdots & 0 & 1 \end{bmatrix}$$

w_i is the weight coefficients representing the effective gain and given by:

$$w_i=\left\{-1+\Delta z\left(-j\beta_k+\frac{1}{2}(\Gamma g_m(\nu_k,n_i)-\alpha(n_i))\right)\right\};\quad i=1:N_z \tag{5.2.15}$$

$$E=\begin{bmatrix} E^{+}{}_0 \\ \vdots \\ E^{+}_{N\sec t+1} \\ E_1^{-} \\ \vdots \\ E^{-}{}_{N\sec t+1} \end{bmatrix};\qquad R=\begin{bmatrix} (1-\sqrt{R_1})E_{in} \\ 0 \\ \vdots \\ 0 \end{bmatrix} \tag{5.2.16}$$

E is the unknown field vector and R the right hand-side vector of size $2(N_z+1)$. The facet reflectivities ($R_1, R_2 \neq 0$) cause the boundary conditions (5.2.3) to be coupled. This implies that each of the forward and backward system of difference equations cannot be solved separately. The coupled system $M.E = R$ is solved in the following manner:

1. the matrix M is factorized into LU form (i.e. M = L.U)
2. Backward substitutions yield a solution to the system $\mathrm{L.E_{temp} = R}$
3. Forward substitutions yield the solution to the system $\mathrm{U.\ E = E_{temp.}}$

Finally, similar discretization scheme and matrix factorization can be applied to the coupled two-point BVP (5.2.9) augmented with boundary conditions (5.2.10) to calculate the ASE photon rates at the selected N_m resonant frequency modes.

III. Performance Analysis

The SOA is deliberately operated near the ground state material gain peak $\lambda = 1.18 \mu m$ where the linewidth enhancement factor is minimal. The typical dot density of $\rho_{QD} = 4.10^{10}\,\mathrm{cm}^{-2}$ is used. The device temperature is 300K. The loss coefficient α assumes no background loss (Nil carrier-independent loss K_0) but only carrier-dependent loss coefficient K_1. The simulations assume no bimolecular recombination so the threshold current is approximately $I_{tr} = \frac{eN_D}{2\tau_D} \approx 0.77A$ corresponding to a threshold current density of $J_{tr} = \frac{I_{tr}}{W_{opt}L} \approx 32.1 kA.cm^{-2}$. The simulations are carried out at two injection levels of 0.5 and 2.0 A corresponding to below and above threshold respectively. Two launch power levels are considered namely, $P_{in} = -25\,dBm$ and $P_{in} = 0\,dBm$. The SOA cavity is divided into 32 sections. A total number of 40 cavity resonant frequencies are used whereas $K_m = 15$.

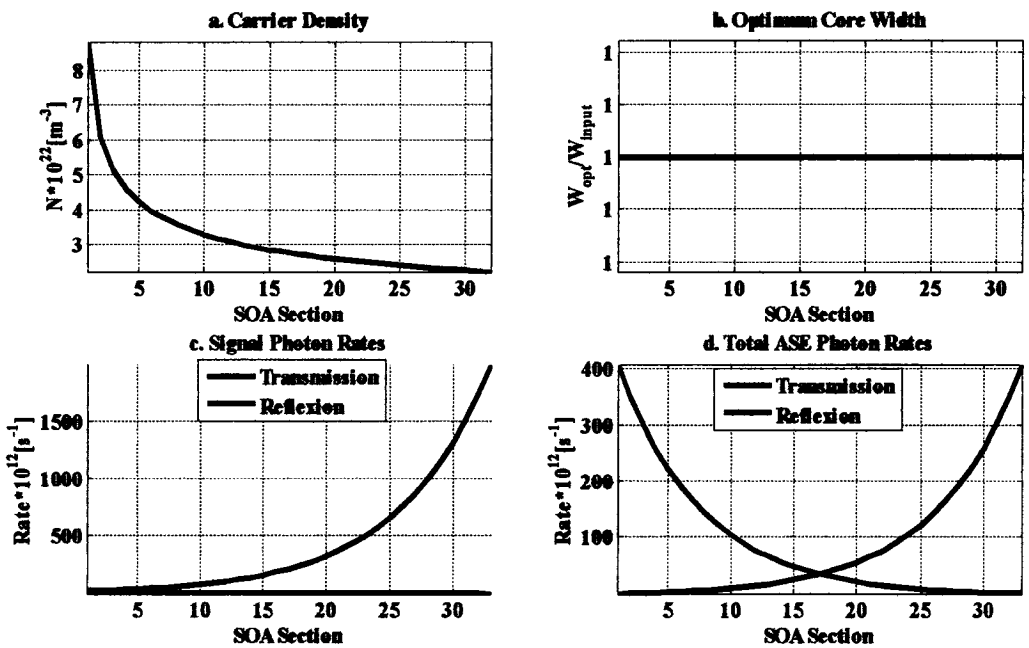

Figure 5:3 SOA Longitudinal Distributions (P_{in} = -25 dBm , I_{bias} = 0.5A)

Figures 5:3.a and 5:4.a show longitudinal distributions of the injected carrier densities. In both cases, the carrier density peaks at the input facet, it undergoes an almost exponential decay up to a quarter of the way through the cavity then it continues decaying at a rather much slower rate characteristic of saturation. Indeed, the carrier density depletion explains the amplification of the input signal as shown by the blue curves in figures 5:3.c and 5.4.c. Note that the backward-propagating signal is negligible due to low facet reflectivities as shown by the red curve in figures 5.3:c and 5:4.c.

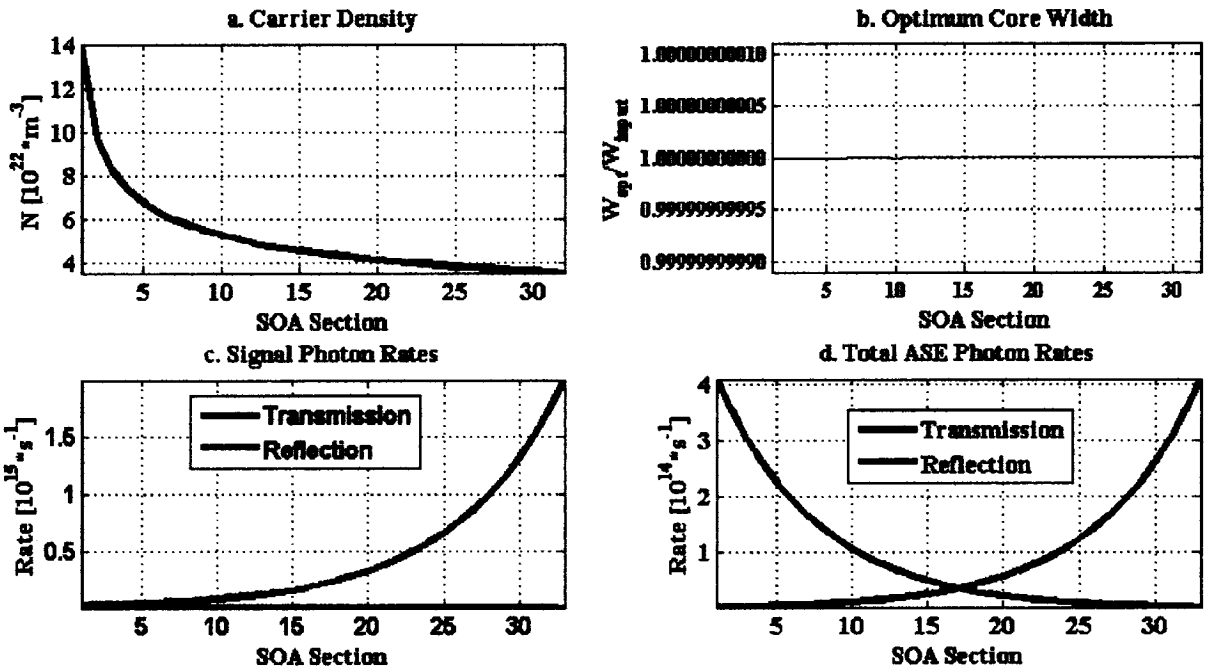

Figure 5:4 SOA Longitudinal Distributions (P_{in} = -25 dBm , I_{bias} = 2A)

Figures 5:3.b and 5:4.b simply depict the tapered profile of the SOA polarization-insensitive waveguide. They show optimal widths ratios at various transverse cross-sections along the cavity to the input section.

The carrier density depletion causes the amplification of the spontaneous emissions in the forward and backward directions as shown by the blue and red curves, respectively in figures 5:3.d and

5:4.d. It can be seen that the total ASE predicted is quite high in both directions.

The SOA chip gain profile is fitted through the resonant and anti-resonant wavelengths of the cavity. It can be seen that a gain over 19 dB can be achieved at a low input power of -25 dBm and 18 dB for a high input power of 0 dBm as shown in figure 5.5.a. The corresponding noise figures vary from a low of 5.8 dB to 8 dB as shown on figure 5.5.b. These features can be considered as a remarkable improvement over the reported results for bulk and quantum well SOAs [20, 21]. In figure 5.5.c, simulated ASE power spectra are shown for different non saturating injection and input power levels. It can be seen that at lower signal power -25 dBm, the carrier density is high producing a much larger gain than for a power of 0 dBm. Similarly, a higher injection level provides more carriers so the gain is higher as shown by the green and red curves in figure 5.5.c.

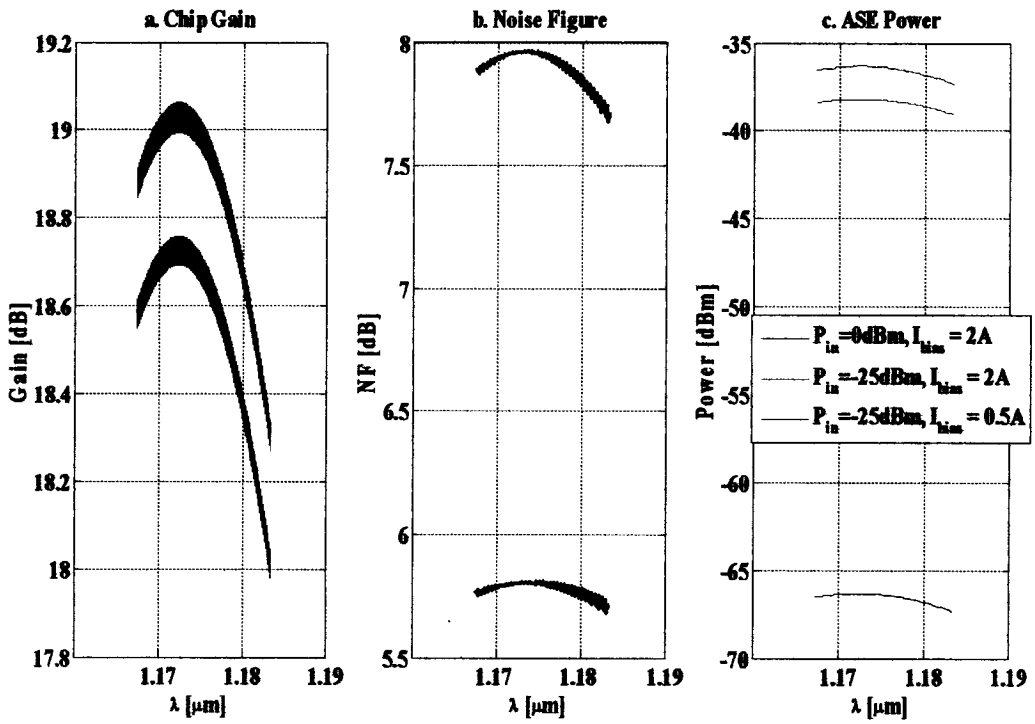

Figure 5:5 SOA Characteristic Parameters

IV. Conclusion

The steady-state performance of a polarization-insensitive quantum dot semiconductor optical amplifier was successfully shown. A high chip gain of at least 19 dB and low noise figure of at most 8 dB characterize the device considered over a 40 nm bandwidth. These results are promising for further development and improvement.

Chapter Six

Conclusion

I Epilogue

On the basis of a resonant two-level energy system, the calculated quantum dot electronic structure reveals attractive features for device applications. For a highly uniform self-assembled quantum dot ensemble minimal inhomogeneous broadening leads to a higher-bandwidth but lower-peak material gain than for a single dot (~ 10^7 m^{-1}). The modal gain is further lowered due to a small optical confinement in the order of 10^{-4}. From an SOA standpoint, this requires the cavity loss not to exceed an order of 10^{-2} m^{-1} which is achievable. On the other hand, the almost nil linewidth enhancement factor is a tremendous achievement which implies chirp free laser operation near the material gain peak.

Furthermore, a low 2% tolerance in modal polarization is achieved easily due to two reasons:

1. Only dot-located energy states are considered in the gain calculations
2. Ideal lens-shaped dots with circular base have minimal anisotropy

The merit of the polarization-insensitive process can be better demonstrated if the wetting layer located states are included in the gain calculations. This might be the case if the ground state gain is low and the device tends to lase on highly degenerate upper energy levels such as possible excited states and wetting layer states.

II Extensions

The knowledge of the growth mechanisms and structural characterizations of the self-assembly process are recommended prerequisites for an in-depth study of *realistic* quantum dot

nanostructures. A better understanding in these latter areas will yield a realistic strain representation enabling accurate modeling of the quantum dot electronic structure. Moreover, an improved gain model can be achieved through a better representation of the scattering mechanisms. In particular, this requires a homogeneous broadening model which evaluates scattering dephasing rates in terms of injected carrier densities and lattice temperature.

On the other hand, a promising extension resides in considering other practical waveguide structures (e.g. ridge, channel, side-clad, etc) such that modal optical confinement factors are derived for each layer of the active core. This implies that the assumption ***A5*** of chapter four and equivalent refractive index equation 4.2.1 need not apply.

Finally, in view of the potential functional applications such as ultrafast wavelength conversion, *Connelly's* SOA model can be further extended to include rate equations corresponding to different carrier density depleting mechanisms like spectral hole burning, two-photon absorption and so on.

Appendix A1

The Hamiltonian basis $\{u_{10}, u_{20}, u_{30}, u_{40}, u_{50}, u_{60}, u_{70}, u_{80}\}$elements are explicitly given below in terms of the spherical harmonics (i.e. normalized associated *Legendre* polynomials) and the up and down electromagnetic spins [20]:

$$u_{10}(r) \equiv \left|S\uparrow\right\rangle \equiv Y_{0,0}\uparrow = \frac{1}{\sqrt{4\pi}}\uparrow$$

$$u_{20}(r) \equiv \left|S\downarrow\right\rangle \equiv Y_{0,0}\downarrow = \frac{1}{\sqrt{4\pi}}\downarrow$$

$$u_{30}(r) \equiv \left|\frac{3}{2},\frac{3}{2}\right\rangle = \frac{-1}{\sqrt{2}}\left|(X+iY)\uparrow\right\rangle \equiv Y_{1,+1}(\theta,\varphi)\uparrow = -\sqrt{\frac{3}{8\pi}}\sin\theta e^{i\varphi}\uparrow$$

$$u_{40}(r) \equiv \left|\frac{3}{2},\frac{1}{2}\right\rangle = \frac{-1}{\sqrt{6}}\left|(X+iY)\downarrow\right\rangle + \sqrt{\frac{2}{3}}\left|Z\uparrow\right\rangle \equiv \frac{1}{\sqrt{3}}Y_{1,+1}(\theta,\varphi)\downarrow + \sqrt{\frac{2}{3}}Y_{1,0}\uparrow = -\sqrt{\frac{3}{8\pi}}\sin\theta e^{i\varphi}\downarrow + \sqrt{\frac{3}{4\pi}}\frac{z}{r}\uparrow$$

$$u_{50}(r) \equiv \left|\frac{3}{2},-\frac{1}{2}\right\rangle = \frac{1}{\sqrt{6}}\left|(X-iY)\uparrow\right\rangle + \sqrt{\frac{2}{3}}\left|Z\downarrow\right\rangle \equiv \frac{1}{\sqrt{3}}Y_{1,-1}(\theta,\varphi)\uparrow + \sqrt{\frac{2}{3}}Y_{1,0}\downarrow = \sqrt{\frac{3}{8\pi}}\sin\theta e^{-i\varphi}\uparrow + \sqrt{\frac{3}{4\pi}}\frac{z}{r}\downarrow$$

$$u_{60}(r) \equiv \left|\frac{3}{2},-\frac{3}{2}\right\rangle = \frac{1}{\sqrt{2}}\left|(X-iY)\downarrow\right\rangle \equiv Y_{1,-1}(\theta,\varphi)\downarrow = \sqrt{\frac{3}{8\pi}}\sin\theta e^{-i\varphi}\downarrow$$

$$u_{70}(r) \equiv \left|\frac{1}{2},\frac{1}{2}\right\rangle = \frac{1}{\sqrt{3}}\left|(X+iY)\downarrow\right\rangle + \frac{1}{\sqrt{3}}\left|Z\uparrow\right\rangle \equiv -\sqrt{\frac{2}{3}}Y_{1,+1}(\theta,\varphi)\downarrow + \frac{1}{\sqrt{3}}Y_{1,0}\uparrow = -\sqrt{\frac{1}{4\pi}}\sin\theta e^{i\varphi}\downarrow + \sqrt{\frac{1}{2\pi}}\frac{z}{r}\uparrow$$

$$u_{80}(r) \equiv \left|\frac{1}{2},-\frac{1}{2}\right\rangle = \frac{1}{\sqrt{3}}\left|(X-iY)\uparrow\right\rangle - \frac{1}{\sqrt{3}}\left|Z\downarrow\right\rangle \equiv \sqrt{\frac{2}{3}}Y_{1,-1}(\theta,\varphi)\uparrow - \frac{1}{\sqrt{3}}Y_{1,0}\downarrow = \sqrt{\frac{1}{4\pi}}\sin\theta e^{-i\varphi}\uparrow - \sqrt{\frac{1}{2\pi}}\frac{z}{r}\downarrow$$

Appendix A2

Expressed in the basis $\{u_{10}, u_{20}, u_{30}, u_{40}, u_{50}, u_{60}, u_{70}, u_{80}\}$ (Refer to Appendix A1) the upper triangular part U_0 of the kinetic Hamiltonian $H_0 = [L_0 \setminus U_0]$ is [36]:

$$U_0 = \begin{bmatrix} E_g + \frac{\hbar^2 k^2}{2m_c'} & 0 & Pk^+ & -\sqrt{\frac{2}{3}}Pk_z & \frac{-1}{\sqrt{3}}Pk^- & 0 & \sqrt{\frac{1}{3}}Pk_z & -\sqrt{\frac{2}{3}}Pk^- \\ & E_g + \frac{\hbar^2 k^2}{2m_c'} & 0 & \frac{1}{\sqrt{3}}Pk^+ & -\sqrt{\frac{2}{3}}Pk_z & Pk^- & \sqrt{\frac{2}{3}}Pk^+ & \frac{1}{\sqrt{3}}Pk_z \\ & & F & H^* & -I & 0 & \frac{-H^*}{\sqrt{2}} & -\sqrt{2}I \\ & & & G & 0 & I & \frac{F-G}{\sqrt{2}} & -\sqrt{\frac{3}{2}}H^* \\ & & & & G & H^* & \sqrt{\frac{3}{2}}H^* & \frac{F-G}{\sqrt{2}} \\ & & & & & F & \sqrt{2}I^* & \frac{-H}{\sqrt{2}} \\ & & & & & & -\delta + \frac{F+G}{2} & 0 \\ & & & & & & & -\delta + \frac{F+G}{2} \end{bmatrix}$$

The *Kane* parameter P is the optical matrix element that measures the coupling between the conduction and valence band edge states. Often an energy rescale of this parameter E_p, is used such that $P^2 = \frac{\hbar^2}{2m_0} E_p$; m_0 is the mass of the elementary charge at rest.

The remaining operators are defined as follows:

$$k^{\pm} = \frac{(k_x \pm ik_y)}{\sqrt{2}}, \qquad F = Ak^2 + \frac{B}{2}\left(k^2 - 3k_z^2\right), \quad G = Ak^2 - \frac{B}{2}\left(k^2 - 3k_z^2\right), \quad H = -Dk_z\left(k_x + ik_y\right),$$

$$I = \frac{\sqrt{3}}{2}B\left(k_x^2 - k_y^2\right) - iDk_xk_y .$$

The coefficients A, B, and D are further defined in terms of the *Luttinger* band structure

parameters γ_1, γ_2 and γ_3:

$$N=-3\frac{\hbar^2}{m_0}\gamma_3, \qquad M=\frac{\hbar^2}{2m_0}(2\gamma_2-\gamma_1), \qquad D=\frac{N}{\sqrt{3}}=-\sqrt{3}\frac{\hbar^2}{m_0}\gamma_3, \qquad L=-\frac{\hbar^2}{2m_0}(\gamma_1+4\gamma_2),$$

$$A=\frac{L+2M}{3}=-\frac{\hbar^2}{2m_0}\gamma_1,\ B=\frac{L-M}{3}=-\frac{\hbar^2}{m_0}\gamma_2,\ m_c=\frac{1}{2\gamma_0}=\frac{1}{4m_0}\left(\frac{m_0}{m_e^*}-\frac{E_p\left(E_g+2\delta/3\right)}{E_g\left(E_g+\delta\right)}\right).$$

m_c is the Γ valley conduction band mass of the electron whereas m_e^* is the effective electron mass.

The Hamiltonian operator $\boldsymbol{H}$ acquires extra terms when the crystal is strained. To present a simple picture of the strain effects on the dots, *Pikus and Bir* formulation is adopted herein. Due to the same underlying symmetry, the strain part $\boldsymbol{H_{str}}$ can be obtained from the kinetic part $\boldsymbol{H_0}$ by the following substitutions, in terms of the strain tensor ε components and the deformation potentials a_c, a_v, b and d:

$$k_\alpha k_\beta \leftrightarrow \varepsilon_{\alpha\beta}$$

$$\frac{\hbar^2}{2m_e^*}\leftrightarrow -a_c, \quad \frac{\hbar^2}{2m_0}\gamma_1\leftrightarrow -a_v, \qquad \frac{\hbar^2}{2m_0}\gamma_2\leftrightarrow -\frac{b}{2}, \qquad \frac{\hbar^2}{2m_0}\gamma_3\leftrightarrow -\frac{d}{2\sqrt{3}}$$

$$F+G\leftrightarrow 2a(\varepsilon_{xx}+\varepsilon_{yy}+\varepsilon_{zz}), \quad F-G\leftrightarrow b(\varepsilon_{xx}+\varepsilon_{yy}-2\varepsilon_{zz})$$

$$H\leftrightarrow d(\varepsilon_{zx}+i\varepsilon_{zy}), \qquad I\leftrightarrow\frac{\sqrt{3}}{2}b(\varepsilon_{xx}-\varepsilon_{yy})-id\varepsilon_{xy}.$$

Neglecting the shear strain components would *essentially* result in a diagonal contribution to the effective Hamiltonian $\boldsymbol{H}$. The remaining non-zero contributions to the strain Hamiltonian are due to the spin-orbit terms. The trace of the strain tensor $Tr(\varepsilon)=\varepsilon_{xx}+\varepsilon_{yy}+\varepsilon_{zz}$ is referred to as hydrostatic strain. It is exactly the fractional change of the volume of the crystal under deformation. The quantity $2\varepsilon_{zz}-\varepsilon_{xx}-\varepsilon_{yy}$ is referred to as shear strain. More often, an energy rescale of the last two strains are introduced as the hydrostatic and shear deformation potentials, defined respectively as $\partial E_{hy}=-a_g(\varepsilon_{xx}+\varepsilon_{yy}+\varepsilon_{zz})$ and $\partial E_{sh}=b(2\varepsilon_{zz}-\varepsilon_{xx}-\varepsilon_{yy})$, where

$a_g = a_c - a_v$ is the hydrostatic deformation potential.

In the context of the current work, a lattice-mismatched strain is considered, such that

$$\varepsilon_{xx} = \varepsilon_{yy} = \frac{a_0 - a}{a} \qquad \text{and} \qquad \varepsilon_{zz} = -2\frac{C_{12}}{C_{11}}\varepsilon_{xx},$$

where a_0 and a are the lattice constants of the barrier material (i.e. *GaAs*) and dot material (i.e. *InAs*) respectively meanwhile C_{11} and C_{12} are the elastic stiffness coefficients.

Appendix A3

Table A.1: Useful Band Structure Parameters [68]

Parameter	*InAs*	*GaAs*	Unit
a_{lc}: Lattice Constant at $T = 300\ K$	6.0583	5.65325	
E_g : Energy Gap (Gamma Valley)	0.417	1.519	eV
δ: Spin-Orbit Split-Off Energy	0.39	0.341	eV
m_e^*: Electron Effective Mass	0.0053 [0.026]	0.067	e.m.u.[11]
$m_{so^*}^*$: Spin-Orbit Effective Mass	0.14	0.172	e.m.u.
E_p: Optical Matrix Element	21.5	28.8	eV
VBO: Valence Band Offset	-0.36 [-0.59]	-0.80	eV
CBO: Conduction Band Offset	0.58 [0.89]	- -	eV
ΔE_v : Heterojunction Valence Band Offset	0.21		eV
γ_1: Luttinger parameter	15.45 [20.0]	6.98	
γ_2: Luttinger parameter	1.843 [8.5]	2.06	
γ_3: Luttinger parameter	9.2	2.93	
a_c: Conduction Deformation Potential	-5.95 [-5.08]	-7.17	eV
a_v: Valence Deformation Potential	1.00	1.16	eV
b: Shear Deformation Potential	-1.8	-2.0	eV
d: Shear Deformation Potential	-3.6	-4.8	eV
C_{11}: Elastic Stiffness Coefficient	832.9	1221	GPa
C_{12}: Elastic Stiffness Coefficient	452.6	566	GPa
C_{44}: Elastic Stiffness Coefficient	395.9	600	GPa
Bulk Modulus	5.8×10^{10}	7.53×10^{10}	GPa
Young's Modulus	5.14×10^{10}	8.59×10^{10}	Gpa
Poisson's Ratio	0.35	0.31	

Appendix B

The electron wave vector $\vec{k}$ is assumed to have a general direction specified by the following spherical coordinates θ and ϕ:

$$\vec{k} = k\sin\theta\cos\phi\,\hat{x} + k\sin\theta\sin\phi\,\hat{y} + k\cos\theta\,\hat{z}\,.$$

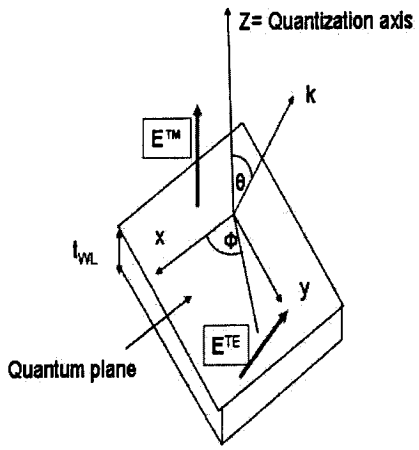

Figure B.1: Geometry of Quantum Well Structure [71]

Using the following coordinate transformations,

$$\begin{bmatrix}\uparrow'\\ \downarrow'\end{bmatrix} = \begin{bmatrix} e^{-i\frac{\phi}{2}}\cos\frac{\theta}{2} & e^{i\frac{\phi}{2}}\sin\frac{\theta}{2} \\ -e^{-i\frac{\phi}{2}}\sin\frac{\theta}{2} & e^{i\frac{\phi}{2}}\cos\frac{\theta}{2}\end{bmatrix}\cdot\begin{bmatrix}\uparrow\\ \downarrow\end{bmatrix}$$

and

$$\begin{bmatrix}X'\\ Y'\\ Z'\end{bmatrix} = \begin{bmatrix}\cos\theta\cos\phi & \cos\theta\sin\phi & -\sin\theta\\ -\sin\phi & \cos\phi & 0\\ \sin\theta\cos\phi & \sin\theta\sin\phi & \cos\theta\end{bmatrix}\cdot\begin{bmatrix}X\\ Y\\ Z\end{bmatrix}$$

The band edge functions in the new primed coordinate system are:

Conduction band

$\left|iS\downarrow'\right\rangle$ and $\left|iS\uparrow'\right\rangle$

Heavy hole subband

$$\left|\frac{3}{2},\frac{3}{2}\right\rangle' = \frac{-1}{\sqrt{2}}\left|(X'+iY')\uparrow'\right\rangle = \frac{-1}{\sqrt{2}}\left|(\cos\theta\cos\phi - i\sin\phi)X + (\cos\theta\sin\phi + i\cos\phi)Y - \sin\theta Z\right|\uparrow'\rangle$$

$$\left|\frac{3}{2},-\frac{3}{2}\right\rangle' = \frac{-1}{\sqrt{2}}\left|(X'-iY')\downarrow'\right\rangle = \frac{1}{\sqrt{2}}\left|(\cos\theta\cos\phi + i\sin\phi)X + (\cos\theta\sin\phi - i\cos\phi)Y - \sin\theta Z\right|\downarrow'\rangle$$

Light hole subband

$$\left|\frac{3}{2},\frac{1}{2}\right\rangle' = \frac{-1}{\sqrt{6}}\left|(X'-iY')\downarrow'\right\rangle + \sqrt{\frac{2}{3}}\left|Z'\uparrow'\right\rangle = \frac{-1}{\sqrt{6}}\left|(\cos\theta\cos\phi - i\sin\phi)X + (\cos\theta\sin\phi + i\cos\phi)Y - \sin\theta Z\right|\downarrow'\rangle + \sqrt{\frac{2}{3}}\left|\sin\theta\cos\phi X + \sin\theta\sin\phi Y + \cos\theta Z\right|\uparrow'\rangle$$

$$\left|\frac{3}{2},-\frac{1}{2}\right\rangle' = \frac{1}{\sqrt{6}}\left|(X'-iY')\uparrow'\right\rangle + \sqrt{\frac{2}{3}}\left|Z'\downarrow'\right\rangle = \frac{1}{\sqrt{6}}\left|(\cos\theta\cos\phi + i\sin\phi)X + (\cos\theta\sin\phi - i\cos\phi)Y - \sin\theta Z\right|\uparrow'\rangle + \sqrt{\frac{2}{3}}\left|\sin\theta\cos\phi X + \sin\theta\sin\phi Y + \cos\theta Z\right|\downarrow'\rangle$$

Spin Orbit sub-band

$$\left|\frac{1}{2},\frac{1}{2}\right\rangle' = \frac{1}{\sqrt{3}}\left|(X'-iY')\downarrow'\right\rangle + \frac{1}{\sqrt{3}}\left|Z'\uparrow'\right\rangle = \frac{1}{\sqrt{3}}\left|(\cos\theta\cos\phi - i\sin\phi)X + (\cos\theta\sin\phi + i\cos\phi)Y - \sin\theta Z\right|\downarrow'\rangle + \frac{1}{\sqrt{3}}\left|\sin\theta\cos\phi X + \sin\theta\sin\phi Y + \cos\theta Z\right|\uparrow'\rangle$$

$$\left|\frac{1}{2},-\frac{1}{2}\right\rangle' = \frac{1}{\sqrt{3}}\left|(X'-iY')\uparrow'\right\rangle - \frac{1}{\sqrt{3}}\left|Z'\downarrow'\right\rangle = \frac{1}{\sqrt{3}}\left|(\cos\theta\cos\phi + i\sin\phi)X + (\cos\theta\sin\phi - i\cos\phi)Y - \sin\theta Z\right|\uparrow'\rangle - \frac{1}{\sqrt{3}}\left|\sin\theta\cos\phi X + \sin\theta\sin\phi Y + \cos\theta Z\right|\downarrow'\rangle.$$

The *Kane* parameter P and momentum matrix parameter P_x are defined as [20]

$$P = \frac{\hbar}{m_0}\langle iS|P_z|Z\rangle = \frac{\hbar}{m_0}P_x$$

$$P_x = \langle iS|p_x|X\rangle = \langle iS|p_y|Y\rangle = \langle iS|p_z|Z\rangle$$

For conduction to heavy hole transitions, the matrix elements M_{C-HH} are:

$$\left\langle iS\uparrow\left|p\right|\frac{3}{2},\frac{3}{2}\right\rangle = -[(\cos\theta\cos\phi - i\sin\phi)\hat{x} + (\cos\theta\sin\phi + i\cos\phi)\hat{y} - \sin\theta\hat{z}]\frac{P_x}{\sqrt{2}},$$

$$\left\langle iS\downarrow\left|p\right|\frac{3}{2},-\frac{3}{2}\right\rangle = [(\cos\theta\cos\phi + i\sin\phi)\hat{x} + (\cos\theta\sin\phi - i\cos\phi)\hat{y} - \sin\theta\hat{z}]\frac{P_x}{\sqrt{2}},$$

$$\left\langle iS\uparrow\left|p\right|\frac{3}{2},-\frac{3}{2}\right\rangle = \left\langle iS\downarrow\left|p\right|\frac{3}{2},\frac{3}{2}\right\rangle = 0.$$

For conduction to light hole transitions, the matrix elements M_{C-LH} are:

$$\left\langle iS\uparrow\left|p\right|\frac{3}{2},\frac{1}{2}\right\rangle = \sqrt{\frac{2}{3}}[(\sin\theta\cos\phi)\hat{x} + (\sin\theta\sin\phi)\hat{y} + \cos\theta\hat{z}]P_x,$$

$$\left\langle iS\downarrow\left|p\right|\frac{3}{2},-\frac{1}{2}\right\rangle = \sqrt{\frac{2}{3}}[(\sin\theta\cos\phi)\hat{x} + (\sin\theta\sin\phi)\hat{y} + \cos\theta\hat{z}]P_x,$$

$$\left\langle iS\uparrow\left|p\right|\frac{3}{2},-\frac{1}{2}\right\rangle = \frac{1}{\sqrt{6}}[(\cos\theta\cos\phi + i\sin\phi)\hat{x} + (\cos\theta\sin\phi - i\cos\phi)\hat{y} - \sin\theta\hat{z}]P_x,$$

$$\left\langle iS\downarrow\left|p\right|\frac{3}{2},\frac{1}{2}\right\rangle = -\frac{1}{\sqrt{6}}[(\cos\theta\cos\phi - i\sin\phi)\hat{x} + (\cos\theta\sin\phi + i\cos\phi)\hat{y} - \sin\theta\hat{z}]P_x.$$

For conduction to spin orbit transitions, the matrix elements M_{C-SO} are:

$$\left\langle iS\uparrow\left|p\right|\frac{1}{2},\frac{1}{2}\right\rangle = \sqrt{\frac{1}{3}}[(\sin\theta\cos\phi)\hat{x} + (\sin\theta\sin\phi)\hat{y} + \cos\theta\hat{z}]P_x,$$

$$\left\langle iS\downarrow\left|p\right|\frac{1}{2},-\frac{1}{2}\right\rangle = -\sqrt{\frac{1}{3}}[(\sin\theta\cos\phi)\hat{x} + (\sin\theta\sin\phi)\hat{y} + \cos\theta\hat{z}]P_x,$$

$$\left\langle iS\uparrow\left|p\right|\frac{1}{2},-\frac{1}{2}\right\rangle = \sqrt{\frac{1}{3}}[(\cos\theta\cos\phi + i\sin\phi)\hat{x} + (\cos\theta\sin\phi - i\cos\phi)\hat{y} - \sin\theta\hat{z}]P_x,$$

$$\left\langle iS\downarrow\left|p\right|\frac{1}{2},\frac{1}{2}\right\rangle = \sqrt{\frac{1}{3}}[(\cos\theta\cos\phi - i\sin\phi)\hat{x} + (\cos\theta\sin\phi + i\cos\phi)\hat{y} - \sin\theta\hat{z}]P_x.$$

The spin-degenerate squared matrix elements $M^2_{c\_v}$ of the conduction to valence band transitions are in the case of TE polarization (i.e. $\hat{e} = \hat{x}$ or $\hat{e} = \hat{y}$)

$$|\hat{e}\cdot p_{CV}|^2 \equiv |\hat{x}\cdot p_{C-HH}|^2 = \left(\left|\left\langle iS\uparrow' \left| p_x \right| \frac{3}{2},\frac{3}{2}\right\rangle'\right|^2 + \left|\left\langle iS\uparrow' \left| p_x \right| \frac{3}{2},-\frac{3}{2}\right\rangle'\right|^2\right) = \frac{3}{2}\left(\cos^2\theta\cos^2\phi+\sin^2\phi\right)M_b^2$$

$$|\hat{e}\cdot p_{CV}|^2 \equiv |\hat{x}\cdot p_{C-LH}|^2 = \left(\left|\left\langle iS\uparrow' \left| p_x \right| \frac{3}{2},\frac{1}{2}\right\rangle'\right|^2 + \left|\left\langle iS\uparrow' \left| p_x \right| \frac{3}{2},-\frac{1}{2}\right\rangle'\right|^2\right) = \left(2\sin^2\theta\cos^2\phi+\frac{1}{2}\left[\left(\cos^2\theta\cos^2\phi+\sin^2\phi\right)\right]\right)$$

$$|\hat{e}\cdot p_{CV}|^2 \equiv |\hat{x}\cdot p_{C-SO}|^2 = \left(\left|\left\langle iS\uparrow' \left| p_x \right| \frac{1}{2},\frac{1}{2}\right\rangle'\right|^2 + \left|\left\langle iS\uparrow' \left| p_x \right| \frac{1}{2},-\frac{1}{2}\right\rangle'\right|^2\right) = M_b^2$$

The spin-degenerate squared matrix elements $M_{c\_v}^2$ of the conduction to valence band transitions are in the case of TM polarization (i.e. $\hat{e}=\hat{z}$)

$$|\hat{e}\cdot p_{CV}|^2 \equiv |\hat{z}\cdot p_{C-HH}|^2 = \left(\left|\left\langle iS\uparrow' \left| p_x \right| \frac{3}{2},\frac{1}{2}\right\rangle'\right|^2 + \left|\left\langle iS\uparrow' \left| p_x \right| \frac{3}{2},-\frac{1}{2}\right\rangle'\right|^2\right) = \frac{3}{2}\sin^2\phi M_b^2$$

$$|\hat{e}\cdot p_{CV}|^2 \equiv |\hat{z}\cdot p_{C-LH}|^2 = \left(\left|\left\langle iS\uparrow' \left| p_x \right| \frac{3}{2},\frac{1}{2}\right\rangle'\right|^2 + \left|\left\langle iS\uparrow' \left| p_x \right| \frac{3}{2},-\frac{1}{2}\right\rangle'\right|^2\right) = \left(2\cos^2\theta+\frac{1}{2}\sin^2\theta\right)M_b^2$$

$$|\hat{e}\cdot p_{CV}|^2 \equiv |\hat{z}\cdot p_{C-SO}|^2 = \left(\left|\left\langle iS\uparrow' \left| p_x \right| \frac{1}{2},\frac{1}{2}\right\rangle'\right|^2 + \left|\left\langle iS\uparrow' \left| p_x \right| \frac{1}{2},-\frac{1}{2}\right\rangle'\right|^2\right) = M_b^2$$

The momentum matrix elements need to be averaged depending on the crystal symmetry. The averaging procedures varies according to the dimension of the material (i.e. quantum confinement dimension).

For a bulk zinc blende semiconductor, the averaging is done over the solid angle and the resulting *isotropic* bulk matrix element M_b^2 is given by

$$\left\langle \left|\hat{e}\cdot p_{C\_V}\right|^2 \right\rangle_{bulk} = \frac{1}{4\pi}\int_0^{\pi}\int_0^{2\pi} d\theta d\phi \left|\hat{e}\cdot M_{C\_V}\right|^2 = M_b^2$$

$$M_b^2 = \left|\hat{e}\cdot p_{CV}\right|^2 \equiv \left\langle \left|\hat{e}\cdot M_{C-V}\right|^2 \right\rangle = \frac{1}{3}P_x^2,$$

where $\hat{e}=\hat{x}$ or $\hat{e}=\hat{y}$ for in-plane polarization (i.e. TE) and $\hat{e}=\hat{z}$ for polarization along the growth direction (i.e. TM).

In the case of quantum wells (i.e. One dimensional quantum confinement along the growth

direction $\hat{z}$), the momentum matrix element is averaged over the azimuthal angle $0 \le \phi \le 2\pi$ in the plane of the quantum well. The squared momentum matrix element can be expressed in terms of the bulk matrix element $M_{QW}^2 = A_{CV}^{\hat{e}} M_b^2$, where $A_{CV}^{\hat{e}}$ denotes the anisotropy factor for a dipole transition between conduction band C and valence band V and the field polarization lies along the direction $\hat{e}$.

For quantum wells, the averaging of the squared momentum matrix element expressions yields then in the case of TE polarization:

$$\left\langle \left| \hat{x} \cdot M_{C\_HH} \right|^2 \right\rangle_{QW} = \frac{3M_b^2}{4\pi} \int_0^{2\pi} d\phi \left(\cos^2\theta \cos^2\phi + \sin^2\phi \right) = \frac{3}{4}\left(1 + \cos^2\theta\right) M_b^2$$

$$\left\langle \left| \hat{x} \cdot M_{C\_LH} \right|^2 \right\rangle_{QW} = \frac{M_b^2}{2\pi} \int_0^{2\pi} d\phi \left(2\sin^2\theta \cos^2\phi + \frac{1}{2}\left[\left(\cos^2\theta \cos^2\phi + \sin^2\phi \right) \right] \right) = \frac{1}{4}\left(5 - 3\cos^2\theta\right) M_b^2$$

$$\left\langle \left| \hat{x} \cdot M_{C\_SO} \right|^2 \right\rangle_{QW} = \frac{M_b^2}{2\pi} \int_0^{2\pi} d\phi = M_b^2$$

For quantum wells, the averaging of the squared momentum matrix element expressions yields then in the case of TE polarization:

$$\left\langle \left| \hat{z} \cdot M_{C\_HH} \right|^2 \right\rangle_{QW} = \frac{3M_b^2}{4\pi} \int_0^{2\pi} d\phi \sin^2\phi = \frac{3}{2}\sin^2\theta M_b^2$$

$$\left\langle \left| \hat{z} \cdot M_{C\_LH} \right|^2 \right\rangle_{QW} = \frac{M_b^2}{2\pi} \int_0^{2\pi} d\phi \left(2\cos^2\theta + \frac{1}{2}\sin^2\theta \right) = \frac{1}{2}\left(1 + 3\cos^2\theta\right) M_b^2$$

$$\left\langle \left| \hat{z} \cdot M_{C\_SO} \right|^2 \right\rangle_{QW} = \frac{M_b^2}{2\pi} \int_0^{2\pi} d\phi = M_b^2$$

Likewise for quantum dots, The momentum matrix element can be expressed in terms of the bulk matrix element $M_{QD}^2 = A_{CV} M_b^2$. This time, the momentum matrix element is averaged over the azimuthal angle $0 \le \phi \le 2\pi$ and polar angle $-\frac{\pi}{2} \le \theta \le \frac{\pi}{2}$ of the dot lens-shape geometry.

The averaging of the squared momentum matrix element expressions yields then in the case of TE polarization:

$$\left\langle \left| \hat{x} \cdot M_{C\_HH} \right|^2 \right\rangle_{QD} = \frac{3M_b^2}{4\pi^2} \int_0^{2\pi} \int_{-\frac{\pi}{2}}^{\frac{\pi}{2}} d\theta d\phi \left(\cos^2\theta \cos^2\phi + \sin^2\phi \right) = \frac{9}{8} M_b^2$$

$$\left\langle \left| \hat{x} \cdot M_{C\_LH} \right|^2 \right\rangle_{QD} = \frac{M_b^2}{2\pi^2} \int_0^{2\pi} \int_{-\frac{\pi}{2}}^{\frac{\pi}{2}} d\theta d\phi \left(2\sin^2\theta \cos^2\phi + \frac{1}{2} \left[\left(\cos^2\theta \cos^2\phi + \sin^2\phi \right) \right] \right) = \frac{7}{8} M_b^2$$

$$\left\langle \left| \hat{x} \cdot M_{C\_SO} \right|^2 \right\rangle_{QD} = \frac{M_b^2}{2\pi^2} \int_0^{2\pi} \int_{-\frac{\pi}{2}}^{\frac{\pi}{2}} d\theta d\phi = M_b^2$$

The averaging of the squared momentum matrix element expressions yields then in the case of TM polarization:

$$\left\langle \left| \hat{z} \cdot M_{C\_HH} \right|^2 \right\rangle_{QD} = \frac{3M_b^2}{4\pi^2} \int_0^{2\pi} \int_{-\frac{\pi}{2}}^{\frac{\pi}{2}} d\theta d\phi \sin^2\phi = \frac{6}{8} M_b^2$$

$$\left\langle \left| \hat{z} \cdot M_{C\_LH} \right|^2 \right\rangle_{QD} = \frac{M_b^2}{2\pi^2} \int_0^{2\pi} \int_{-\frac{\pi}{2}}^{\frac{\pi}{2}} d\theta d\phi \left(2\cos^2\theta + \frac{1}{2} \sin^2\theta \right) = \frac{10}{8} M_b^2$$

$$\left\langle \left| \hat{z} \cdot M_{C\_SO} \right|^2 \right\rangle_{QD} = \frac{M_b^2}{2\pi^2} \int_0^{2\pi} \int_{-\frac{\pi}{2}}^{\frac{\pi}{2}} d\theta d\phi = M_b^2$$

Appendix C

Table C:1: Useful Parameters Used in SOA Simulations [32]

Constant	Value	S.I. Unit
Planck's Constant (h)	$6.62606876.10^{-34}$	J.s
Speed of light in vacuum (c)	299792458	$m.s^{-1}$
Permittivity in free space (ε_0)	$8.854187817.10^{-12}$	$F.m^{-1}$
Electron elementary charge (e)	$1.602176462.10^{-19}$	C
Boltzman Constant (k_B)	$1.3806503.10^{-23}$	$J.K^{-1}$
Active region length (L)	8.10^{-3}	m
Input (output) Coupling Loss η_{in} (η_{out})	1.0	dB
Carrier dependent absorption loss coefficient (K_1)	7500.10^{-24}	m^2
Carrier independent absorption loss coefficient (K_0)	0	m^{-1}
Input (output) Facet Reflectivity R_1 (R_2)	5.10^{-5}	
Linear radiative recombination coefficient (A_{rad})	$3.0.10^{-8}$	s^{-1}
Linear nonradiative recombination coefficient due to traps (A_{nrad})	$5.0.10^{-8}$	$m^3.s^{-1}$
Bimolecular radiative recombination coefficient (B_{rad})	$1.1.10^{-16}$	$m^3.s^{-1}$
Bimolecular nonradiative recombination coefficient (B_{rad})	0	$m^3.s^{-1}$
Auger recombination coefficient (C_{aug})	$2.2.10^{-33}$	$m^6.s^{-1}$
Leakage recombination coefficient (D_{leak})	0	$m^{13.5}.s^{-1}$
line broadening (τ_{in})	$0.1.10^{-12}$	s^{-1}

Bibliography

[1] S. Adachi, Physical Properties of III-V Semiconductor Compounds InP, InAs, GaP, InGaAs and InGaAsP. "*John Wiley & Sons Inc. Publications*", 1992. ISBN 0-471-57329-9.

[2] G.P. Agrawal, Fiber-Optic Communication Systems. "*John Wiley & Sons Inc. Publications*". 2002. ISBN 0-471-21571-6.

[3] T. Akiyama, M. Ekawa, M. Sugawara, K. Kawaguchi, H. Sudo, A. Kuramata, H. Ebe and Y. Arakawa, "An Ultrawide-Band semiconductor Optical Amplifier Having an Extremely High Penalty-Free Output Power of 23 dBm Achieved with quantum Dots", *IEEE Photonics Technology Letters*, vol. 17, no. 8, pp. 1614-1616, August 2005.

[4] T. Akiyama, N. Hatori, H. Ebe, M. Sugawara, "Pattern-Effect-Free Semiconductor Optical Amplifier Achieved Using quantum Dots," *IEEE Electronic Letters*, vol. 38, no. 19, pp. 1139-1140, September 2002.

[5] T. Akiyama, H. Kuwatsuka, N. Hatori, Y. Nakata, H. Ebe and M. Sugawara, "Symmetric Highly Efficient (~ 0 dB) Wavelength Conversion Based on Four-Wave Mixing in Quantum Dot Optical Amplifiers," *IEEE Photonics Technology Letters*, vol. 14, no. 8, pp. 1139-1141, August 2002.

[6] T. Akiyama, H. Kuwatsuka, T. Simoyama, Y. Nakata, K. Mukai, M. Sugawara, O. Wada and H. Ishikawa, "Nonlinear Gain Dynamics in Quantum-Dot Optical Amplifiers and its Application to Optical Communication Devices", *IEEE Journal of Quantum Electronics*, Vol. 37, No. 8, pp. 1059-1065, August 2001.

[7] T. Akiyama, H. Kuwatsuka, T. Simoyama, Y. Nakata, K. Mukai, M. sugawara, O. Wada and H. Ishikawa, "Application of Spectral-Hole Burning in the Inhomogeneously Broadened Gain of Self-Assembled Quantum Dots to a Multiwavelength-Channel Nonlinear Optical Device," *IEEE Photonics Technology Letters*, vol. 12, no. 10, pp. 1301-1303, October 2000.

[8] Y. Arakawa and A. Yariv, "Theory of Gain, Modulation Response and Spectral Linewidth in AlGaAs Quantum Well Lasers", *IEEE Journal of Quantum Electronics*, vol. QE 21, no. 10, pp. 1666 – 1674, Oct. 1985.

[9] M. H. Baier, S. Wtanabe, E. Pelucchi and E. Kapon, "High Uniformity of site-Controlled Pyramidal Quantum Dots Grown on Prepatterned Substrates", *Applied Physics Letters*, Vol. 84, No. 11, pp. 1943-1945, March 2004.

[10] Z.Bakonyi, H. Sui, G. Onishchukov, L. F. Lester, A.L. Gray, T. C. Newell and A. Tunnermann, "High-Gain Quantum-Dot Semiconductor Optical Amplifier for 1300 nm," *IEEE Journal of Quantum Electronics*, vol. 39, iss. 11, pp. 1409-1414, November 2003.

[11] G.A. Baraff and D. Gershoni, "Eigenfunction-expansion method for solving the quantum-wire problem: Formulation", *Physical Review* B, vol. 43, no. 5, 1991.

[12] G. Bastard, "Wave Mechanics Applied to Semiconductor Heterostructures", *Halsted Press*, 1988, ISBN 0-470-21708-1.

[13] P. Bhattacharya and S. Fathpour, "High-Speed 1.3 μm Tunnel Injection Quantum-Dot Lasers", *Applied Physics Letters*, vol. 86, pp. 153109-1 - 153109-3, 2005.

[14] P. Bhattacharya, S. Ghosh and A.D. Stiff-Roberts, "Quantum Dot Opto-Electronic Devices", *Annual Reviews of Material Research*, vol. 34, pp. 181- 218, March 2004.

[15] D. Bimberg, M. Grundmann and N.N. Ledentsov, "Quantum Dot Heterostructures", *John Wiley & Sons*, 1999, ISBN 0 471 97388 2.

[16] P. Borri, W. Langbein, J.M. Hvam, F. Heinrichsdorff, M. H. Mao and D. Bimberg, "Spectral Hole-Burning and Carrier-Heating Dynamics in InGaAs Quantum-Dot Amplifiers", *IEEE Journal of Selected Topics in Quantum Electronics*, vol. 6, no. 3, May/June 2000.

[17] P. Boucaud, S. Sauvage, "Infrared photdetection with semiconductor self-assembled quantum dots", *Comptes Rendus de l'Académie des Sciences – IR vision : from chip to image*, vol. 4 no 10, 2003, pp. 1133-1154.

[18] R.G. Broeke, J.J. Binsma, M. Van Geemert, T. De Vries, Y.S. Oei, X.J.M. Leijtens, M.K. Smit, "Monolithical Integration of Semiconductor Optical Amplifiers and Passive Mode-Filters for Low Facet Reflectivity", Proc. IEEE/LEOS annual Symposium, December 2001, ISBN 90-5487247-0, ed. H. Thienpont; F. Berghmans, J. Danckaert; L. Desmet, VUB, Brussel, 2001, pp. 57-61. OED [06.11]

[19] S.L. Chang and C.S. Chang, "A Band-Structure Model of Strained Quantum-Well Würtzite Semiconductors", *Semicond. Sci. Technol.* 12 (1997), pp. 252-263.

[20] S.L. Chuang, "Physics of Optoelectronic Devices", *Wiley Series in Pure and Applied Optics*, 1995, ISBN 0471109398.

[21] M. J. Connelly, "Semiconductor Optical Amplifiers". *Boston, London: Kluwer Academic Publishers*, 2002. ISBN 0792376579.

[22] M. J. Connelly, "Wideband Semiconductor Optical Amplifier Steady-State Numerical Model," *IEEE Journal of Quantum Electronics*, vol. 37, iss. 3, pp. 439-447, March 2001.

[23] M.A. Cusack, P.R. Briddon nad M. Jaros, "Eletronic Structure of InAs/GaAs Self-Assembled Quantum Dots", *Physical Review* B 54, no. 4 1996, pp. 2300-2303.

[24] B. Dagens, A. Markus, J.X. Chen, J.-G, Provost, D. Make, O. Le Gouezigou, J. Landreau, A. Fiore and B. Thedrez, "Giant Linewidth Enhancement Factor and Purely Frequency Modulated Emission from Quantum Dot Laser", *IEEE Electronic Letters*, vol. 41, no. 6, March 2005.

[25] J. H. Davies, "The Physics of Low-Dimensional Semiconductors", *Cambridge University Press*, 1998, ISBN 052148491X.

[26] A. Gahl and S. Balle, "Influence of the confinement factor on the wavelength-dependent output properties of a tapered traveling-wave semiconductor amplifier ", *Photonic Technological Letters*, vol. 11, pp 1375-1377, 1999.

[27] D. Gershoni, C. H. Henry and G.A. Baraff, "Calculating the Optical Properties of Multidimensional Heterostructures: Application to the Modeling of Quaternary Quantum Well Lasers", *IEEE Journal of Quantum Electronics*, vol. 29, no. 9, September 1993, pp. 2433-2450.

[28] S. Ghosh, S. Pradhan and P. Bhattacharya, "Dynamic Characteristics of High-Speed $In_{0.4}Ga_{0.6}As$/GaAs Self-Organized quantum Dot Lasers at Room Temperature", *Applied Physics Letters,* vol. 81, no. 16, pp. 3055-3057, October 2002.

[29] M. Grundmann and D. Bimberg, "Gain Threshold of Quantum Dot Lasers:Theory and Comparison to Experiments", *Jpn. J. Appl. Phys.* vol. 36 (1997), pp. 4181- 4187.

[30] P. Harrison, "Quantum Wells, Wires and Dots, Theoretical and Computational Physics", *John Wiley & Sons*, 2002, ISBN 0 471 98495 7.

[31] http://pages.ief.u-psud.fr/QDgroup/index.html

[32] http://www.ioffe.rssi.ru/SVA/NSM/Semicond/

[33] http://www.nextnano.de/

[34] Y. Z. Huang, Z. Pan and R.H. Wu, "Analysis of the optical confinement factor in semiconductor lasers", *Journal of Applied Physics.*, vol. 79, no. 10, pp 3827-3830, 1996.

[35] L. Jacak, P. Hawrylak and A. Wojs, "Quantum Dots". Springer-Verlag, 1998. ISBN 3540636536.

[36] H. Jiang and J. Singh, "Self-Assembled Semiconductor Structures: Electronic and Optoelectronic Properties", *IEEE Journal of Quantum Electronics*, vol. 34, no. 7, 1998.

[37] J. Kim, L. Wang and A. Zunger, "Comparison of the Electronic Structure of InAs/GaAs Pyramidal Quantum Dots with Different Facet Orientations", *Physical Review B*.57, no 16, April 1998.

[38] M. V. Kisin, B. L. Gelmont and S. Luryi, "Boundary-condition problem in the Kane model", *Physical Review B*, vol. 58, no. 8, 1998, pp 4605-4616.

[39] M. Kuntz, G. Fiol, M. Lämmlin, C. shubert, A. R Kovsh, A. Jacob, A. Umbach and D. Bimberg, "10 Gbit/s Data Modulation using 1.3 μm InGaAs Quantum Dot Lasers", *IEEE Electronic Letters*, vol. 41, no. 5, March 2005.

[40] S.A. Maksimenko, G. Y. Slepyan, N.N. Ledentsov, V.P. Kalosha, A. Hoffman, D. Bimberg, "Light Confinement in a Quantum Dot", *Semicond. Sci. Technol.* 15, pp. 491-496, 2000.

[41] P. Meystre, M. Sargent III, "Elements of Quantum Optics", *Springer*, 1999, ISBN 354064220X.

[42] T. C. Newell, D. J. Bossert, A. Stintz, B. Fuchs, K. J. Malloy and L.F. Lester, "Gain and Linewidth Enhancement Factor in InAs Quantum-Dot Laser Diodes", *IEEE Photonics Technology Letters*, vol. 11, no. 12, pp. 1527-1529, Dec. 1999.

[43] K. Okamoto, "Fundamentals of Optical Waveguides", *Academic Press*, 2000.

[44] M. G. Pala and G. Iannaccone, "A Three-Dimensional Solver of the Schrödinger Equation in Momentum Space for the Detailed Simulation of Nanostructures", *Nanotechnology* 13 (2003), pp. 369-372.

[45] J. Piprek, "Semiconductor Optoelectronic Devices, Introduction to Physics and Simulation", *Academic Press*, 2003, ISBN 0-12-557190-9.

[46] O. Qasaimeh, "Characteristics of Cross-Gain (XG) Wavelength Conversion in Quantum-Dot Semiconductor Optical Amplifiers," *IEEE Photonics Technology Letters*, vol. 16, no. 2, pp. 542-544, February 2004.

[47] O. Qasaimeh, "Optical Gain and Saturation Characteristics of Quantum-Dot Semiconductor Optical Amplifiers," *IEEE Journal of Quantum Electronics*, vol. 39, iss. 6, pp. 793-798, June 2003.

[48] E. U. Rafailov, P. Loza-Alvarez, W. Sibbett, G. S. Sokolovskii, D.A. Livshits, A. E. Zhukov and V.M. Ustinov, "Amplification of Femtosecond Pulses Over by 18 dB in a Quantum-Dot Semiconductor Optical Amplifier," *IEEE Photonics Technology Letters*, vol. 15, no. 8, pp. 1023-1025, August 2003.

[49] B.J. Riel, "An Introduction to Self-Assembled Quantum Dots", submitted to *American J. Physics.*

[50] A. Sakamoto and M. Sugawara, "Theoretical Calculation of Lasing Spectra of quantum-Dot Lasers: Effect of Homogeneous Broadeneing of Optical Gain," *IEEE Photonics Technology Letters*, vol. 12, no. 2,

February 2000.

[51] S. Schneider, P. Borri, W. langbein, U. Woggon, R. L. Sellin, D. Ouyang and D. Bimberg, "Linewidth Enhancement Factor in InGaAs Quantum-Dot Amplifiers", *IEEE Journal of Quantum Electronics*, vol. 40, no. 10, pp. 1423 – 1429, Oct. 2004.

[52] O. B. Schekin and D. G. Deppe, "1.3 μm InAs quantum Dot Laser with T_0=161 K from 0 to 90 °C", *Applied Physics Letters*, vol. 80, no. 18, pp. 3277-3279, May 2002.

[53] J. Singh, Electronic and Optoelectronic Properties of Semiconductor Structures, "*Cambridge University Press*", 2003, ISBN 0-07-057607-6.

[54] M.S. Skolnick and D.J. Mowbray, "Self-Assembled Semiconductor Quantum Dots: Fundamental Physics and Device Applications", *Annual Reviews of Material Research*, vol. 34, pp. 1-40, March 2004.

[55] B. Sonnenberg-Klein, K. L. Silverman and R. Mirin, "Multimode Lasing at Room Temperature from *InGaAs/GaAs* Quantum Dot Lasers", *Semiconductor Lasers for Lightwave Communications Systems, Proc.*, SPIE vol. 4533, pp. 1-8, August 21-22, 2001.

[56] O. Stier, M. Grundmann and D. Bimberg, "Electronic and Optical Properties of Strained Quantum-Dots Modeled by 8-Band *k.p.* Theory", *Physical Review* B 59, no. 8 1999.

[57] O. Stier and D. Bimberg, "Modeling of a Strained Quantum wires Using Eight-Band *k.p.* Theory", *Physical Review* B 55, no. 12, 1997, pp. 7726-7732.

[58] M. Sugawara, "Quantum-Dot Semiconductor Optical Amplifiers", *Optical Fiber Conference* 2003, vol 2, pp. 537-538.

[59] M. Sugawara, N. Hatori, T. Akiyama, Y. Nakata and H. Ishikawa, "Carrier Dynamics in Self-Assembled InGaAs/GaAs Quantum Dots and their Application to Optical Devices", *Optical Fiber Conference* 2003, pp. I-524, I-525.

[60] M. Sugawara, N. Hatori, T. Akiyama, Y. Nakata and H. Ishikawa, "Quantum-Dot Semiconductor Optical Amplifiers for High Bit-Rate Signal Processing over 40 Gbit/s", *Optical Fiber Conference* 2003, pp. I-260, I-261.

[61] M. Sugawara, T. Akiyama, N. Hatori, Y. Nakata and H. Ishikawa, "Quantum-Dot Semiconductor Optical Amplifiers for High Bit-Rate Signal Processing up to 160 Gbs^{-1} and a New Scheme of 3R Regenerators," *Measurement Science and Technology*, vol. 13, pp. 1683-1691, October 2002.

[62] M. Sugawara, N. Hatori, T. Akiyama, Y. Nakata and H. Ishikawa, "Quantum-Dot Semiconductor Optical Amplifiers for High Bit-Rate Signal Processing over 40 Gbit/s," *Japanese Journal of Applied Physics*, vol. 40, no. 5B, pp. L488-L491, 2001.

[63] M. Sugawara, N. Hatori, T. Akiyama and Y. Nakata, "Self-Assembled Quantum-Dot Lasers and Optical Amplifiers", 2001 *International Conference on Indium Phosphide and Related Materials Proc.*, 13th IPRM, 14 -18 May 2001.

[64] M. Sugawara, K. Mukai, Y. Nakata and H. Ishikawa, "Effect of Homogeneous Broadening of Optical Gain on Lasing Spectra in Self-Assembled $In_xGa_{1-x}As/GaAs$ Quantum Dot Lasers", *Physical Review B*, vol. 63, no. 11, pp. 7595-7603, March 2000.

[65] M. Sugawara, "Self-Assembled *InGaAs/GaAs* Quantum Dots", Semiconductors and Semimetals, vol. 60, *Academic Press*, 1999, 0-12-752169-0.

[66] T.D. Visser, H. Blok, B. Demeulenaere, and D. Lenstra, "Confinement Factors and Gain in Optical

Amplifiers", *Journal of Quantum Electronics*, vol. 33, no. 10, pp 1763-1766, 1997.

[67] T. D. Visser, B.Demeulenaere, J. Haes, D. Lenstra, R. Baets and H. Blok, "Confinement and Modal Gain in Dielectric Waveguides", *Journal of Lightwave Technology*, vol. 14, no. 5, pp. 885-887, 1996.

[68] I. Vürgaftman and J. R. Meyer, "Band Parameters for III-V Compound Semiconductors and their Alloys", *Journal of Applied Physics,* vol. 89, no. 11, pp. 5815-5875, 1 June 2001.

[69] W. P. Wong ,and K. S. Chiang , "Design of Waveguide Structure for Polarization-Insensitive Optical Amplification", *Journal of Quantum Electronics*, vol. 36, no. 11, pp. 1243-1250, 2000.

[70] Q. Xie, A. Madhukar, P. Chen and N.P. Kobayashi, "Vertically Self-Organized InAs Quantum Box Islands on GaAs (100)", *Physical Review Letters*, vol. 75, no. 13 (1995), pp. 2542-2546.

[71] M. Yamanishi and I. Suemune, "Comment on Polarization Momentum Matrix Elements in Quantum Lasers", *Japanese Journal of Applied Physics*, vol. 23, no. 1, 1984, pp. L35-L36.